William Caires Silva Amorim

Reduced-Order Simulation Models for ES-STATCOM based on Modular Multilevel Converters

Belo Horizonte, MG

2019

William Caires Silva Amorim

Reduced-Order Simulation Models for ES-STATCOM based on Modular Multilevel Converters

Dissertação submetida à banca examinadora designada pelo Colegiado do Programa de Pós-Graduação em Engenharia Elétrica do Centro Federal de Educação Tecnológica de Minas Gerais e da Universidade Federal de São João del-Rei, como parte dos requisitos necessários à obtenção do grau de Mestre em Engenharia Elétrica.

Centro Federal de Educação Tecnológica de Minas Gerais

Programa de Pós-Graduação em Engenharia Elétrica

Orientador: Prof. Dr. Heverton Augusto Pereira

Belo Horizonte, MG

2019

A524r

Amorim, William Caires Silva
Reduced-Order simulation models for ES-STATCOM based on modular multilevel converters / William Caires Silva Amorim. – 2019.
103 f.: il.

Dissertação de mestrado apresentada ao Programa de Pós-Graduação em Engenharia Elétrica em associação ampla entre a UFSJ e o CEFET-MG.
Orientador: Heverton Augusto Pereira.
Dissertação (mestrado) – Centro Federal de Educação Tecnológica de Minas Gerais.

1. Conversores de corrente elétrica – Teses. 2. Programação modular – Teses. 3. Energia armazenamento – Teses. 4. Sincronização – Teses. 5. Conversores de frequências – Teses. 6. Reguladores de voltagem – Teses. 7. Simulação (computadores) – Teses. I. Pereira, Heverton Augusto. II. Centro Federal de Educação Tecnológica de Minas Gerais. III. Universidade Federal de São João del-Rei. IV. Título.

CDD 621.313

Elaboração da ficha catalográfica pela Biblioteca-Campus II / CEFET-MG

À minha família, mentores e amigos.

Agradecimentos

Agradeço a Deus, primeiramente, por ter me iluminado em todos os passos nesta jornada acadêmica, e sobretudo aos meus pais Maria e Almir, por serem meu porto seguro e terem apoiado meus passos por todos estes anos. Aos meus irmãos, Lucas e Géssica, por todo apoio e companheirismo oferecidos nesta caminhada. Aos meus avós, em especial, minha avó Valdice por todas as orações e as bençãos dadas para guiar meus passos. A Dona Graça e família, por serem minha segunda família desde minha vinda para Viçosa.

Aos professores que me orientaram neste trabalho, Prof. Allan Cupertino e Prof. Heverton Pereira. Aos amigos da graduação, mestrado, DEL e de Viçosa por toda a ajuda oferecida no decorrer deste mestrado. Aos membros do grupo de pesquisa GESEP, especialmente, João Marcus, João Victor, Rodrigo, Renata, Dayane, Lucas Santana, Lucas Gusman e Paulo, por todo companheirismo e conhecimento compartilhado. Por fim, agradeço ao CEFET-MG pelo apoio financeiro.

"Não fui eu que ordenei a você? Seja forte e corajoso!
Não se apavore nem desanime, pois o Senhor,
o seu Deus, estará com você por onde você andar.
(Josué 23:1-9)

Resumo

Devido à crescente integração de energias renováveis, os sistemas elétricos de potência podem tornar-se mais suscetíveis a desequilíbrios de tensão da rede, distúrbios de frequência, ressonâncias harmônicas, entre outros. Desta forma, diversos trabalhos apontam que os serviços auxiliares fornecidos pelos sistemas de armazenamento de energia podem minimizar esses problemas. A combinação do armazenamento de energia por baterias eletroquímicas e de compensadores síncronos estáticos (STATCOMs, do inglês *Static Synchronous Compensator*) figura como uma das propostas para reduzir o custo destes sistemas. Os conversores modulares multiníveis são apresentados como uma boa solução para a realização de sistemas de armazenamento de energia e de STATCOM, devido à sua alta eficiência, modularidade, qualidade da tensão de saída, entre outros. No entanto, existe uma elevada complexidade no estudo da integração de sistemas de armazenamento de energia e de STATCOMs baseado em conversores modulares multiníveis, aplicados a um sistema elétrico de potência. Esta complexidade é devido à presença de conversores eletrônicos de potência, sistema de transmissão, fontes renováveis, transformadores, entre outros, que acarretam em um alto esforço computacional para simulação. Neste sentido, este trabalho apresenta o projeto detalhado de um conversor modular multinível e a implementação de três modelos computacionais de simulação de ordem reduzida. Os modelos computacionais representam conversores modulares multiníveis aplicados em sistemas de armazenamento de energia agregado a um STATCOM, denominado ES-STATCOM (do inglês *Energy Storage System - Static Synchronous Compensator*). O desempenho destes modelos é comparado em três estudos de casos: análise do processo de carga e descarga do sistema de armazenamento, estudo de suporte de frequência e, finalmente, de suporte de tensão, considerando um conversor modular multinível de 100 MVA conectado a uma rede elétrica de 33 kV. Os resultados revelaram uma alta similaridade do comportamento dinâmico de variáveis como potência ativa, potência reativa, corrente circulante e corrente da rede, entre os modelos de simulação de ordem reduzida. Além disso, os modelos foram comparados em termos da figura de mérito de erro absoluto integral normalizado e do tempo total de processamento, revelando um baixo erro entre os modelos de ordem reduzida, além de uma redução entre 50% a 70% do tempo de processamento total.

Palavras-chaves: Conversor modular multinível; ES-STATCOMs; suporte de frequência à rede elétrica; suporte de tensão à rede elétrica; modelos de simulação de ordem reduzida.

Abstract

Due to the high penetration of renewable energies, power systems may become more susceptible to grid voltage fault, grid frequency disturbances, harmonic resonances and others. Several studies have pointed out that ancillary services provided by energy storage systems can minimize such kind of problems. The combination of energy storage by electrochemical batteries and static synchronous compensator has been proposed to reduce the cost of these systems. Modular multilevel converters are presented as a good solution for building energy storage systems and static synchronous compensator (STATCOM) due to their high efficiency, modularity and inherent fault tolerance structure. However, the study of the integration of energy storage systems and STATCOM based on modular multilevel converters applied in an electrical power system is complex. This complexity is due to the presence of power electronics, transmission system, renewable sources, transformers, among others, which results in a high computational effort for simulation. In this sense, this work presents the detailed design of a modular multilevel converter and implementation of three reduced-order simulation models. The computational models represent modular multilevel converter applied to energy storage systems aggregated to a STATCOM, called ES-STATCOM (Energy Storage System - Static Synchronous Compensator). The performance of these models are compared in three case studies: analysis of the charging and discharging process of the designed storage system, frequency support and voltage support. A 100 MVA modular multilevel converter connected to a 33 kV grid is considered. The results indicated a high similarity of the dynamic behavior of variables such as active power, reactive power, circulating current and grid current among the reduced-order simulation models. Moreover, the models were compared based on the figure of merit normalized integral of absolute error (NIAE) and the total processing time variables. The results revealed a low error between the reduced-order models and a reduction between 50% to 70% of the total processing time.

Key-words: Modular multilevel converter; ES-STATCOMs; grid frequency support; grid voltage support; reduced-order simulation models.

List of Figures

List of Tables

List of abbreviations and acronyms

ac	Alternating Current
ALA	Arm-level Averaged
ATB	Average Tolerance Band
BESS	Battery Energy Storage Systems
BMS	Battery Management System
CTB	Cell Tolerance Band
CS	Circuit Simulators
dc	Direct Current
DS	Double Star
DSFB	Double-Star Full Bridge
DSHB	Double-Star Half Bridge
DSOGI	Dual Second-Order Generalized Integrator
ECP	Electrochemical Performance
EMS	Energy Management System
ES	Energy Storage
EP	Electrical Performance
FB	Full Bridge
HB	Half Bridge
HVDC	High-Voltage Direct Current
IAE	Integral of Absolute Error
IGBT	Insulated Gate Bipolar Transistor
ISE	Integral of Squared Error
JB	Junction Box

LLA	Leg-Level Average
LPF	Low-Pass Filter
LVRT	Low Voltage Ride-Through
MES	Mathematical Equation Solvers
MMC	Modular Multilevel Converter
MP	Mathematical Performance
MV	Medium Voltage
NIAE	Normalized Integral of Absolute Error
NLC	Nearest-Level Control
NS	Negative Sequence
NPC	Neutral-Point Clamped
OCV	Open-Circuit Voltage
PC	Personal Computer
PI	Proportional Integral
PCC	Point of Common Coupling
PLL	Phase-Locked Loop
PS	Positive Sequence
PCS	Power Conversion Systems
PV	Photovoltaic
PR	Proportional Resonant
pu	Per Unit
qZSI	Quasi-Z-Source Converter
rms	Root Mean Square
SLA	Submodule-Level Averaged
SLS	Submodule-Level Switched
SM	Submodule

S&S	Sorting and Selection
SSS	Submodule Semiconductors Switches
STATCOM	Static Synchronous Compensator
SOC	State-of-Charge
T&D	Transmission and Distribution
THD	Total Harmonic Distortion
VSC	Voltage Source Converter
VSM	Voltage Source Model
WPP	Wind Power Plant
ZSI	Z-Source Converter

List of symbols

$B_{i,j}$	i-th series battery pack in j-string
$B_{eq,ALA}$	Equivalent battery pack for ALA model
$B_{eq,SLS}$	Equivalent battery pack for SLS model
$B_{eq,VSM}$	Equivalent battery pack for VSM model
C	Capacitance submodule
C_{eq}	Equivalent capacitance arm for ALA model
$C_{bat,r}$	Discharging rate recommended of battery pack
$C_{bat,n}$	Nominal capacity of battery pack
$C_{bat,0}$	Initial capacity of battery pack
D_1	Top diode
D_2	Bottom diode
E_n	Total energy storage requirement
f_g	Grid frequency
$g^i_{u,n}$	Gate signal for the i-submodule in upper arm of n-th phase
$g^i_{l,n}$	Gate signal for the i-submodule in lower arm of n-th phase
$\widehat{I}$	Peak of grid current
i_{bat}	Battery cell current
i_u	Upper arm current
i_l	Lower arm current
$i_{g\alpha\beta}$	Grid current stationary frame
$i^*_{gp,\alpha\beta}$	Reference of active grid current in stationary frame
$i^*_{gq,\alpha\beta}$	Reference of reactive grid current in stationary frame
$i^*_{g,\alpha\beta}$	Reference of grid current in stationary frame

$i_{g,n}$	Grid current of n-phase
$i_{g,n}$	Grid voltage of n-phase
$i_{c,n}$	Circulating current for the n-phase
$i^*_{c,n}$	Circulating current reference for the n-phase
i^+_g	Positive sequence of grid current
i^-_g	Negative sequence of grid current
$k_{i,avg}$	Integral gain of average control
$k_{p,avg}$	Proportional gain of average control
$k_{p,g}$	Proportional gain of grid current control
$k_{r,g}$	Resonant gain of grid current control
$k_{p,z}$	Proportional gain of circulating current control
$k_{r,z}$	Resonant gain of circulating current control
L_{grid}	Grid inductance
L_{arm}	Arm inductance
L_{eq}	Equivalent inductance of arm in VSM model
m	Modulation amplitude index
$N_{u,n}$	Number of submodule inserted in upper arm of n-phase
$N_{l,n}$	Number of submodule inserted in lower arm of n-phase
N_s	Battery racks in series
N_p	Battery racks in parallel
$N_{p,power}$	Number of parallel battery strings based on rated power converter
$N_{p,energy}$	Number of parallel battery strings based on energy storage requirement
N	Submodules per arm
P^*	Active power reference
P_n	Rated active power
P_{meas}	Active power measured in the VSM model

$P_{b,min}$	Minimum battery pack power
$p_{u,n}$	Instantaneous active power in upper arm
$p_{l,n}$	Instantaneous active power in lower arm
$\overline{p}_{g,n}$	Mean value of active power in each phase
$\widetilde{p}_{g,n}$	Oscillating value of active power in each phase
Q_n	Rated reactive power
Q_{meas}	Reactive power measured in the VSM model
R_{arm}	Arm inductor resistance
R_{eq}	Equivalent resistance of arm in VSM model
R_{grid}	Grid resistance
r_{bat}	Battery cell resistance
S_1	Top IGBT
S_2	Bottom IGBT
SOC_{max}	Maximum SOC operation for the battery pack
SOC_{min}	Minimum SOC operation for the battery pack
$SOC_{i,pu}$	Instantaneous SOC of battery rack model
SOC^*_{sm}	SOC reference per submodule
$SOC_{u,i}$	SOC for the i-submodule in upper arm
$SOC_{l,i}$	SOC for the i-submodule in lower arm
$SOC_{lim,l}$	Lower SOC limit for the SOC submodule
$SOC_{lim,u}$	Upper SOC limit for the SOC submodule
$SOC_{avg,glob}$	Average global SOC
$SOC^*_{avg,glob}$	Reference average global SOC
$SOC_{n,avg}$	Average SOC per phase in n-phase
$SOC^*_{n,avg}$	Reference of average SOC per phase in n-phase
$SOC_{n,diff}$	Difference SOC per phase in n-phase

$SOC^*_{n,diff}$	Reference of difference SOC per phase in n-phase
SOC_{pu}	SOC estimation of battery rack model
S_n	Rated apparent power
$\widehat{V}$	Peak of grid voltage (line-to-neutral)
V_{dc}	Nominal dc-link voltage
$V_{b,max}$	Maximum battery pack voltage
$V_{b,min}$	Minimum battery pack voltage
V_g	Output voltage (line-to-line)
V^*_{sm}	Submodule voltage reference
$v_{bat,ocv}$	Battery cell open circuit voltage
$v_{sm,i}$	i-th submodule voltage
v_{dc}	Instantaneous dc-link voltage
$v_{dc,min}$	Minimum dc-link voltage
$v_{g,n}$	Grid voltage of n-phase
$v^+_{g,d}$	Positive sequence of d-component grid voltage in stationary frame
$v^-_{g,d}$	Negative sequence of d-component grid voltage in stationary frame
$v^+_{g,q}$	Positive sequence of q-component grid voltage in stationary frame
$v^-_{g,q}$	Negative sequence of q-component grid voltage in stationary frame
v^+_g	Positive sequence of grid voltage
v^-_g	Negative sequence of grid voltage
$v_{s,n}$	Equivalent output voltage in n-phase
$v_{c,n}$	Internal voltage in n-phase
$v_{u,n}$	Reference signal for upper arm in n-phase
$v_{l,n}$	Reference signal for upper arm in n-phase
x_{eq}	Converter equivalent output inductance
x_{arm}	Per unit arm reactance

x_{ref}	Reference variable of NIAE computation
x_m	Measured variable of NIAE computation
Δ	Grid voltage angle
Δv_g	Maximum grid voltage variation
$\Delta SOC_{i,pu}$	SOC increment of battery rack model
ϕ	Grid current angle
θ_v	Phase angle of each grid phase
ω_g	Grid angular frequency
$\hat{\theta}$	Grid angular displacement

Superscripts

$*$	Reference value
$+$	Positive sequence
$-$	Negative sequence

Subscripts

u	Upper arm
l	Lower arm
dq	direct and quadrature axis
$\alpha\beta$	stationary reference frame

Contents

1 Introduction

1.1 Context and Relevance

Renewable energy systems based on photovoltaic (PV) and wind power plants (WPPs) are frequently featured by their intermittent power generation characteristic. When a high penetration scenario of renewable energy in the power system is considered, some issues as voltage flicker, instabilities during fault conditions and harmonic resonances may arise (Saqib; Saleem, 2015; Bharadwaj; Maiti, 2017). Under such conditions, static synchronous compensator (STATCOM) has been employed to improve the grid power quality and to provide the low voltage ride-through (LVRT) capability, as required by the modern grid codes (Cheng et al., 2006).

The growth of large WPPs have lead to the displacement of conventional power plants and to a system with reduced inertia and frequency control reserves (Saqib; Saleem, 2015). In this context, energy storage systems would enable WPPs to contribute to these functionalities and to operate as modern flexible and dispatchable power plants. Therefore, grid-scale battery energy storage systems (BESS) have been developed to provide spinning reserve, load compensation and energy storage (Vasiladiotis; Rufer, 2015; Li et al., 2018).

Traditionally, STATCOMs lack energy storage capacity. Hence, they cannot provide significant inertia, load leveling or power buffering services. For the sake of economy, the companies have studied the integration of the STATCOM and BESS functions in the same device. Such kind of system is referred, in this work, as ES-STATCOM (Bharadwaj; Maiti, 2017). BESS plays an important role in the power flow in the power system. Thus, BESS are able to perform the so-called ancillary services, such as frequency support, voltage support, power backup, among others (Knap et al., 2016; Xavier; Cupertino; Pereira, 2018). In the ancillary services studies, the power system simulated includes grid model, loads, transformers, converters, generation sources, among others, which impacts in a higher computational burden (Saad et al., 2013). In this sense, reduced models of components, as converters, grid model and others, are able to decrease the simulation time consumption and increase the number of components simulated (CIGRE, 2014). For this reason, this work aims to present simulation models for ES-STATCOM to increase the simulation performance.

The next sections discusses the evolution of the installed battery bank capacity around the world, due to the price reduction of the lithium-ion batteries. In addition, the components and services performed by the BESS are discussed. Finally, converter topologies applied in the ES-STATCOM are introduced.

1.2 BESS Overview

BESS have been used for some decades in isolated areas, especially to supply energy or meet some service demand (Baker; Collinson, 1999). BESS offer some attractive advantages in relation to traditional energy storage systems (ESS), such as pumped hydro storage, thermal storage and compressed air energy storage (CHEN et al., 2009). The fastest response time (generally, lower than one second) makes the BESS able to offer important services in the power system (CHEN et al., 2009; Qian et al., 2011; Horiba, 2014).

Nowadays, in the scenario of high penetration of renewable energy, BESS play a key role in the efforts to combine a sustainable energy source with a reliable dispatched load and to mitigate the impacts of the intermittent sources (Chatzinikolaou; Rogers, 2017). Renewable energies, as photovoltaic and wind power system, among other alternatives, account for a significant part of the electric power generation matrix all around the world. However, the intermittent characteristic of renewable generation leads to the need of store the produced energy. Among the storage technologies, storing the energy produced in chemical battery banks, known as BESS, is one of the most applied in power systems (Lawder et al., 2014; REN21, 2019).

In recent years, the installation of BESS has increased throughout the world. Fig. 1 (a) presents the global battery storage capacity that totaled just over 3 GW in the end of 2018 (IEA, 2019; IRENA, 2017). During the period of 2013-2018 the global battery storage capacity has increased about 943 %. In addition, the Fig. 1 (b) presents a lithium-ion battery price that is around in 176 $ per kWh in end of 2018 (BNEF, 2019). In the period of 2013-2018 the battery pack price reduced 73 %. This fact can be explained by the new technologies of batteries that emerged in the last years, such as lithium-ion battery. In 2019, the Nobel Prize in chemistry was awarded to three scientists: John B. Goodenough (american), M. Stanley Wittingham (british) and Akira Yoshino (japanese) for the development of lithium-ion battery, that is widely used in portable electronic equipment, electric vehicles, BESS, among others (NOBEL PRIZE, 2019).

Many companies that deal with power systems have been specializing and marketing BESS in the market. ABB, Samsung and Siemens offer ES-STATCOM and/or BESS units. For instance, Siemens commercializes the SVC PLUS Frequency Stabilizer. This system includes supercapacitors in the converter dc-link to provide primary frequency support (SIEMENS, 2018). In 2011, ABB commissioned a STATCOM combined with a BESS in Norfolk, UK. The so-called DynaPeaQ was based on ABB's SVC Light STATCOM and a Li-ion battery bank of 200 kWh (ABB, 2016; ABB, 2017). Tab. 1 presents some projects developed with BESS in America, Europe and Oceania, which provide ancillary services.

Fig. 2 presents a diagram, emphasizing the constituent parts of a BESS, from the

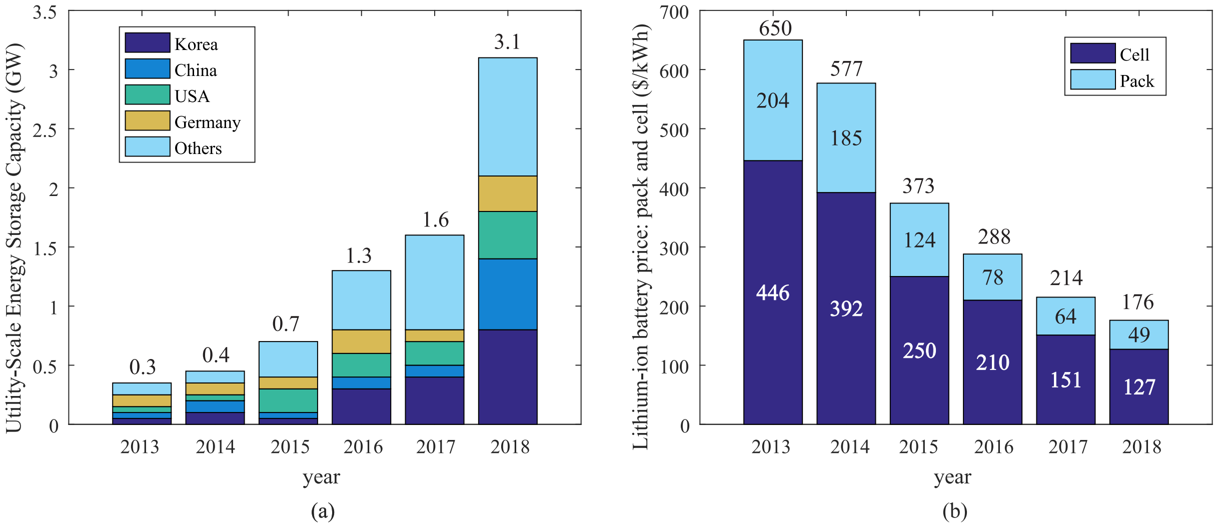

Figure 1 – BESS increasing in terms of installation and price. (a) Utility-scale energy storage capacity in last years (b) Lithium-ion battery price in last years (Based on (IEA, 2019; BNEF, 2019)).

Table 1 – Examples of BESS projects installed for power systems services (Based on (AES, 2017; ABB, 2017; NEOEN, 2018; SAMSUNG, 2018)).

BESS Project	Service Performed	Rated Power	Manufacturer
Hornsdale, Australia	Power Quality and Backup Power	300 MW	Tesla
SDG&E, USA	Black Start Capability	30 MW	AES
Angamos, Chile	Spinning Reserve and Frequency Regulation	20 MW	ABB
Chitose Hokkaido, Japan	Voltage Support	17 MW	ABB
Schwerin, Germany	Frequency Regulation	10 MW	Samsung

battery cell to the storage container (ADB, 2018). The basic storage unit is formed by the cell. The association of several units in series and parallel, forms the so-called module. This last unit is controlled by the battery management system (BMS) which controls the electrical and thermal characteristics of the module, as state-of-charge (SOC), current, temperature and voltage, to avoid any a harmful operation. For protection purposes, the BMS and module are enclosed by the junction box (JB). This set is known as battery pack and forms a larger unit, with well-defined electrical characteristics.

In systems that deal with high power, it is necessary to increase the units of battery pack used, including several units in a larger unit, called battery rack. Under this scenario, a power converter performs the connection between the power system and the battery rack. An energy management system (EMS) is also used to ensure the electrical and thermal characteristics mentioned for each battery rack. Battery racks, EMS and power conversion systems (PCS) are installed in a larger environment such as a container. Finally, in a power

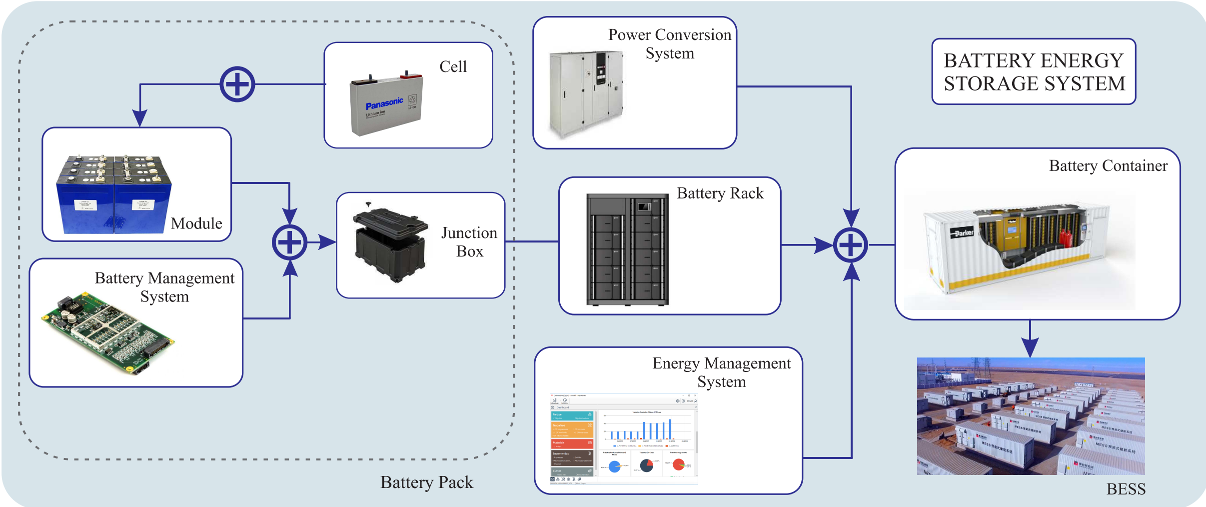

Figure 2 – Schematic of a Battery Energy Storage Systems (Adapted from (ADB, 2018)).

system, the group formed for several battery containers compose the so-called BESS.

1.3 Services performed by ES-STATCOM

The viability of the ES-STATCOM installation connected to medium voltage (MV) grids depends on the services provided and agreements with the local power system operator. The typical services provided are illustrated in Fig. 3 and described below:

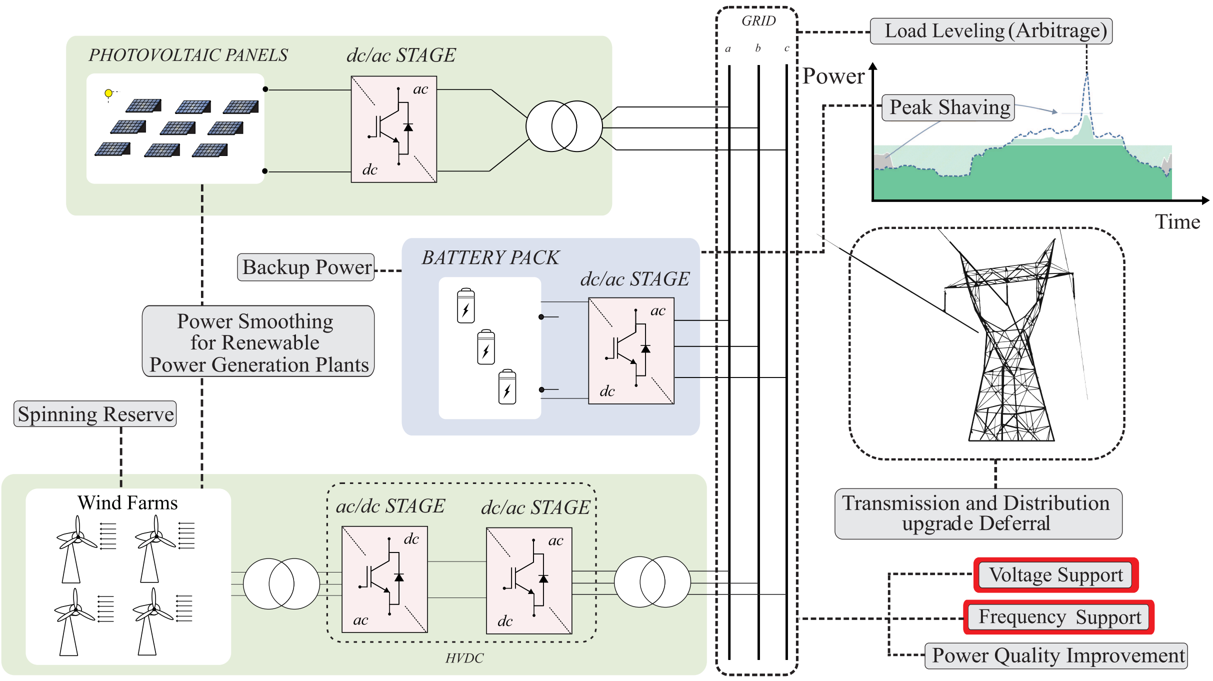

Figure 3 – Ancillary Services performed by ES-STATCOM.

- peak shaving: the energy purchased from the utility during peak demand hours can be reduced through BESS. Since the energy price in the peak demand hours is typically more expensive, BESS has become an attractive alternative to companies with high electricity consumption during peak hours. BESS is usually controlled to charge at low demand hours and discharge at the critical time of demand (Prasatsap; Kiravittaya; Polprasert, 2017);

- transmission and distribution (T&D) upgrade deferral: if there is a constant overload at a specific point in the T&D lines, the electric utility needs to adapt its infrastructure to support this new demand. However, this is expensive and usually complex, as it may be necessary to upgrade T&D devices, such as transformer lines, to support the new power flow. An increasingly viable alternative is the installation of BESS near the overloaded grid point, to reduce the effects on T&D devices. As a result, the upgrading in the T&D infrastructure can be delayed or avoided (Garcia-Garcia; Paaso; Avendano-Mora, 2017);

- load leveling (arbitrage): this is an expression to designate energy trade. Basically, BESS absorbs energy during low demand hours, when energy is cheaper, and injects it into the grid in hours of high demand, when energy is more expensive. This service is similar to peak shaving, however the goal is to distribute the load rather than just remove the peak. Therefore, the main benefit is the energy price difference between those hours (Walawalkar; Apt; Mancini, 2007; Abdelrazek; Kamalasadan, 2016);

- power smoothing for renewable power generation plants: the intermittent power generation in renewable energy systems, such as WPP or PV, can be maintained at an appropriate level for a period of time, which alleviates the output power, reducing the rapid oscillations of the voltage and power in the grid (Li; Hui; Lai, 2013; Abdelrazek; Kamalasadan, 2016);

- backup power: since photovoltaic power plants generate energy only during few hours of the day, especially at low demand times, the BESS system can be used to absorbs this generated energy and inject it out of the generation time (Velasco de la Fuente et al., 2013);

- frequency support: recent studies have addressed the ability of microgrids to operate in islanded mode and the BESS ability to provide frequency support and uninterrupted supply in the absence of the main grid (Velasco de la Fuente et al., 2013; Serban; Marinescu, 2014);

- spinning reserve: large power generators usually operate below their total capacity and maintain some reserve to withstand unexpected load variations. Thus, the BESS system can be used to injects energy to increase the generation (Knap et al., 2016);

- power quality improvement: different concepts of BESS are proposed to guarantee the voltage quality requirements, especially in scenarios with high penetration of distributed generation, in order to deal with the effects of variation in the grid voltage between the periods of high and low demand. In this sense, harmonic compensation are applied to the BESS, improving aspects of power quality (Krata; Saha, 2019);
- black start capability: several studies propose the use of BESS to promote the recovery of a total or partial power system subjected to a blackout. Under such conditions, the assistance given by BESS reduces the time of grid interruption and the economic losses (Xu et al., 2015);
- voltage support: in scenario of high penetration of renewable energies, the power systems are susceptible to disturbance in grid voltage. In this situation, the operator needs to ensure the operation of components connected through voltage support. In this situation, the systems can face symmetrical and asymmetrical grid faults, then ES-STATCOM can be used to inject reactive current for supporting the voltage regeneration (Xavier; Cupertino; Pereira, 2018; Krata; Saha, 2019).

In this work, the explored ancillary services of study are the frequency and voltage support, those are highlighted in the Fig. 3. These ancillary services are studied to analyze the performance of converters simulation models applied to the ES-STATCOM.

1.4 Converters applied in ES-STATCOM

Power converters play an important role in the integration of BESS with the power system. The general structure of a ES-STATCOM connected to the grid is composed of battery pack, dc/dc stage and dc/ac stage. Fig. 4 shows topologies widely used for ES-STATCOM applications. The topologies discussed are the (a) two-level converter, (b) three-level converter and (c)-(f) cascaded multilevel converters configurations.

The two-level and three-level converters are topologies with step-up transformers when medium voltage applications are required. Fig. 4 (a) presents a two-level converter, with the voltage source converter (VSC), ZSI (Z-source converter) and qZSI (Quasi-Z-source converter) configurations applied in the ac/dc stage (Vazquez et al., 2010; Krishnamoorthy et al., 2014). Generally, it is used a low-pass filter (LPF), such as LC or LCL filters, to attenuate the injected harmonics and to perform the grid connection. In the VSC configuration, the battery bank can be connected directly to the ac/dc stage or connected through the dc/dc stage. In addition, ZSI and qZSI were proposed to overcome these drawbacks inherent of the VSC topology (Fang Zheng Peng, 2003; Liu et al., 2013).

Fig. 4 (b) presents a three-level converter, with the three-level diode clamped multilevel converter (NPC converter) and three-level flying capacitor converter. The NPC

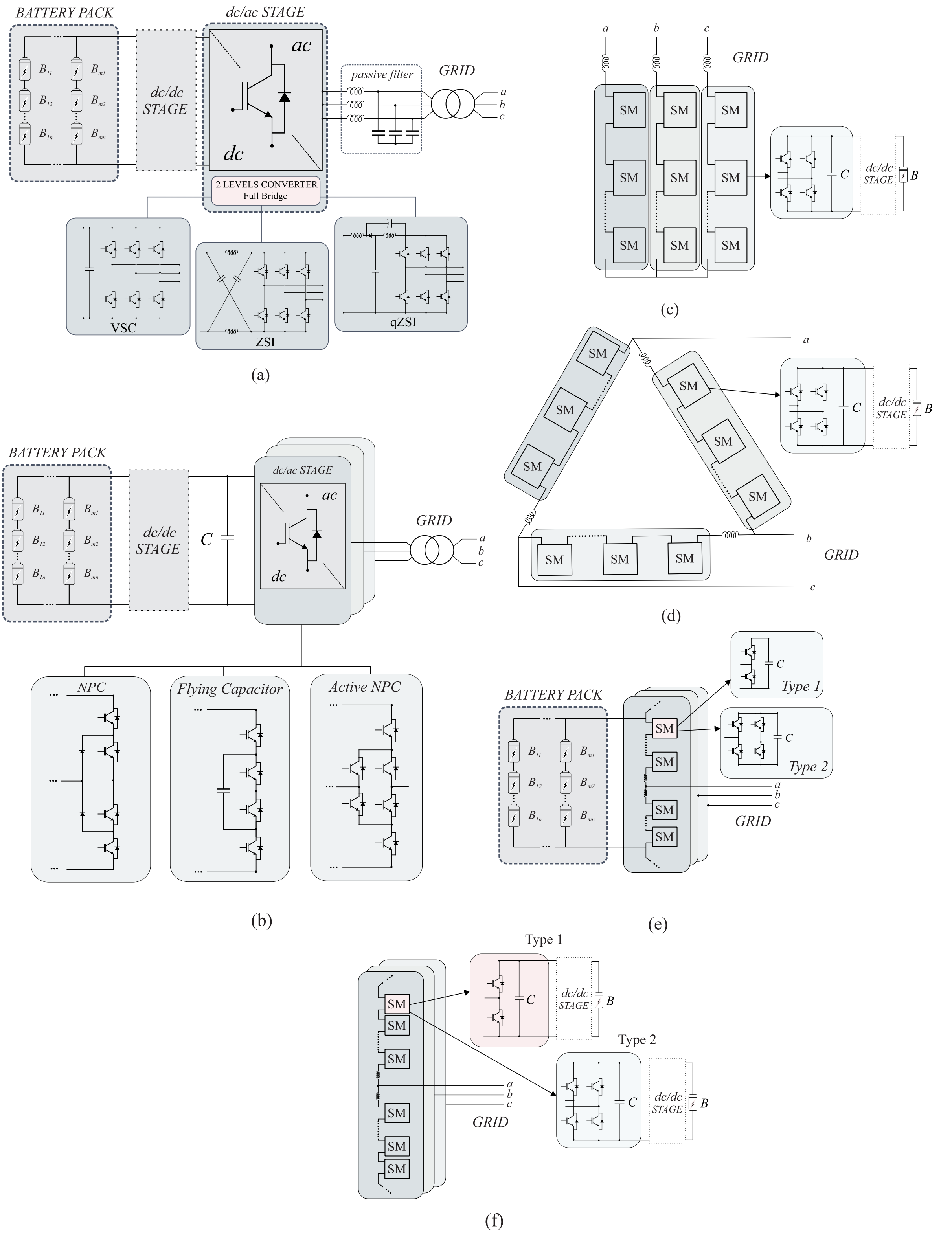

Figure 4 – ES-STATCOM technologies: (a) two-level converters: VSC, ZSI and qZSI (b) three level converters: NPC and flying capacitor (c) Star-connected cascaded multilevel converter (d) delta-connected cascaded multilevel converter (e) DSHB or DSFB with BESS centralized (f) DSHB or DSFB with BESS decentralized.

configuration has the advantage of greater degree of freedom to increase the magnitude of the output voltage and to improve the harmonic performance, reducing filter requirements. The disadvantage of this topology is the more complex control and modulation techniques required in relation to the two-level converters (Pou et al., 2005; Arifujjaman, 2015). As an alternative, the three-level flying capacitor converter uses capacitors instead of clamping diodes to divide the dc voltage input. In addition, the balancing of the capacitors can be carried out through the modulation.

To deal with the SOC unbalance of the batteries and to improve features like power losses, the cascaded multilevel converters emerged as an attractive topology in ES-STATCOM systems (Ch; Maiti, 2016; Feng et al., 2018; Chivukula; Maiti, 2019). The advantages of this topology are:

- low voltage switches, reducing the implementation costs;
- low switching frequency, which implies in high efficiency;
- high output voltage quality, reducing the harmonics distortion in the grid;
- fault-tolerance and redundancy, increasing the converter reliability.

Fig. 4 (c)-(f) present different configuration of cascaded multilevel converters topologies (Soong; Lehn, 2014a). Fig. 4 (c) and Fig. 4 (d) present a star-connected cascaded multilevel converter and delta-connected cascaded multilevel converter topologies, respectively (Sochor; Akagi, 2016). The star-connected cascaded multilevel converter is less expensive, in terms of physical systems implementation. On the other hand the delta-connected cascaded multilevel converter has better dynamics in situations of symmetrical and asymmetrical grid faults.

Another cascaded multilevel converter topology is the modular multilevel converter (MMC), patented by (Marquadt, 2001). The Double-Star (DS) is one variation of MMC topology, that can be formulated by different submodules (SM): half bridge SM, that is applied in the double-star half bridge (DSHB) or full bridge SM, that is applied in the double-star full bridge (DSFB) (Soong; Lehn, 2014b; Vasiladiotis; Cherix; Rufer, 2015). The battery packs can be located in centralized (disposition between the physical dc-link) or decentralized form (disposition between the SMs). Fig. 4 (e) and Fig. 4 (f) present a battery packs centralized in a DSHB or DSFB topology and a battery packs decentralized in DSHB or DSFB topology, respectively (Chen; Li; Cai, 2017).

Some challenges are considered in decentralized configuration, such as unbalances between the SOC can lead to dc current injection into the grid. The dc/dc stage, shown in Fig. 4 (f), decouples the battery from the capacitor, that can reduce the dc filter required and increase the battery lifetime (Uno; Tanaka, 2011; Serban; Marinescu, 2014). While in centralized configuration, the dc-link fault is a considerable problem, requiring current limiter mechanisms, in the decentralized configuration the dc-link fault can be dealt just bypassing the SM with fault.

Due to MMC topology presenting inherent advantages of cascaded multilevel converter topologies, such as: the use of low voltage switches, modularity, fault-tolerant, low frequency switching operation and high output voltage quality, this topology is chosen to represent the ES-STATCOM in this work. In addition, the DSHB is choose among the cascaded multilevel converter topologies, once the DSHB topology is more suitable for unbalanced voltage conditions and presents a lower current rating when compared with the delta-connected cascaded multilevel converter (Cupertino et al., 2019).

1.5 DSHB Simulation Models

The MMC is a promising candidate for ES-STATCOM realization, as it can be directly connected to the medium-voltage system without the use of line transformers, providing an efficient and compact solution (Vasiladiotis; Rufer, 2015; Hillers; Stojadinovic; Biela, 2015). Despite the benefits, the implementation of such systems faces considerable challenges. In contrast to other multilevel approaches, the energy storage can be concentrated in the SMs, that is referred as decentralized BESS. Low voltage battery racks can be directly integrated in the converter SM. Thus, the modularity of the topology results in an inherent fault-tolerant solution (Hillers; Biela, 2014; Soong; Lehn, 2016).

Despite the technical advantages, the MMC modeling and simulation are challenging, since the converter contains hundreds or thousands of switching devices and passive components (Pereira; Kontos; Teodorescu, 2017). The simulation of the switching devices requires relatively small time steps, resulting in a considerable computational effort and a long simulation time (Sharifabadi et al., 2016; Pereira; Kontos; Teodorescu, 2017). Therefore, reduced-order models play an important role in the simulation of MMC based systems.

Most approaches in the technical literature propose simulation models for MMC focused on high-voltage direct current (HVDC) systems (Saad et al., 2013; Xu; Gole; Zhao, 2015; Ajaei; Iravani, 2015; Karaagac et al., 2017; Hao et al., 2019). Pereira, Kontos and Teodorescu (2017) compared two improved MMC average models combined with modulation strategies for the representation of individual capacitor voltages and current ripples. Sharifabadi et al. (2016) classifies the simulation models for MMC HVDC systems into four categories: leg-level average (LLA), arm-level averaged (ALA), submodule-level averaged (SLA) and submodule-level switched (SLS). Ahmed et al. (2014) proposed an efficient model to simulate internal faults in the SM converter. Beddard, Barnes and Preece (2015) and Ajaei and Iravani (2015) discussed models able to represent the converter dynamics during dc and ac faults. Rodrigues et al. (2016) proposed a fast model for the power losses evaluation and consequently, converter efficiency. Finally, reference (Zhang et al., 2019) discussed an approach for the thermal modeling of modular multilevel converters.

Regarding the power system engineering, simulation models with relatively large time steps and capable of representing the ES-STATCOM during voltage and frequency support are strongly necessary. The technical brochure elaborated by Conseil International des Grands Réseaux Électriques (CIGRE) focus in comparing models of MMC with different types of complexity applied to HVDC system (CIGRE, 2014). This document evaluate the requirements of simulation models for MMC topologies to provide a framework for model development consistent with the currently known MMC technologies. The simulation models proposed can be adapted to changing power electronic topologies and control algorithms.

Nevertheless, a detailed investigation on simulation models of MMC based on ES-STATCOMs has not been presented yet. This system presents challenges to representations of elements such as transformers, grid, generation sources, transmission lines and the MMC. This converter deals with the difficulty in implementing a high number of submodules, dynamics of semiconductor switches, dynamics of SOC in batteries, among others.

1.6 Objectives

There is a lack in the literature which consider the dynamics of simulation models of ES-STATCOM connected in grid systems. Thus, this work aims to fill this void, providing the following reduced-order simulation models evaluation: submodule-level switched (SLS), arm-level average (ALA) and voltage source model (VSM). Especially, a study of simulation models for DSHB based on ES-STATCOM was not realized. In this sense, this master thesis intends to fill this void. Therefore, the main goals of this work are:

- design of the DSHB ES-STATCOM based on required ratings;
- evaluation of the dynamics of the MMC during the BESS charging and discharging process;
- simulation models considering an ES-STATCOM application in an offshore WPP. In addition, the performance of reduced-order models are analyzed during voltage and frequency support;
- investigation of reduced-order simulation models: submodule-level switched (SLS), arm-level average (ALA) and voltage source model (VSM).

1.7 Contributions

Considering the above discussions, the main contributions of this work are:

- demonstration of the methodology to design a ES-STATCOM in order to attend the required ratings;
- discussion of the ES-STATCOM dynamics in the process of batteries charging and discharging. In addition, evaluating the studied ES-STATCOM simulation models in grid frequency and grid voltage support;
- evaluate different DSHB simulation models to discuss computational effort and simulation time. In this context, the normalized integral of absolute error (NIAE) and the overall processing time are evaluated.

1.8 Master Thesis Outline

This master thesis is organized in six chapters, following the structure presented in Fig. 5. Thus, this master thesis is outlined as follows:

- chapter 2 describes the modeling and control of the DSCC-STATCOM focus on the topology, control strategy, modulation strategies and ES-STATCOM components design.
- chapter 3 introduces the DSHB simulation model of analyze. In this section, the SLS, SLA and VSM models are discussed and compared in different power system service.
- in Chapter 4, the case studies are presented. Additionally, MMC dynamics for charging and discharging process are discussed.
- in Chapter 5, the DSHB ES-STATCOM performance during ancillary services support is explored, considering both frequency and voltage support case studies.
- finally, the conclusions of this work are stated in Chapter 6.

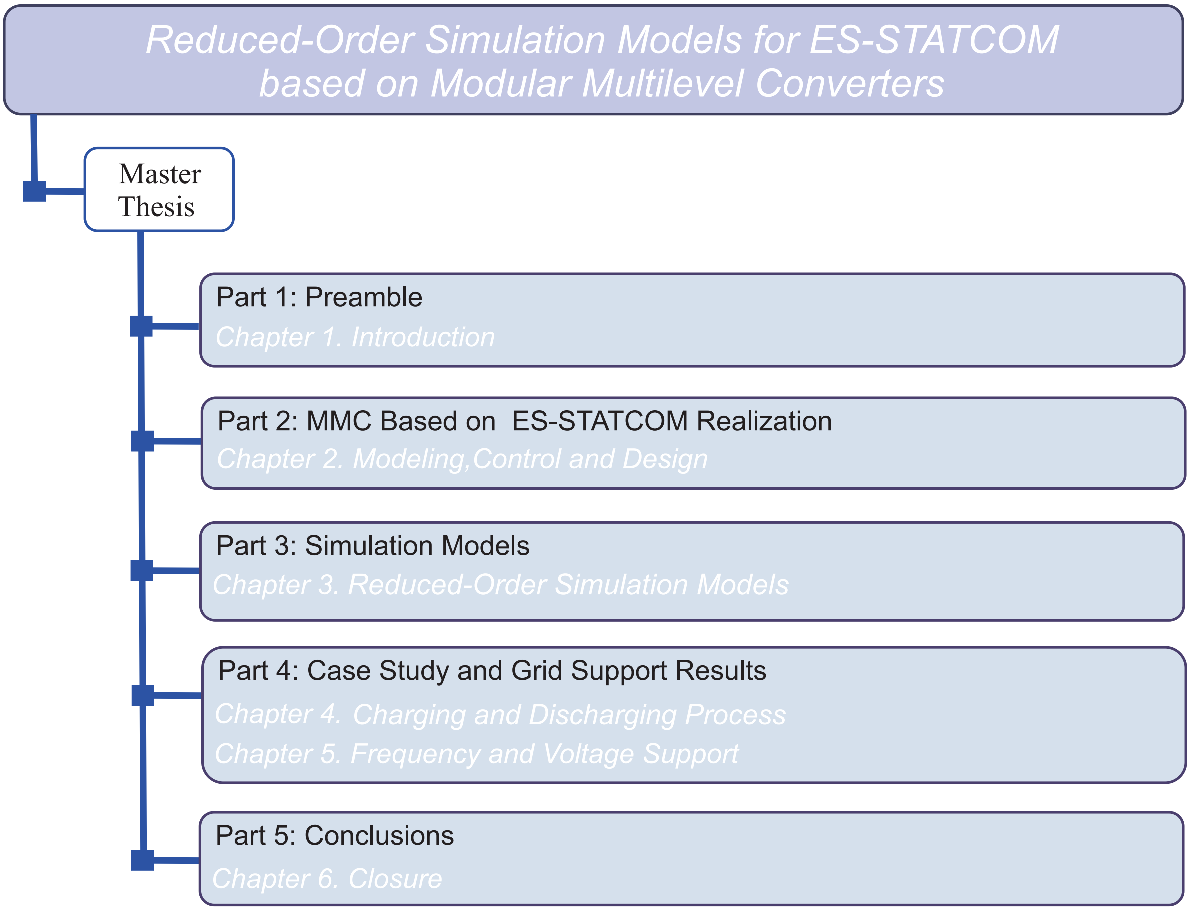

Figure 5 – Structure of the Master Thesis.

1.9 List of Publications

1.9.1 Published Journal Papers

- L. S. Xavier, W. C. S. Amorim, A. F. Cupertino, V. F. Mendes, W. C. d. Boaventura and H. A. Pereira. “Power converters for battery energy storage systems connected to medium voltage systems: a comprehensive review”. BMC Energy 1, 7 (2019) doi:10.1186/s42500-019-0006-5.

- W. C. S. Amorim, D. C. Mendonça, R. O. de Sousa, A. F. Cupertino, H. A. Pereira and R. Teodorescu, “Analysis of Double Star Modular Multilevel Topologies Applied in HVDC System for Grid Connection of Offshore Wind Power Plants”. J Control Autom Electr Syst (2019) doi:10.1007/s40313-019-00542-2.

- A. F. Cupertino, W. C. S. Amorim, H. A. Pereira, S. I. S. Junior, S. K. Chaudhary and R. Teodorescu. “High Performance Simulation Models for ES-STATCOM based on Modular Multilevel Converters”, in IEEE Transactions on Energy Conversion, Early Access. doi: 10.1109/TEC.2020.2967314.

1.9.2 Submitted Journal Papers (under review)

- M. P. M. Combatt, W. C. S. Amorim, E. S. O. Brito, A. F. Cupertino, R. M. , H. A. Pereira. "Design of Parallel Plate Electrocoagulation Reactors Supplied by Photovoltaic System Applied to Wastewater Treatment". Computers and Electronics in Agriculture. 2018.

1.9.3 Published Conference Papers

- W. C. S. Amorim, D. C. Mendonça, J. M. S. Callegari, M. P. Silva, H. A. Pereira and A. F. Cupertino, "Comparison of Current Grid Controllers in a DG Inverter with Grid Harmonic Distortion," 2018 13th IEEE International Conference on Industry Applications (INDUSCON), São Paulo, Brasil, 2018, pp. 194-201.
- R. O. de Sousa, D. C. Mendonça, W. C. S. Amorim, A. F. Cupertino, H. A. Pereira and R. Teodorescu, "Comparison of Double Star Topologies of Modular Multilevel Converters in STATCOM Application". 13th IEEE/IAS International Conference on Industry Application (INDUSCON), São Paulo, Brasil, 2018, pp. 622-629.
- R.O. de Sousa, W.C.S. Amorim, D.C. Mendonça, A.F. Cupertino, L.M.F. Morais and H.A. Pereira, "Thermal Stress Evaluation of a Multifunctional Modular Multilevel Converter - STATCOM Operating as Active Filter". Brazilian Power Electronics Conference (COBEP), Santos, Brasil, 2019.
- R. C. de Barros, J. M. S. Callegari, D. d. C. Mendonca, W. C. S. Amorim, M. P. Silva and H. A. Pereira, "Low-Cost Solar Irradiance Meter using LDR Sensors," 2018 13th IEEE International Conference on Industry Applications (INDUSCON), São Paulo, Brasil, 2018, pp. 72-79.
- D. C. Mendonça, P. R. M. Júnior, W. C. S. Amorim, P. H. G. R. P. Castro, A. G. Torres and K. S. Moreira. "Controle de Posição de um Motor de Indução com Inversor de Frequência e Arduino," 2018 13th IEEE International Conference on Industry Applications (INDUSCON), São Paulo, Brasil, 2018.

2 Modeling, Control and Design

2.1 MMC-based ES-STATCOM

The MMC ES-STATCOM topology studied in this work, called DSHB, is illustrated in Fig. 6 (a) (Akagi, 2011). The SM structure, presented in Fig. 6 (b), is a half bridge topology composed of two Insulated Gate Bipolar Transistor (IGBT) and two diodes. The battery bank is connected in parallel with the SM capacitor. Each battery bank has N_s battery racks in series and N_p parallel battery strings.

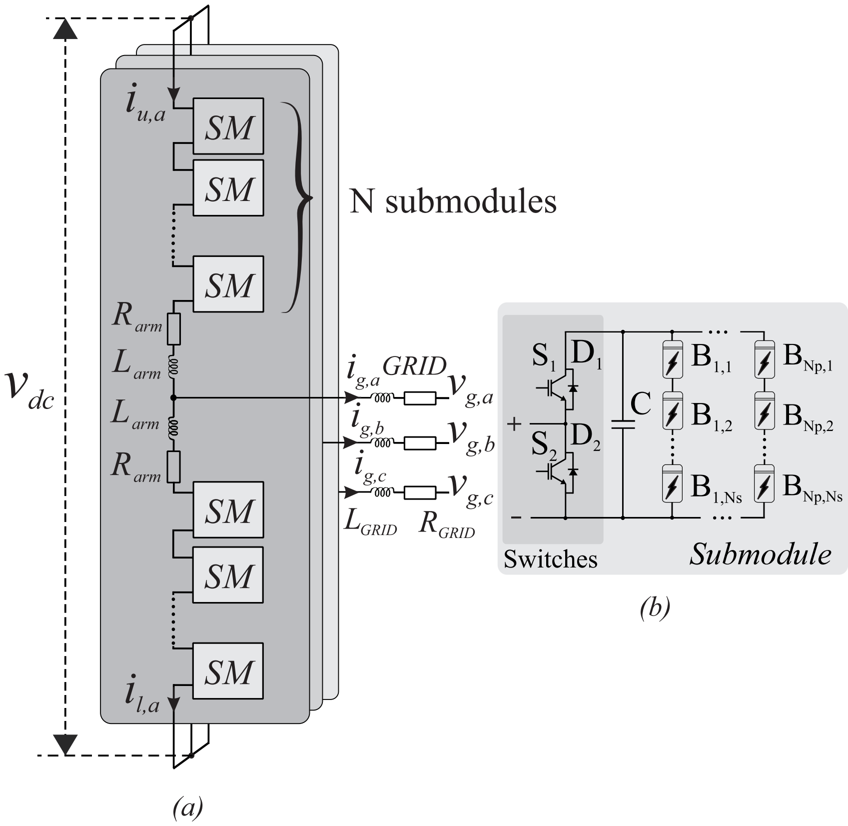

Figure 6 – Basic structure of an DSHB-MMC ES-STATCOM (a) converter structure (b) SM structure.

The upper and lower arms are connected by two arm inductors, forming the converter phase (or called leg). The arm inductor is used to limit the increasing rate of current during faults and reduce the high-order harmonics in the circulating current (Harnefors et al., 2013; Arslan et al., 2018). The arm inductor presents an intrinsic resistance, denoted by R_{arm}.

The converter is connected to the main grid through a three-phase isolation transformer with inductance L_{grid} and resistance R_{grid}. Moreover, $i_{u,n}$ and $i_{l,n}$ are the upper and lower arm currents, respectively, for each phase. The grid voltage and current are represented by $v_{g,n}$ and $i_{g,n}$, respectively, for each phase.

A dc-dc converter can be linked between the cell capacitor and the battery, to mitigate harmonics in the battery current (Ma et al., 2017). However, since dc-dc converters may directly affect the cost and efficiency of the ES-STATCOM, they are not considered in this work.

2.2 DSHB-MMC Dynamics

In MMC based BESS, the batteries can be arranged on dc-link (centralized configuration) or distributed in the SMs (decentralized configuration). In this work, the decentralized configuration is analyzed. Thus, the dc-link bus bars can be designed disregarding short-circuit. This is completely different from an MMC-HVDC system, where there are cables and other devices connected to the converter dc-link and short circuits can happen.

In decentralized configuration, the dc-link current (i_{dc}) is defined by the sum of the upper arm currents or lower arm currents. For this topology configuration, i_{dc} is equal zero. In this sense, the sum of upper or lower arm currents results in:

$$\sum_{n=1}^{3} i_{u,n} = \sum_{n=1}^{3} i_{l,n} = 0. \tag{2.1}$$

In relation to the arm voltages, the instantaneous value synthesized for each arm can be obtained from the insertion index and the instantaneous value of the capacitors voltage or batteries rack in series. Consequently, the inserted voltages can be expressed as:

$$v_{u,n} = \sum_{i=1}^{N} g_{u,n} v_{sm,n}^{i}. \tag{2.2}$$

The output current in DSHB-MMC is referred to as grid current. Based on the arm currents direction present in Fig. 6 (a), the output current is obtained:

$$i_{g,n} = i_{u,n} - i_{l,n}. \tag{2.3}$$

The circulating current ($i_{c,n}$), in MMC, exchange energy between the arms. However, to keep the converter losses and the arm currents at a minimum, the circulating current should be pure dc. The circulating current is calculated for each phase and given by:

$$i_{c,n} = \frac{i_{u,n} + i_{l,n}}{2}. \tag{2.4}$$

Thus, the upper and lower arm currents can be expressed in terms of circulating current and grid current, respectively:

$$i_{u,n} = \frac{i_{g,n}}{2} + i_{c,n}, \tag{2.5}$$

$$i_{l,n} = -\frac{i_{g,n}}{2} + i_{c,n}. \tag{2.6}$$

The output voltage ($v_{g,n}$) and output current ($i_{g,n}$) dynamics can be obtained as follows:

$$v_{s,n} - \left(\frac{L_{arm}}{2} + L_g\right)\frac{di_{g,n}}{dt} - \left(\frac{R_{arm}}{2} + R_g\right)i_{g,n} = v_{g,n}. \tag{2.7}$$

where $v_{s,n}$ is the line-to-neutral voltage synthesized by the DSHB-MMC.

The dynamics of the circulating current per phase is analyzed from the DSHB-MMC internal voltage ($v_{c,n}$), which performs the circulating current control is given by:

$$v_{c,n} = L_{arm}\frac{di_{c,n}}{dt} + R_{arm}i_{c,n}. \tag{2.8}$$

The dynamics of the upper arm voltage ($v_{u,n}$) and lower arm voltage ($v_{l,n}$) is given by:

$$v_{u,n} = v_{c,n} - v_{s,n} + \frac{v_{dc}}{2}. \tag{2.9}$$

$$v_{l,n} = v_{c,n} + v_{s,n} + \frac{v_{dc}}{2}. \tag{2.10}$$

The instantaneous active power exchange by ES-STATCOM is derived from the instantaneous active power exchange by the upper and lower arms. Thus, the instantaneous active power delivered by each arm is given by:

$$p_{u,n} = v_{u,n}i_{u,n} = (v_{c,n} - v_{s,n} + \frac{v_{dc}}{2})(\frac{i_{g,n}}{2} + i_{c,n}), \tag{2.11}$$

$$p_{l,n} = v_{l,n}i_{l,n} = (v_{c,n} + v_{s,n} + \frac{v_{dc}}{2})(-\frac{i_{g,n}}{2} + i_{c,n}), \tag{2.12}$$

which results in:

$$p_{u,n} = v_{c,n}\frac{i_{g,n}}{2} + v_{c,n}i_{c,n} - v_{s,n}\frac{i_{g,n}}{2} - v_{s,n}i_{c,n} + v_{dc}\frac{i_{g,n}}{4} + v_{dc}\frac{i_{c,n}}{2}, \tag{2.13}$$

$$p_{l,n} = -v_{c,n}\frac{i_{g,n}}{2} + v_{c,n}i_{c,n} - v_{s,n}\frac{i_{g,n}}{2} + v_{s,n}i_{c,n} - v_{dc}\frac{i_{g,n}}{4} + v_{dc}\frac{i_{c,n}}{2}. \tag{2.14}$$

In decentralized configuration the circulating current ($i_{c,n}$) is approximately zero, since the dc-link is not present. In addition, the internal voltage ($v_{c,n}$) is approximately zero in order to keep the circulating current in zero. Then, the instantaneous active power can be simplified to:

$$p_{u,n} = \underbrace{v_{c,n}\frac{i_{g,n}}{2}}_{\approx 0} + \underbrace{v_{c,n}i_{c,n}}_{\approx 0} - \underbrace{v_{s,n}\frac{i_{g,n}}{2}}_{dc+ac\ comp.} - \underbrace{v_{s,n}i_{c,n}}_{\approx 0} + \underbrace{v_{dc}\frac{i_{g,n}}{4}}_{ac\ comp.} + \underbrace{v_{dc}\frac{i_{c,n}}{2}}_{\approx 0}, \tag{2.15}$$

$$p_{l,n} = -\underbrace{v_{c,n}\frac{i_{g,n}}{2}}_{\approx 0} + \underbrace{v_{c,n}i_{c,n}}_{\approx 0} - \underbrace{v_{s,n}\frac{i_{g,n}}{2}}_{dc+ac\ comp.} + \underbrace{v_{s,n}i_{c,n}}_{\approx 0} - \underbrace{v_{dc}\frac{i_{g,n}}{4}}_{ac\ comp.} + \underbrace{v_{dc}\frac{i_{c,n}}{2}}_{\approx 0}. \tag{2.16}$$

The sum of equations (2.15) and (2.16) results in:

$$p_{u,n} + p_{l,n} = -v_{s,n}i_{g,n}. \tag{2.17}$$

The power delivered to the grid ($p_{g,n}$) is equal to the sum of power delivered by each arm. In addition, half of the power is processed by each arm, based on equations (2.15) and (2.16), which implies in equal distribution between the arms. Conversely, the ac output voltage in DSHB can be expressed as:

$$v_{s,n} \approx v_{g,n} = \widehat{V}cos(\omega_n t + \theta_v + \delta), \tag{2.18}$$

where $\widehat{V}$ is the peak of grid voltage, ω_n is the nominal grid angular frequency, θ_v is the phase angle of each grid phase ($\theta_v \in \left\{-\frac{2\pi}{3}, 0, \frac{2\pi}{3}\right\}$) and δ is the grid voltage angle.

Similarly, the grid current can be expressed as:

$$i_{g,n} = \widehat{I}cos(\omega_n t + \theta_v + \phi), \tag{2.19}$$

where $\widehat{I}$ is the peak of grid current and ϕ is the grid current angle.

From the equations (2.18) and (2.19), the instantaneous active power delivered by each phase can be expressed as:

$$p_{g,n} = v_{g,n}i_{g,n} \approx v_{s,n}i_{g,n}. \tag{2.20}$$

Finally, replacing equation (2.17) in (2.20), the instantaneous active power delivery by each phase is given by:

$$p_{g,n} = -(p_{u,n} + p_{l,n}) = \underbrace{\frac{\widehat{V}\widehat{I}}{2}cos(\delta - \phi)}_{\overline{p}_{g,n}} + \underbrace{\frac{\widehat{V}\widehat{I}}{2}cos(2\omega_n t + 2\theta_v + \phi + \delta)}_{\widetilde{p}_{g,n}}. \quad (2.21)$$

From the instantaneous active power, the average instantaneous power term ($\overline{p}_{g,n}$) exchange effective active power between the grid and DSHB-MMC. In addition, the instantaneous active power equation can be formulated in terms of modulation index (m), that for DSHB-MMC topology is given by:

$$m = 2\frac{\widehat{V}}{V_{dc}}, \quad (2.22)$$

which results in:

$$p_{g,n} = \frac{mV_{dc}\widehat{I}}{4}cos(\delta - \phi) + \frac{mV_{dc}\widehat{I}}{4}cos(2\omega_n t + 2\theta_v + \phi + \delta). \quad (2.23)$$

2.3 Control Strategy

ES-STATCOMs need to deal with different power exchanges in different times of operation. The MMC ES-STATCOM can charge or discharge the battery bank to provide ancillary services. For this reason, the control needs to compute the converter control mode, that provide the grid current reference to grid current control.

Fig. 7 shows the control strategy of a MMC based ES-STATCOM used in the present work. The control objectives can be classified as:

- grid Current Control;
- circulating Current Control;
- SOC Balancing Control.

The grid current control is implemented in stationary reference frame ($\alpha\beta$) coordinates. In this control, Proportional Resonant (PR) controllers are employed.

The circulating current control inserts damping in the converter dynamic response, suppress second harmonic and performs the SOC control exchange energy to batteries (Li et al., 2018). Thus, these control is implemented based on a PR controller that computes the MMC internal voltage $v_{c,n}$.

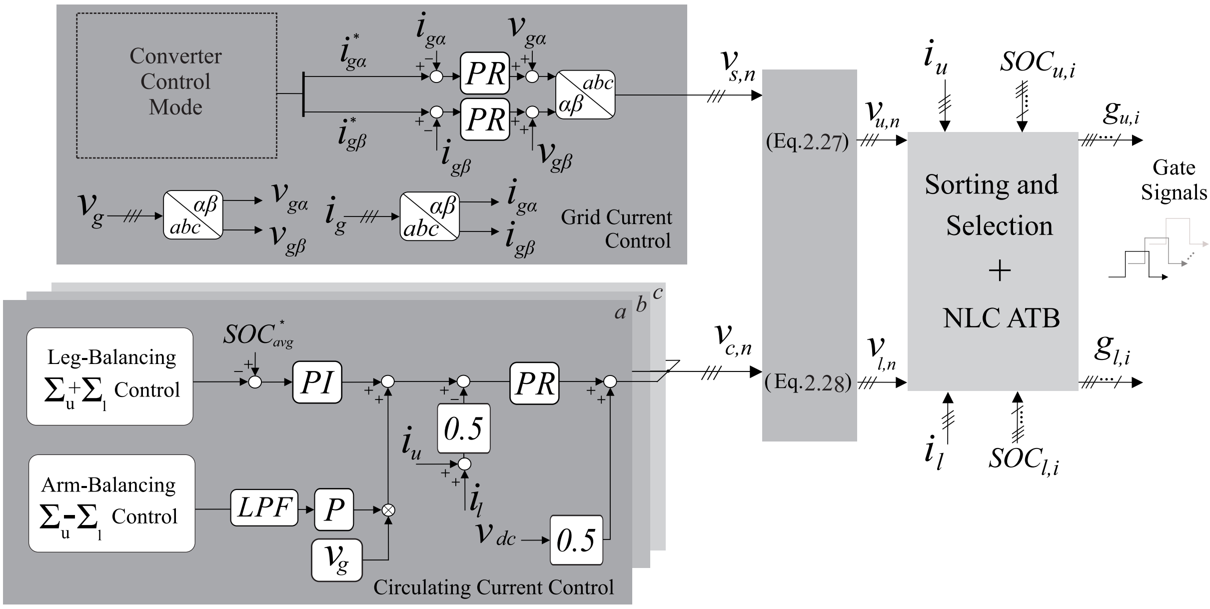

Figure 7 – ES-STATCOM control strategy with grid current control and circulating current control.

The reference $i^*_{c,n}$ is obtained using a LPF of $i_{c,n}$, which is employed using a second order Butterworth filter. In addition, to compensate the 2-nd harmonic component present in the circulating current, a resonant controller is implemented in the control.

The circulating current can be used to reach the SOC balancing without affecting the converter output current. This characteristic is very important during the frequency support mode.

The leg-balancing control employs Proportional Integral (PI) controllers that compute the dc portion of the circulating current to guarantee that all legs present the same average SOC. The average SOC in n-phase is given by:

$$SOC_{n,avg} = \frac{1}{2N}\left(\sum_{i=1}^{N} SOC_{u,i} + \sum_{i=1}^{N} SOC_{l,i}\right), \tag{2.24}$$

where $SOC_{u,i}$ and $SOC_{l,i}$ are the SOC of the i-th SM of the upper and lower arm, respectively, and N is the number of SMs per arm. The reference of the leg-balancing control is given by:

$$SOC^*_{avg} = \frac{1}{3}\sum_{j=1}^{3} SOC_{j,avg}. \tag{2.25}$$

where $SOC_{j,avg}$ is the average SOC of the j-th converter phase.

For the arm-balancing control, the difference between the average SOC of the upper and the lower arms, SOC_{diff}, is computed for each n-phase by means of a LPF, as follows:

$$SOC_{n,diff} = \frac{1}{N}\left(\sum_{i=1}^{N} SOC_{u,i} - \sum_{i=1}^{N} SOC_{l,i}\right). \tag{2.26}$$

The reference of the arm-balancing control is zero, to guarantee a balanced SOC in the upper and lower arm of each phase. A proportional controller is used to compute the amplitude of the fundamental frequency circulating current. This signal is multiplied by the grid voltage.

The normalized reference signals per n-phase are given by:

$$v_{u,n} = \frac{v_{c,n}}{V_{sm}^*} - \frac{v_{s,n}}{NV_{sm}^*} + \frac{1}{2}, \tag{2.27}$$

$$v_{l,n} = \frac{v_{c,n}}{V_{sm}^*} + \frac{v_{s,n}}{NV_{sm}^*} + \frac{1}{2}. \tag{2.28}$$

where $v_{s,n}$ is the voltage synthesized in the converter output (drives i_g), $v_{c,n}$ is the converter internal voltage (drives i_c), v_{dc} is the instantaneous dc-link voltage, v_{sm}^* is the SM voltage reference and N is the total number of SMs. The injection of 1/6 of third harmonic is considered in normalized reference signals to increase the linear region of the modulator (Zhao et al., 2019).

Finally, the insertion indexes for upper and lower arms are given by:

$$n_{u,n} = \frac{v_{u,n}}{Nv_{sm}^*}, \tag{2.29}$$

$$n_{l,n} = \frac{v_{l,n}}{Nv_{sm}^*}, \tag{2.30}$$

Fig. 8 presents the control strategy to perform the charging of batteries, in SOC global control, and the discharging of batteries, during a frequency support. In this work, a frequency regulation study is performed as an ancillary service provided by the ES-STATCOM. This frequency support is done through a frequency droop control, illustrated in Fig. 8. The SOC global control performs the control of average global SOC using a PI controller, computing the SOC global among all converter phases. Besides, the frequency regulation scheme, a curve of frequency droop is used to give the reference of active power injection.

This structure controls the active and reactive power exchange with the electrical grid. The grid current reference in stationary frame is given by:

$$i_{g,\alpha\beta}^* = i_{gp,\alpha\beta}^* + i_{gq,\alpha\beta}^*, \tag{2.31}$$

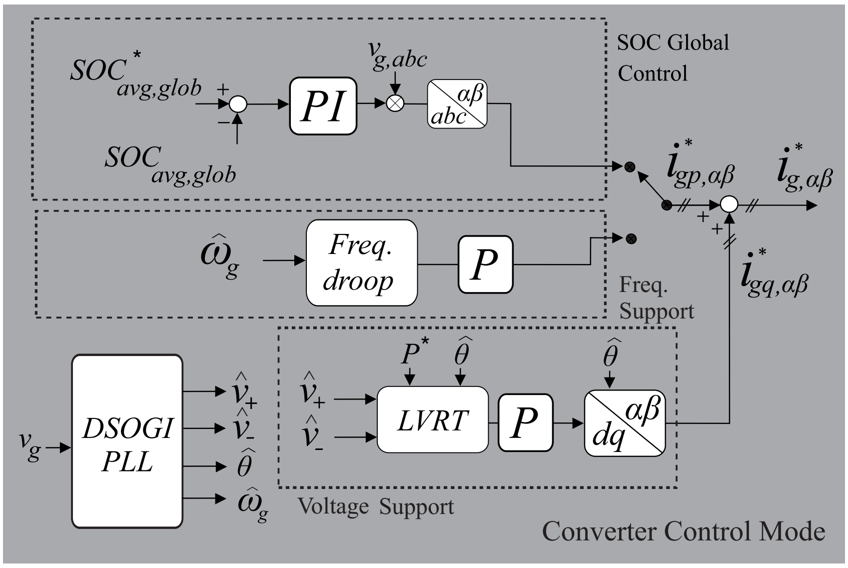

Figure 8 – ES-STATCOM control strategy for converter control mode.

where $i^*_{gq,\alpha\beta}$ is the q-component reference current in stationary frame of grid current component that causes the reactive power transfer. This reference is computed based on the reactive power requirement or voltage support demand (Sharifabadi et al., 2016). In addition, $i^*_{gp,\alpha\beta}$ is the p-component reference grid current in stationary reference frame, that causes the active power transfer. The latter depends on the ES-STATCOM control mode: SOC global control or frequency regulation.

Under normal grid conditions, $i^*_{gp,\alpha\beta}$ is computed by the global SOC control, which calculates the amount of active power to charge the batteries to reach the reference SOC^*. The global SOC control is implemented per phase and is based on PI controllers. Usually, these controllers are saturated in a fraction of the rated current (e.g. 10 % of nominal grid current). Under such conditions, the charging process of the batteries might not affect the electric grid.

2.4 Modulation Strategies

The semiconductor switches of a HB SMs can synthesize different levels of voltage. HB has two possible states for the two gate switches, S_1 and S_2, plus a blocking state, where both are disabled. HB presents two states for the semiconductor switches, producing levels 0 and $+v_c$, as presented in Tab. 2.

MMC ES-STATCOMs address challenges associated with maintaining the SOC to reach a nominal SOC per SM and per phase. The nearest-level control (NLC) is a modulation method, applicable to an extensive number of output voltage levels (Zeng et al., 2015; Ghat; Shukla; Mathew, 2017). The NLC modulation samples the SMs insertion index of the upper arm ($n_{u,n}$), the arm currents ($i_{u,n}$ and $i_{l,n}$) and SMs SOC ($SOC^i_{u,n}$) at

Table 2 – Switching States of the HB Switches

State	S_1	S_2	v_{sm}
1	1	0	$+v_c$
2	0	1	0
3	0	0	blocked
4	1	1	0

a rated sampling frequency (f_s). The sampling frequency is one of the main impact factors of the NLC modulation, since it is possible to carry out the SOC balancing.

The NLC and sorting and selection (S&S) algorithm give flexibility to the method of controlling the fluctuation of SOC in SMs. Therefore, some of the most widespread forms found in the literature are NLC algorithms with conventional sorting, cell tolerance band (CTB) and average tolerance band (ATB) (Sharifabadi et al., 2016). ATB presents a lower equivalent switching frequency, compared with PWM, which affects the semiconductor switching losses. Regarding the modulation strategy, the nearest level control with ATB is employed in this work (Sharifabadi et al., 2016).

Fig. 9 shows a flowchart of SOC balancing for DSHB applied to NLC modulation method. The reference voltages for SMs insertion are normalized, which produces just positive levels in HB. After sampling the SOC of all SMs, the algorithm sample the arm current. The NLC ATB maintains the SMs insertion list comparing the instantaneous SOC of all SMs with the average SOC per arm ($\frac{1}{N}\sum_{i=1}^{N} SOC_{u,n}^{i}$). Thus, the instantaneous SOC of all SMs must be between the limits values: $\delta_{lim,l}$ (-0.01 or 99% of SOC_{sm}^{*}) and $\delta_{lim,u}$ (+0.01 or 101% of SOC_{sm}^{*}). If all SM SOC compared with the average SOC value per arm are between the upper and lower SOC limits or the actual insertion index is the same of the previous insertion index, the NLC maintain the last insertion configuration (last SMs insertion list) (Sharifabadi et al., 2016).

In this sense, if it is necessary to update the SMs insertion list, the NLC algorithm analyze the arm current. In case of positive arm current, $n_{u,n}$ SMs with the lowest SOC in the arm are inserted, and the others ($N - n_{u,n}$) are bypassed. On the other hand, in case of negative arm current, the SMs inserted present the highest SOC. Thus, the S&S algorithm only updates the list of SMs to be entered if the instantaneous SOC values exceed the limits $\delta_{lim,l}$ or $\delta_{lim,u}$, or if the actual $n_{u,n(actual)}$ insertion index changes from the previous value $n_{u,n(previous)}$. The NLC algorithm is the same for the lower arms.

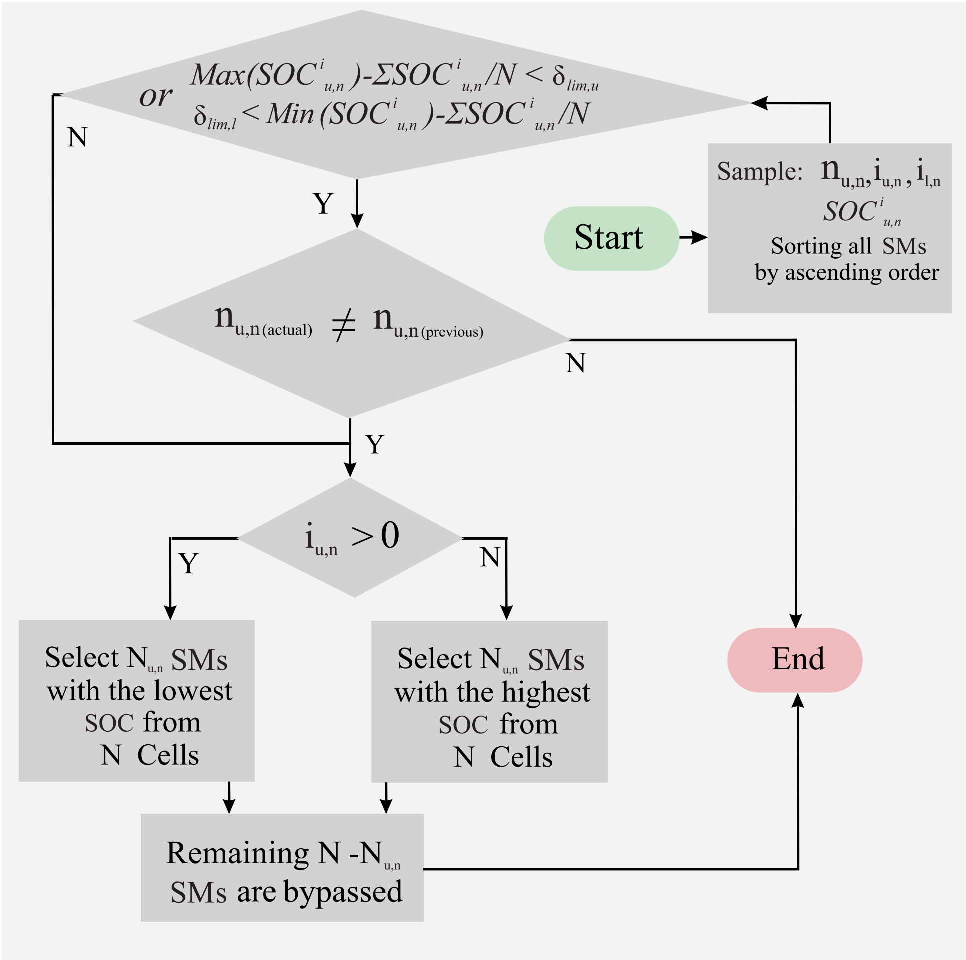

Figure 9 – Flowchart of SOC balancing algorithm.

2.5 DSHB-MMC ES-STATCOM Design

The minimum dc-link voltage required for MMC ES-STATCOM operation assuming 1 pu of reactive current, a grid variation and a voltage in equivalent output impedance, result in:

$$v_{dc,min} = \frac{2\sqrt{2}}{m\sqrt{3}} V_g \left(1 + \Delta V_g + x_{eq}\right), \tag{2.32}$$

where V_g is the rms line-to-line output voltage, ΔV_g is the maximum assumed grid voltage variation in pu, m is the maximum modulation index and x_{eq}, given by equation (2.33), is the per unit equivalent output inductance of the converter. The minimum dc-link voltage considered the case of higher converter output voltage: inductive operation. In this case, the sum of output voltage occurs between the arm reactance voltage and the grid voltage (the arm resistance and transformer resistance are disregarded). In addition, the modulation index is considered, inversely proportional to the minimum dc-link voltage required.

$$x_{eq} = 0.5x_{arm} + x_g, \tag{2.33}$$

where the arm impedance and grid transformer impedance, in pu, are expressed by x_{arm} and x_g, respectively.

The voltage across each SM is proportional to the number of series (N_s) batteries rack. Fig. 10 presents a typical Open-Circuit Voltage (OCV) versus SOC curve of a Li-ion battery (Meng et al., 2018). As observed, the cell battery voltage variation is considerable and must be taken into account in the converter design. The number of battery racks in series is expressed by:

$$N_s = floor\left(\frac{V_{sm}^*}{V_{b,max}}\right), \tag{2.34}$$

where $V_{b,max}$ is the maximum battery rack voltage. The nominal SM voltage is a function of the semiconductor device voltage class. Thus, N_s is rounded using the *floor* function to not exceed V_{sm}^*.

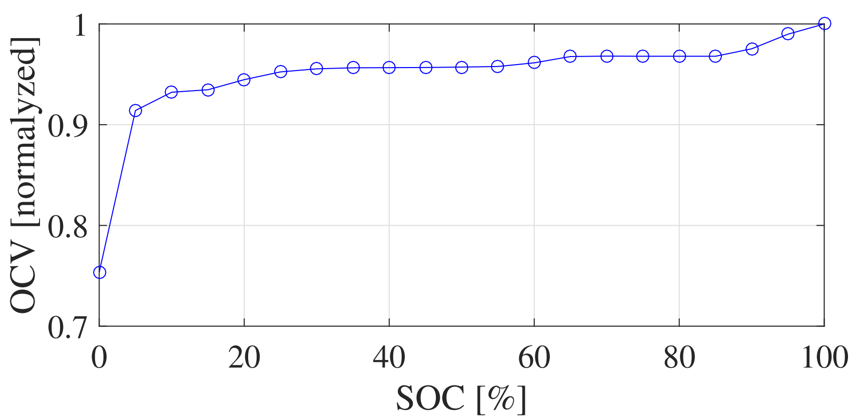

Figure 10 – Typical OCV versus SOC curve for a Li-ion battery (Meng et al., 2018).

To achieve the output voltage requirement, the numbers of SMs is computed considering the minimum dc-link voltage and the minimum battery rack voltage, as follows:

$$N = ceil\left(\frac{v_{dc,min}}{N_s V_{b,min}}\right), \tag{2.35}$$

where $V_{b,min}$ is the minimum battery rack voltage. The *ceil* function ensures the synthesis of minimum output voltage.

The number of parallel battery strings must fulfill two requirements:

1. Converter rated power;

2. Converter total energy storage.

The first criterion assumes that the battery rack must have capacity to inject the rated power of the converter into the grid. Accordingly:

$$N_{p,power} = ceil\left(\frac{P_n}{6NN_sP_{b,min}}\right), \tag{2.36}$$

where P_n is the nominal converter power and $P_{b,min}$ is the minimum battery rack power, given by:

$$P_{b,min} = V_{b,min}C_{bat,r}C_{bat,n}, \tag{2.37}$$

where $C_{bat,r}$ is the proportional factor of recommended discharging rate and $C_{bat,n}$ is the battery nominal capacity.

The second criterion assumes that the batteries must fulfill the energy storage requirements for the application. Accordingly:

$$N_{p,energy} = ceil\left(\frac{100E_n}{6E_{n,bat}NN_s(SOC_{max} - SOC_{min})}\right), \tag{2.38}$$

where E_n is the total energy storage requirement and $E_{n,bat}$ is the battery rack energy storage requirement. In addition, SOC_{max} and SOC_{min} are the maximum and minimum allowed SOC in all SMs, respectively.

In order to accord the two requirements, the number of parallel battery strings is given by:

$$N_p = \max(N_{p,power}; N_{p,energy}). \tag{2.39}$$

Once the battery bank is dimensioned, it is necessary to design the SM capacitance, arm inductance and semiconductors devices (IGBTs and diodes). The SM capacitance is defined to provide an energy storage of $W = 40$ kJ/MVA, as derived in (Cupertino et al., 2018). Therefore, the SM capacitance is computed as follows:

$$C = \frac{2WS_n}{6000N(V_{sm}^*)^2}, \tag{2.40}$$

where W is the energy storage requirement, in kJ/MVA, and S_n is the converter rated apparent power. The design considers the capacitance inclusion, as the converter can only be marketed for an exclusive application of STATCOM and the batteries, in this case, are not considered in the SM. In addition, the capacitance can filter part of the low frequency harmonics in battery current which affects the battery lifetime.

The arm inductance is designed by the maximum line-to-line voltage and the arm impedance in pu, expressed by (Harnefors et al., 2013):

$$L_{arm} = x_{arm} \frac{V_g^2}{2\pi f_n S_n}, \tag{2.41}$$

where x_{arm} is the per unit value of arm reactance and f_n is the nominal grid frequency.

Finally, the maximum value of arm current is useful for the specification of the arm inductors and semiconductors devices. Since the decentralized storage is assumed, the average value of circulating current is zero under balanced conditions. Therefore, the maximum value of arm current is given by:

$$\max(i_u) = \frac{\max(i_g)}{2} = \frac{S_n}{\sqrt{6} V_g}. \tag{2.42}$$

2.6 Grid Code Requirements

Under grid frequency disturbances, the converter might operate in the frequency control mode. In this case, $i^*_{gp,\alpha\beta}$ is computed to inject the active power defined by a frequency droop curve. Fig. 11 presents a typical droop curve for primary frequency control, regulated by (CIGRE, 2014). As observed, a deadband of ± 10 mHz in the nominal grid frequency is considered.

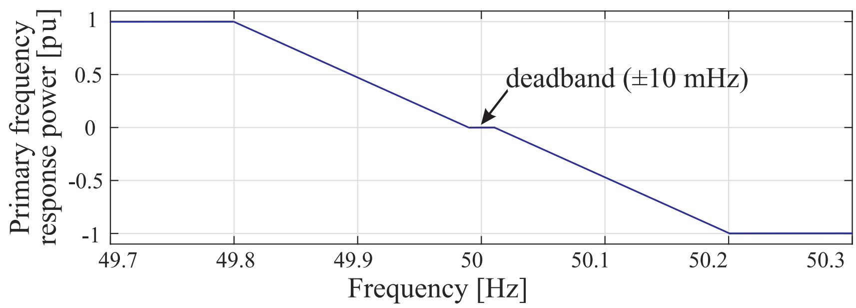

Figure 11 – Typical primary frequency control droop curve.

Under symmetrical and asymmetrical grid faults, the ES-STATCOM needs to inject reactive current in order to support the voltage recovery. For this reason, many grid codes such as (VDE, 2012; NATIONAL GRID ELECTRICITY TRANSMISSION, 2017; EIRGRID, 2018) require a continuous connection between the generation systems (as a offshore wind farm) in the point of common coupling (PCC) in case of grid voltage disturbance, for a minimum time. In this work, it is studied a case of a voltage support, considering a symmetrical grid fault. During the grid fault, the MMC control needs to avoid output overcurrent or dc overvoltage. Thus, it is expected the injecting of positive and/or negative sequence reactive current proportional to the positive and negative sequence of the grid voltage. In this situation, the LVRT is responsible to give the reference of positive and negative sequence reactive current (i_q^+ and i_q^-, respectively)

The adopted LVRT is composed for two components, that is presented in Fig. 12 (a) for the positive sequence (PS) and Fig. 12 (b) for the negative sequence (NS). In the grid fault, the positive sequence of grid voltage gives the reference to positive sequence reactive current, as presented in Fig. 12 (a). In the positive sequence of grid voltage, there is a $\pm 10\%$ deadband. In addition, there is a $+5\%$ deadband for negative sequence of grid voltage, as presented in Fig. 12 (b).

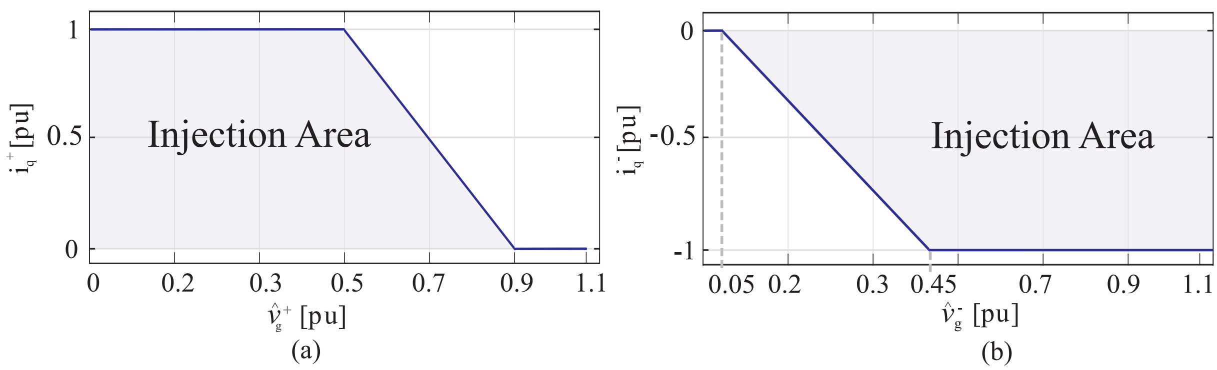

Figure 12 – LVRT reactive current injection curve: (a) PS-LVRT (b) NS-LVRT (Based on (VDE, 2012)).

The converter control mode scheme that gives the reference of grid current is implemented in stationary reference frame ($\alpha\beta$) coordinates, that is results of the sum of active power component ($i_{gp,\alpha\beta}$) and the reactive power component ($i_{gq,\alpha\beta}$), as present in equation (2.31). Thus, ($i_{gq,\alpha\beta}$) is computing by a LVRT component that provide reactive support in case of symmetrical and asymmetrical grid fault. The dq components of grid voltage (v_g): $\widehat{v}_+$, $\widehat{v}_-$, $\widehat{\omega}_g$ and $\widehat{\theta}$ are derived from a dual second-order generalized integrator-phase locked loop (DSOGI-PLL), as presented in Fig. 8 (Rodriguez et al., 2007).

2.7 Chapter Conclusions

In this chapter the topology, modeling, control and modulation strategy for a DSHB were discussed. In addition, an ES-STATCOM based on DSHB-MMC design were presented to attend the required ratings. Thus, the DSHB design take in account the converter energy requirement, especially for batteries and capacitors components.

As observed, the MMC structure presented a high number of components, as capacitors, semiconductors devices, inductors and batteries. Usually, this converter is employed with hundreds or thousands of SMs. In this sense, a considerable computational effort is necessary to simulate the dynamic response of DSHB, especially if the study consider the converter integrated into the power system.

Generally, reduced-order models play an important role in the simulation of MMC-based ES-STATCOM system, after all, the process of charging and discharging require long time of simulation. For this reason, in the next chapter the reduced-order models for MMC ES-STATCOM are evaluated.

3 Reduced-Order Simulation Models

The high number of SMs in an MMC topology introduces challenges in simulation of dynamic response of converter. In addition, power systems simulations deals with models for ES-STATCOM, transformers, transmission systems, among others (Gnanarathna; Gole; Jayasinghe, 2011; Rohner; Weber; Bernet, 2011; Jianzhong Xu et al., 2013). Besides, the ES-STATCOM model needs to compute the converter output current, output voltage, circulating current and SOC estimation for each SM, requiring a considerable computational effort. In power system simulation, the degree of detail of MMC model in an grid support analyzes, as faults inside or outside the converter, voltage stability, frequency stability, and others, may lead to an averaged or reduced-order simulation model (Sato; Igarashi, 2016; Zhang; Shan; Jatskevich, 2017; Gu; Bottrell; Green, 2018; Lopez et al., 2018; Hao et al., 2019). Generally, the models of interest need to give a similar dynamic behavior of the studied variables. These simulation models can be divided in two groups (Sharifabadi et al., 2016):

- mathematical Equation Solvers (MES), as Matlab, Mathematica, Maple, and others;
- circuit Simulators (CS), as PLECS, Simulink, PSIM, PSCAD, PSpice, and others.

The MES group aggregates several equations which lead to a more abstract interpretation of the model. Generally, the equations are defined as linear transfer functions and state-space form. In terms of vectorization, the implementation of MES is effortless, what is an advantage in case of multilevel converters topologies, such as MMC. However, in a power system, it is required a high number of equations. In this sense, CS are more intuitive for the circuit and control implementation. In addition, the computational effort is smaller, compared with MES.

In this sense, this work benchmarks three MMC ES-STATCOM simulation models: SLS, ALA and VSM, considering CS model developed in software PLECS. Each reduced-order simulation model is approached based in different control strategies. In this chapter, it is discussed the battery rack model and the MMC ES-STATCOM reduced-order simulation model.

3.1 DSHB-MMC ES-STATCOM Simulation Models

The simulation of a DSHB-MMC ES-STATCOM can be done with different degrees of detail, in order to simplify the converter characteristics, either by SM, as in SLS, by arm, as in ALA or by phase, as in VSM. Through equivalent models of semiconductor devices in CS, the Submodule Semiconductors Switches (SSS) model is realized. This model aims to be closer to the physical converter characteristics, due to the high level of detail of the components representation. In this sense, the next subsections present the modeling and control of the reduced-order models comparing with the SS model.

3.1.1 Submodule Semiconductors Switches (SSS) Model

The SSS model is illustrated in Fig. 13(a). This model assumes the representation of the SMs using semiconductors devices model, as IGBTs and diodes. Thus, the SM is composed by the equivalent representation of semiconductors devices, as illustrated in Fig. 13(b). The SSS model takes into account the converter switches, individual capacitance C and the equivalent model of the battery racks $B_{eq,SSS}$, as shown in Fig. 13(c).

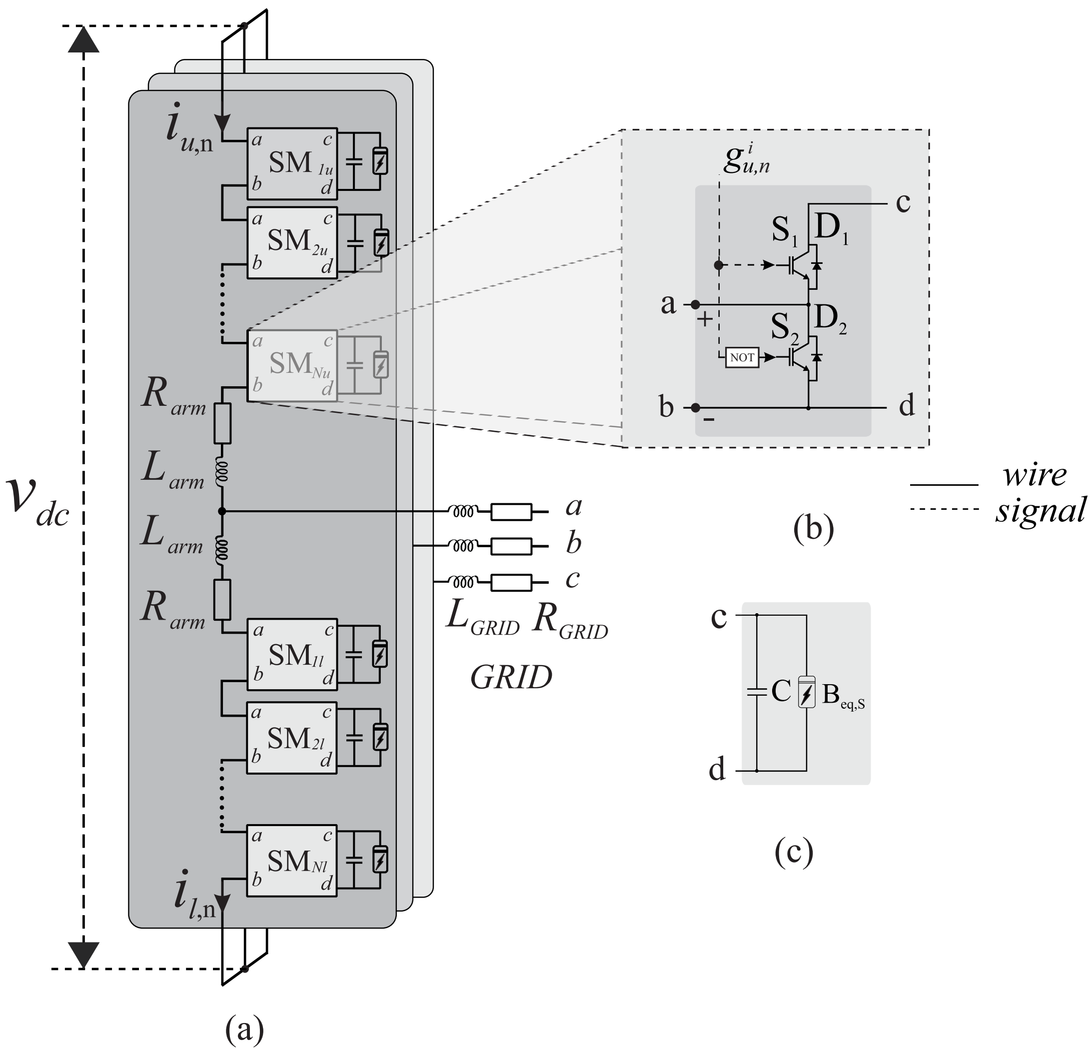

Figure 13 – Submodule Semiconductors Switches (SSS) (a) equivalent model (b) submodule structure (c) capacitor and battery racks arrangement.

The representation of IGBTs and diodes are able to represent the conduction and switching losses, since the data of losses extracted from the semiconductors datasheets are implemented. Due to the transients and losses characteristics in semiconductors devices, this model is appropriated to study internal fault, semiconductors devices losses, capacitors balancing, among others.

3.1.2 Submodule-Level Switched (SLS) Model

The SLS model is illustrated in Fig. 14(a). This model can be used to study the dynamics of each SM. The gate signals computed by the modulation strategy define the insertion or bypass of each SM (Saad; Dennetière; Mahseredjian, 2016). Voltage and current controlled sources are employed to represent the switching characteristics of each device, as illustrated in Fig. 14(b). The SLS model takes into account the effect of the converter switches, individual capacitance C and the aggregated model of the battery racks $B_{eq,SLS}$, as shown in Fig. 14(c). The control strategy applied in SLS model is the same applied in the Fig. 7.

The considerable number of components in SLS leads to high computational burden in ES-STATCOMs applications with high number of SMs (Sharifabadi et al., 2016). Indeed, the complexity of this model increases with the number of SMs (N). Furthermore, since the switching events are represented, small sampling times are usually employed.

The SLS model is used to studies focusing on capacitor balancing methods and for power losses evaluation (Sharifabadi et al., 2016). As well as in SS model, the SLS model can be used for computing the switching and conduction losses, by the gate signals $g_{u,l}$ and SM current $i_{u,n}$, that is calculated by look-up tables extracted from the semiconductors datasheets.

Nevertheless, the converter switching process is one of the factors that limit the increase of the simulation step size, which is required in long simulation studies (Pereira et al., 2014). For this reason, average models are frequently employed to reduce the simulation time by neglecting the switching details. Thus, average models can be employed to summarize converter arms (as ALA model) or converter phase (as VSM model). These average models are discussed in the next subsections.

Despite the advantages of the SSS model, this model requires a high computational effort for simulations involving studies in a power system. Since this work proposes a study of reduced-order models, the SSS model will not be addressed in the case studies.

3.1.3 Arm-level Averaged (ALA) Model

The ALA model is presented in Fig. 15 (a). This model assumes ideal operation of the converter with equal capacitors and battery racks. In addition, aggregates the individual capacitor voltage in the sum of capacitor voltages (Saad et al., 2014). Each converter arm is represented by a controlled ideal voltage source, as presented in Fig. 15

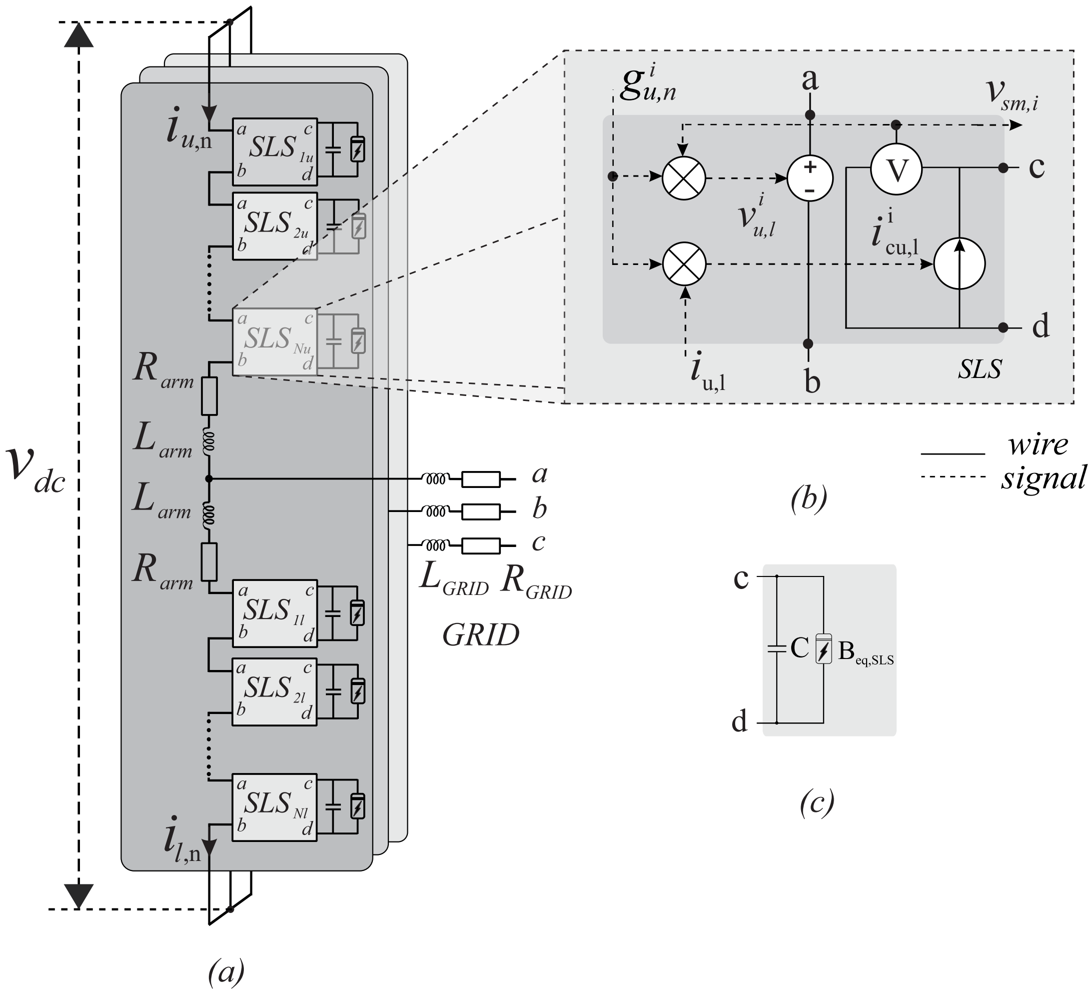

Figure 14 – Submodule-Level Switched Model (SLS) (a) equivalent model (b) submodule structure (c) capacitor and battery racks arrangement.

(b). The output voltage changes according to the insertion index $n_{u,n}$ and $n_{l,n}$, which is computed by equation (2.29) and equation (2.30), respectively. This model represents the capacitors and battery rack dynamics through equivalent models, defined as C_{eq} and B_{eq}, as presented in Fig. 15 (c). The control strategy applied in SLS model is the same applied in the Fig. 7, where the Leg-Balancing and Arm-Balancing are computed considering the SOC estimation per arm.

The equivalent capacitance and battery model parameters can be evaluated as follows. Each SM voltage is based on the following dynamic equation:

$$C\frac{dv_{sm,i}}{dt} + i_{bat,i} = g^i_{u,n} i_{u,n}. \tag{3.1}$$

where $i_{bat,i}$ is the battery current in the i-th SM, $g^i_{u,n}$ is the gate signal to the i-th SM on n-phase and $v_{sm,i}$ is the SM voltage of the i-th SM.

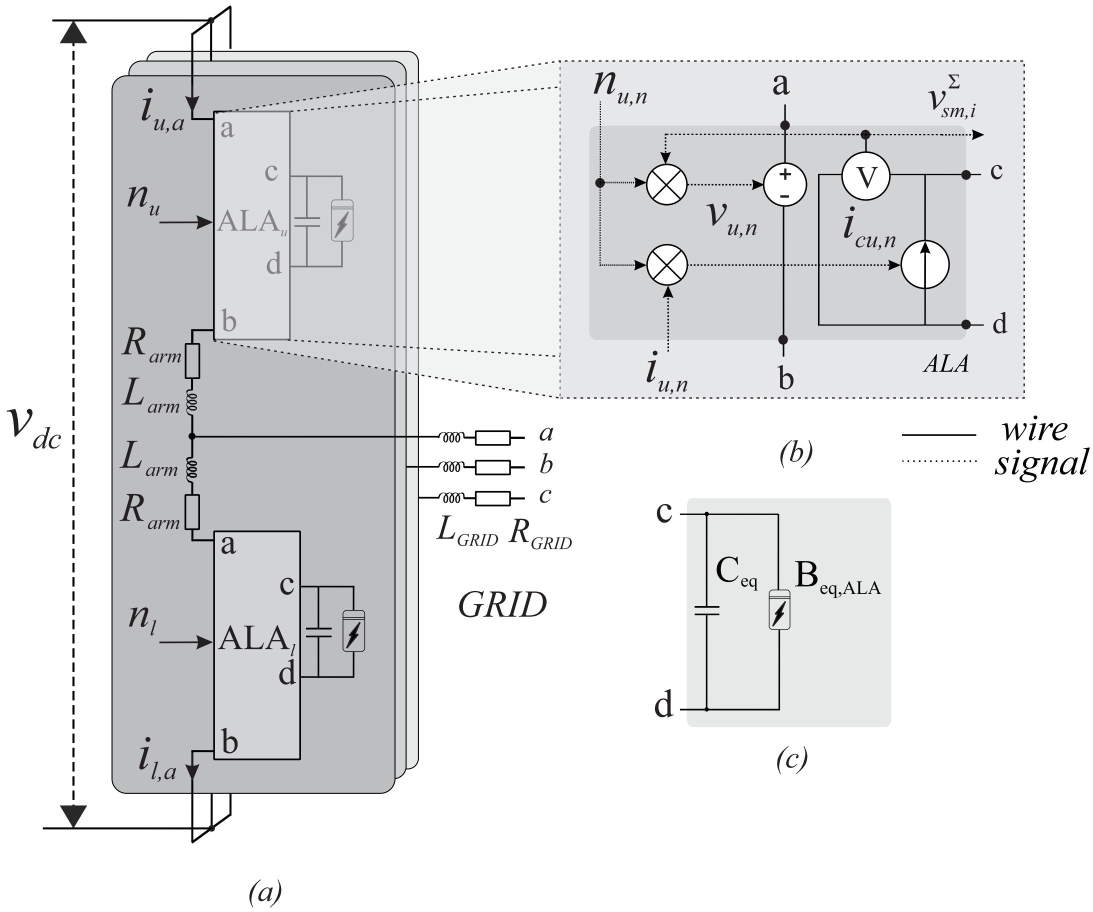

Figure 15 – Arm-Level Averaged Model (ALA) (a) equivalent model (b) arm equivalent structure (c) equivalent capacitor and battery rack arrangement.

Summation over all N capacitors results in:

$$C\sum_{i=1}^{N}\frac{dv_{sm,i}}{dt}+Ni_{bat,i}=i_{u,n}\underbrace{\sum_{i=1}^{N}g^{i}_{u,n}}_{n_{u,n}}, \tag{3.2}$$

which can be rewritten as

$$\frac{C}{N}\frac{dv^{\Sigma}_{sm,i}}{dt}+i_{bat,i}=i_{u,n}n_u, \tag{3.3}$$

where $v^{\Sigma}_{sm,i}$ is the sum of capacitor voltages in the arm.

Based on equation (3.3), the term related to the battery current remains the same in the arm average dynamics. This fact indicates that the number of parallel battery strings in the average and individual SMs are the same. The equation (3.3) indicates that $C_{eq} = \dfrac{C}{N}$. The SOC of each arm can be estimated through the aggregated battery rack model.

The advantages of the ALA model is the reduction in the computational processing time and the simulation is independent of the number of SMs. Besides, it represents the sum of capacitor voltages and output current dynamics (Sharifabadi et al., 2016). In addition, the dynamics of upper and lower arm can be explored. However, this strategy cannot represent the harmonic content of the converter since the modulation strategy and the switching events are not represented by this model.

3.1.4 Voltage Source Model (VSM)

The third reduced-order model is the VSM. Since MMC is a voltage source converter, its output characteristics can be represented as an ideal controlled voltage source in series with an equivalent output impedance. The schematic of this model is shown in Fig. 16, where $L_{eq} = \dfrac{L_{arm}}{2}$ and $R_{eq} = \dfrac{R_{arm}}{2}$, based on equation (2.7).

The voltage $v_{s,n}$ is computed by the grid current control strategy, shown in Fig. 17. It is highlighted that the circulating current control and S&S algorithm are not implemented, because the SMs and arms are not represented in this model.

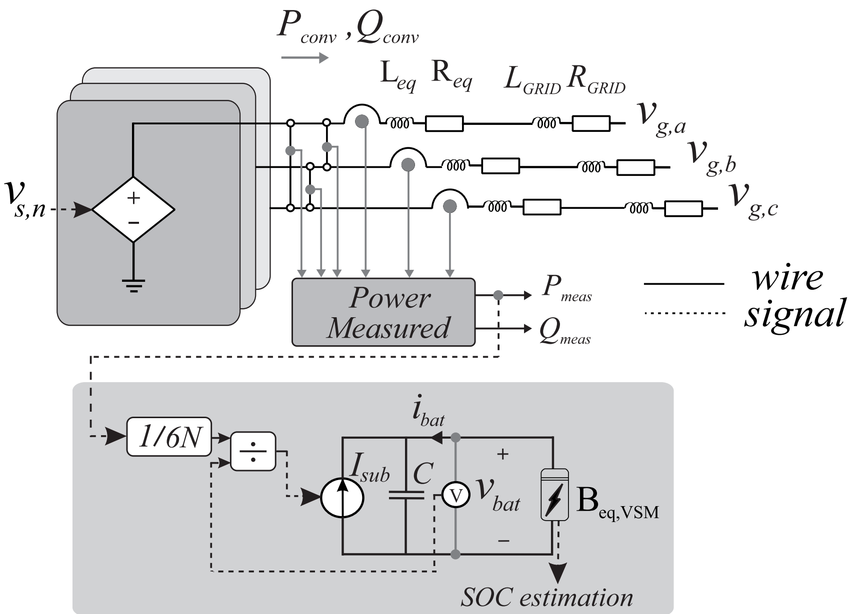

Figure 16 – Voltage Source Model (VSM).

VSM is implemented with a reduced number of components, which reduces the processing time. Although the internal dynamics of the converter are not directly represented, such as the individual SM dynamics and the arm dynamics. The overall SOC can be still roughly estimated through the output active power, as presented in Fig. 16.

In VSM, the computed SOC average is one per phase, because, in this model, the arms are not considered individually. The active and reactive power measured are derived from the converter output terminals, as shown in Fig. 16.

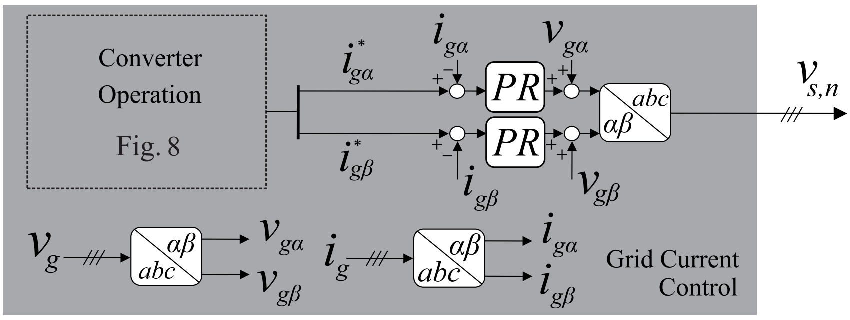

Figure 17 – ES-STATCOM control strategy for VSM model.

3.2 Battery Rack Model

The performance modeling of Li-ion batteries are strongly necessary in ES-STATCOM systems, once the derivation of SOC and battery voltage are the two main variable related with power capability. In this sense, several studies propose equivalent models to modeling the battery performance (Stroe, 2014; Vasiladiotis; Rufer, 2015; Li et al., 2018). Stroe (2014) divided the equivalent models to battery, in three categories:

- electrochemical Performance (ECP) Models: EP models are able to represent the estimate of the growth of solid electrolyte interface in Li-ion batteries and consider various aspects, as the mass transport in the electrolyte, which has a significant effect on the battery performance. The advantage of EP model is the precision to predict macroscopic and microscopic battery variables, as voltage, current, temperature, among others. However, the EP models are described by partial different equations, which are difficult to parametrize without expensive and specialized equipment, requiring huge computational efforts. Thus, in a large system simulation, as power system, this model is not applicable;

- mathematical Performance (MP) Models: MP models are developed based on empirical equations and are able to predict only macroscopic variables, such as voltage, efficiency, and SOC. The majority of these model considering the battery voltage as a function of internal resistance and open circuit voltage. Depending on the level of detail of the model, the main advantage is the reduced computational effort. However, the disadvantage of MP model is the limited accuracy;

- electrical Performance (EP) Models: EP models are using an equivalent electrical circuit to describe the performance behavior of batteries. Thus, the model using a combinations of voltage sources, capacitors, resistances and inductances, which are describing with relatively high accuracy (generally, in order of 1-5 %) the battery variables (e.g. voltage, current, SOC, among others.). In simulation that involves power system, as this work, the EP model is adopted, for the ease of integration with the CS simulation model (Vasiladiotis; Rufer, 2015; Li et al., 2018; Cao; Kroeze; Krein, 2016).

Based on previous discussion, the EP model is developed in this work. The battery rack model employed in the simulation models is presented in Fig. 18 (Álvarez Antón et al., 2013). The OCV versus SOC characteristic is included through a look-up table. This aggregated model computes the battery rack current and voltage. An interesting feature of this model is that the complexity is decoupled with the number of series battery racks N_s in each string and N_p string in parallel.

This model provides an estimation of the equivalent battery rack SOC. The battery rack model is employed based in the SOC estimation given by (Fotouhi et al., 2018):

$$SOC(t) = \left(\frac{\int_0^t i_{bat}(\tau) d\tau}{C_{bat,n}} + SOC_{bat,0} \right), \tag{3.4}$$

where $C_{bat,n}$ is the battery nominal capacity, $SOC_{bat,0}$ is the battery initial SOC in the analyzed cycle and i_{bat} is the instantaneous battery current.

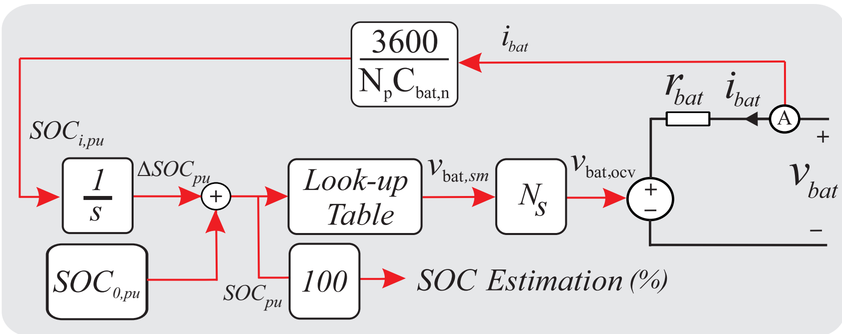

Figure 18 – Structure of a battery rack model. *Remark:* The number 3600 is the time, in seconds, of battery energy exchange in one hour (60×60=3600).

The battery rack model is employed with an equivalent electrical circuit, composed of a controlled voltage source, $v_{bat,ocv}$, and an equivalent series resistance, r_{bat}, that computes the internal losses (Cao; Kroeze; Krein, 2016; Tariq et al., 2018). Equation (3.4) computes the SOC estimation, and based on the look-up table shown in Fig. 10, it is derived the open-circuit battery voltage, that provides the voltage reference defined as $v_{bat,ocv}$. The gains $\frac{1}{N_p C_{bat,n}}$ and N_s realize the battery cell scale up to battery rack.

3.3 DSHB-MMC ES-STATCOM models for power systems service

Table 3 presents a typical time step required for some power systems and converter dynamics studies. For simulations that requires typical time step until 0.1 μs and that require SM dynamics, the SLS model is more indicated in relation ALA and VSM models. For this order of time step, converter dynamics studies, as arm balancing, capacitor balancing, internal fault and semiconductors device losses require a small time step, to simulate the dynamic evolved in the studied phenomenon. This fact can be explained by the individual representation of SMs and switching events of semiconductors devices in SLS model.

On the other hand, ALA and VSM models denote good characteristics in simulation that involves power systems integration studies with relative large time step, such as frequency support, voltage support, load flow, power oscillation damping, among others. Thus, step sizes in the range of 50 μs to 100 ms can be used. Generally, this time step is required in studies of external fault, transient, voltage and frequency stability. Besides, the VSM model presents poor characteristics in case of arm studies, as arm balancing and individual battery SOC, once the arm representation are neglected in this model.

Table 3 – Classification of three MMC model types applied in power systems (adapted from (Sharifabadi et al., 2016)).

Power systems and converter studies	Typical time step
External fault studies	50-100 μs
Transient stability	10-100 ms
Power oscillation damping	10-100 ms
Voltage support	10-100 ms
Frequency support	10-100 ms
Load flow	10-100 ms
Outer control	1-10 ms
Arm balancing	$100\mu s - 1ms$
Capacitor balancing	$100\mu s - 1ms$
Internal fault studies	$10 - 100\mu s$
Semiconductor device losses	$0.1 - 10\mu s$
Hardware design and protection	$0.1 - 10\mu s$

3.4 Performance Indexes

Several performance indexes have been proposed in the literature (Rekasius, 1961; Smith; Stringfellow, 1978; Egido; Fernandez-Bernal; Rouco, 2007), as the Integral of Squared Error (ISE) and the Integral of Absolute Error (IAE). These indexes are massively applied in control tuning, comparing the controlled variable and the reference. Furthermore, these indexes can be applied in a comparison between simulation models, setting a reference model and comparing with the experimental results.

The ISE and IAE computes the accumulated error between the reference variable and the measured variable in a squared and absolute form, respectively. In terms of analyze, it is difficult to construe a direct interpretation of the result, once it does not have a comparison with a reference area involved in the index calculation. In this sense, the NIAE index was introduced by (Pereira et al., 2014).

The models studied in this work are evaluated in terms of the NIAE index. This index performs a quantitative way of standardizing the model quality. For this, it computes a base case of MMC ES-STATCOM, that is given by the SLS model. This model is more accurate then the others, once the switching events are represented. Thus, the SLS model computes the variables of reference, expressed in a generic form, as $x_{ref}(t)$. The others models, as ALA and VSM, compute the measured variable, expressed as $x_m(t)$. The NIAE is defined by (Pereira et al., 2014), is given by:

$$NIAE = 1 - \frac{\int_{t_1}^{t_2} |x_{ref}(t) - x_m(t)|dt}{\int_{t_1}^{t_2} |x_{ref}(t)|dt}, \tag{3.5}$$

where the NIAE is evaluated in the time interval $[t_1, t_2]$. For this work, $x_{ref}(t)$ is the instantaneous variable obtained by SLS model and $x_m(t)$ is the instantaneous variable obtained through the reduced-order simulation model, ALA and VSM models.

The accuracy of the model is evaluated by the NIAE index result, taking a model as appropriate for its representation when NIAE ≥ 0.95. In case of NIAE < 0.95, the model may not represent well the reference model, being classified as an inadequate model (Pereira et al., 2014).

Finally, the processing time is measured using PLECS script considering the complete system (transformers, transmission lines, WPP model, grid model and ES-STATCOM model).

3.5 Chapter Conclusions

In this chapter, the models of a DSHB ES-STATCOM were analyzed. Furthermore, the NIAE index was chose to quantify the similarity between the ALA and VSM models in relation to the SLS model.

The battery rack model presents an electrical equivalent circuit, composed by a voltage source and a series resistance. In addition, these models compute a SOC estimation, based on the battery current, lookup table of OCV x SOC and the nominal battery capacity.

In terms of DSHB-MMC models, the SLS model computes the individual dynamics of each SM. On the other hand, the ALA and VSM are reduced structures of the DSHB ES-STATCOM, and compute a similar dynamics of each arm and each phase, respectively. These models neglect the switching events and individual dynamics of each SM.

4 Charging and Discharging Process

The results for the charging and discharging process considering a transmission system are presented in this chapter. In the Chapter 5, it is analyzed the performance of the DSHB ES-STATCOM models for the grid support studies in an offshore WPP application.

4.1 Case Study

The case study addressed in this work is based on a 100 MVA 33 kV DSHB ES-STATCOM that provides voltage and frequency support in a power system, presented in Fig. 19. The performance of SLS, ALA and VSM models during a batteries charging and discharging process is also analyzed. The models are validated by simulations through comparisons with a SLS model. The NIAE and the overall processing time are used as figures of merit.

The application of a DSHB ES-STATCOM in a transmission systems is illustrated in Fig. 19.

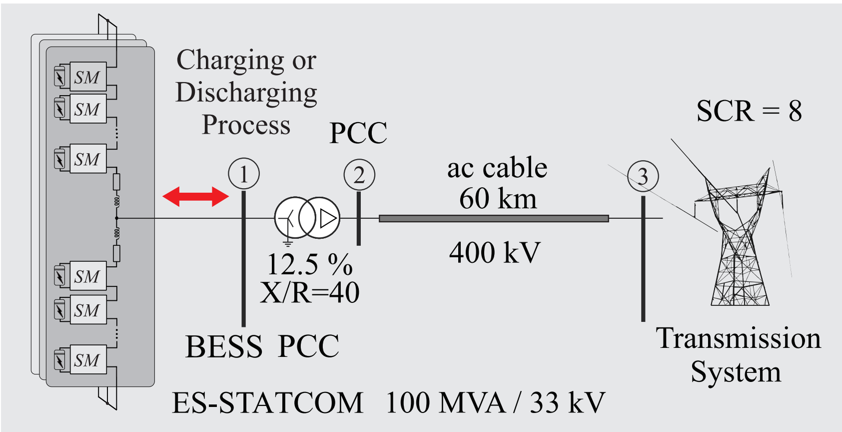

Figure 19 – ES-STATCOM application for a charging and discharging process.

The power system presented in Fig. 19 is composed of a: transmission system, ac cable and ES-STATCOM. In the bus 1, the DSHB ES-STATCOM of 100 MVA/33 kV is connected to a Y-Δ transformer. The transformer connects bus 1 to bus 2. Finally, the transmission system is coupled in the bus 3 by a 60 km ac cable, that connects the bus 2 to bus 3.

The DSHB ES-STATCOM simulation models are evaluated for the batteries charging and discharging process, starting with an initial SOC for all battery racks and setting the SOC reference in the global SOC control. The charging process is analyzed with a SOC reference of 52.5 %, initializing the batteries with 50.5 % of SOC in VSM and ALA model, while in the SLS model the SOC initial are distributed from 50 % to 51 %. In addition, the discharging process is analyzed with a SOC reference of 47.5 %.

The simulations for all case studies consider a multicore Personal Computer (PC) with an Intel Core i5-4430 3-GHz CPU and 8.0 GB RAM. The fixed step solver with a sample time of 74 μs was employed for all three models. The system presented in Fig. 19 was implemented in PLECS environment including the grid model, transmission lines, transformers and DSHB ES-STATCOM. The specifications of power systems components are listed below:

- grid Model: the model is composed of a controlled three-phase voltage source in series with an equivalent grid impedance. The grid frequency is computed considering a mechanical analog, which considers the effects of grid inertia and damping, as presented in Fig. 20. For this work, a 600 MVA/400 kV grid is employed, with parameters shown in Tab. 4;

- transmission Line: the three-phase transmission line is characterized by a uniform distribution of inductances, resistances and neutral capacitances along the line. There are also uniformly distributed mutual inductances and coupling capacitances. The simulation model consider distributed parameters based on traveling wave theory, which describes the time delay phenomenon. This approach is numerically more efficient due to the absence of numerous state variables and should be used in large models. The transmission line parameters are presented in Table 5, with line parameters based on (Kundur, 1994);

- Y-Δ Transformer: this component implements two-winding, three-phase transformers with a three-leg core. The transformer core is assumed symmetrical, where all phases have the same parameters. The windings are considered in star (Y) on the primary side. On the secondary side, the windings are either in delta (Δ) The 600 MVA Y-Δ transformer transforms 220 kV to 400 kV, with impedance of 12.5 % and X/R = 40.

Table 4 – Parameters of the Grid Model.

Parameters	Value
System frequency	50 Hz
Short-circuit ratio (SCR)	8
System damping	2 pu
System inertia	0.086 pu
Grid impedance X/R ratio	40

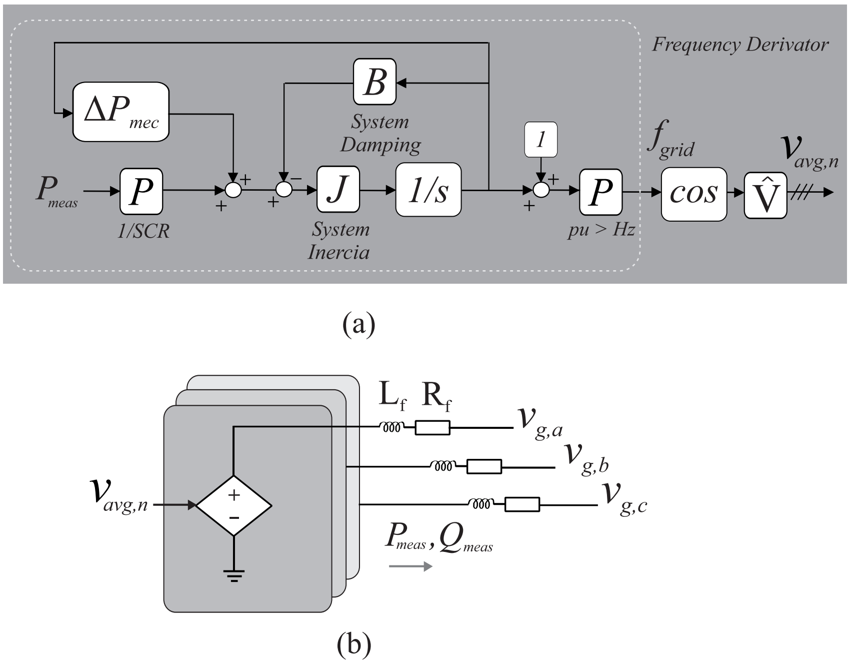

Figure 20 – Schematic diagram of the grid model (a) grid control strategy (b) grid voltage source model.

Table 5 – Parameters of the Transmission Line (π model).

Parameters	Value
Self inductance per unit length	862 nH/m
Mutual inductance per unit length	287.3 nH/m
Resistance per unit length	0.28 Ω/m
Neutral capacitance per unit length	13.8 nF/m
Coupling capacitance per unit length	4.6 nF/m
Length	60,000 m

4.2 DSHB-MMC based on ES-STATCOM Parameters

The parameters of the DSHB ES-STATCOM studied in this work are presented in Tab. 6.

A battery rack E3-R108 manufactured by Samsung is employed in this work (SAMSUNG, 2018). The main battery rack E3-R108 data are presented in Tab. 7. The SOC is assumed to vary from 10-90 % to design the DSHB ES-STATCOM. The lower limit in SOC operation is employed to reduce the depth of discharge (DOD) and increase the life span of the batteries (Dufo-López; Lujano-Rojas; Bernal-Agustín, 2014; Sangwongwanich et al., 2018). The upper limit is defined to reduce the calendar aging of the batteries (Stroe et al., 2016).

In addition, the controller parameters are shown in Tab. 8. The proportional integral controllers are discretized by Tustin method, while the proportional resonant controllers are discretized by Tustin with prewarping method (Cupertino et al., 2018).

Table 6 – Parameters of the DSHB ES-STATCOM.

Parameters	Symbol	Value
Rated apparent power [MVA]	S_n	100
Total energy storage [MWh]	E_n	150
Pole to pole dc voltage [kV]	V_{dc}	61
Output voltage (line-to-line) [kV]	V_g	33
Submodule rated voltage [kV]	V_{sm}^*	2.25
Grid frequency [Hz]	f_n	50
Arm inductance [mH]	L_{arm}	6.9
Arm resistance [mΩ]	R_{arm}	0.5
Submodule Capacitance for 40 kJ/MVA [mF]	C	8.8
Transformer inductance [pu]	L_{grid}	0.0125
Transformer X/R ratio	X/R	40
Number of submodules	N	30 per arm

Table 7 – Parameters of the Battery Rack E3-R108.

Parameters	Symbol	Value
Power capacity [Ah]	$C_{bat,n}$	111
Discharging rate	$C_{bat,r}$	0.5
Total energy storage [MWh]	$E_{bat,n}$	0.108
Battery rack voltage @ SOC = 100% [V]	-	1096
Battery rack voltage @ SOC = 90% [V]	$V_{bat,max}$	1069
battery rack voltage @ SOC = 10% [V]	$V_{bat,min}$	1045
battery rack voltage @ SOC = 0% [V]	-	845
Maximum allowed SOC [%]	SOC_{max}	90
Minimum allowed SOC [%]	SOC_{min}	10
Battery series resistance [mΩ]	R_s	0.1

Table 8 – Parameters of the Controllers.

Parameters	Symbol	Value
Sampling frequency	f_s	9.72 kHz
Proportional gain of SOC global control [MW]	$k_{p,SOC}$	0.440344
Integral gain of SOC global control [MW/s]	$k_{i,SOC}$	0.754572
Proportional gain of average control [Ω^{-1}]	$k_{p,avg}$	8.39
Integral gain of average control [Ω^{-1}/s]	$k_{i,avg}$	143.9
Proportional gain of grid current control [Ω]	$k_{p,g}$	6.3
Resonant gain of grid current control [Ω/s]	$k_{r,g}$	1000
Proportional gain of circulating current control [Ω]	$k_{p,z}$	1.3
Resonant gain of circulating current control [Ω/s]	$k_{r,z}$	1000
Circulating current LPF cut-off frequency	ω_c	8 Hz

4.3 DSHB-based ES-STATCOM Design

Based on the DSHB ES-STATCOM parameters the converter design is performed. The first step, considered the minimum required dc-link voltage. Thus, considering a modulation index of $m = 1.15$ (since the injection of 1/6 of third harmonic is considered in MMC control), a grid voltage variation of $\Delta v_g = 0.1$ pu and grid transformer impedance of $x_{eq} = 0.2$ pu, the minimum required dc-link voltage is:

$$v_{dc,min} = \frac{2\sqrt{2}}{1.15\sqrt{3}} \times 33,000 \times (1 + 0.1 + 0.2) \approx \; 61kV. \tag{4.1}$$

Based on (2.34), the required number of series battery racks is computed according to the SM reference voltage and maximum battery rack voltage as follows:

$$N_s = floor\left(\frac{2,250}{1,096}\right) = 2. \tag{4.2}$$

The required number of submodules per arm is computed by (2.35), considering the minimum dc-link voltage, the minimum battery rack voltage and the number of battery rack in series, as follows:

$$N = ceil\left(\frac{61,000}{2 \times 1,045}\right) = 30. \tag{4.3}$$

According to (2.37), the minimum battery power is computed by the minimum battery rack voltage, the discharging rate and the battery nominal capacity:

$$P_{b,min} = 1,045 \times 111 \times 0.5 \approx 58 \; kW. \tag{4.4}$$

As discussed, the number of parallel battery strings is computed from two criteria. Therefore, the number of parallel battery strings assuming the power criterion is given by (2.36):

$$N_{p,power} = ceil\left(\frac{100 \times 10^6}{6 \times 30 \times 2 \times 58 \times 10^3}\right) = 5. \tag{4.5}$$

On the other hand, using (2.38), the number of parallel strings assuming energy storage requirements criterion is given by:

$$N_{p,energy} = ceil\left(\frac{150 \times 10^6}{6 \times 108 \times 10^3 \times 30 \times 2 \times 0.8}\right) = 5. \tag{4.6}$$

Thus, the N_p assumed to design the converter is:

$$N_p = max(5; 5) = 5. \tag{4.7}$$

Therefore, $N_p = 5$ is employed. Finally, to design the passive components of DSHB, it is used equations (2.40) and (2.41), for deriving the SM capacitance and arm inductance, respectively. The SM capacitance is computed from the energy storage requirement, nominal converter power, number of submodules per arm and submodule reference voltage, that results in:

$$C = \frac{2 \times 40 \times 100 \times 10^6}{6,000 \times 30 \times (2,250)^2} \approx 8.8\ mF. \tag{4.8}$$

In addition, the arm inductance design, considering the arm impedance, grid voltage and grid frequency, is:

$$L_{arm} = 0.2 \times \frac{33,000^2}{10 \times 10^6 \times (2 \times \pi \times 50)} \approx 6.9\ mH. \tag{4.9}$$

4.4 Dynamic Response in Charging and Discharging Process

The batteries charging and discharging process is analyzed in terms of SOC, active power and grid current dynamics. The system simulated is presented in Fig. 19.

Fig. 21 presents the SOC signals for the upper arm in phase a. 30 signals are plotted for SLS (all SMs), 2 signals for ALA (upper and lower arm) and 1 signal for VSM. To charge the batteries, the active power flows from the grid to the batteries. In this work, negative active power means an energy absorption by the DSHB. On the other hand, positive active power means an energy inject by the DSHB, as present in the discharging process.

As observed, the estimated SOC for ALA and VSM are close to SLS SOC distribution. The value of SOC estimation for VSM model stands as average value of SOC estimation in SLS model, that is derived for upper and lower arm. In addition, the spread of SOC for SLS model is explained by the NLC algorithm that exchange the SMs inserted in the arm, based in the SOC value. For this work, a NLC ATB algorithm was implemented, considering a tolerance band of 1 % for the mean SOC in the upper and lower arm.

Fig. 22 presents the dynamic behavior of the instantaneous active power absorbed from the grid for both models. As observed, initially, the converter absorbs approximately 50 MW of active power from the grid. The value of active power is computed by the SOC global control. When the SOC reaches the reference, the transferred active power reduces to a value close to zero to maintain the SOC in the batteries.

Fig. 23 shows the grid current response for both models. As observed in Fig. 23(a), during the charging of batteries the current peak is 1.3 kA. When the batteries reaches the reference value of SOC (50.1%) the converter stop to exchange current. Additionally, Fig. 23(b) shows a detail in the grid current for both models, that is similar for all models.

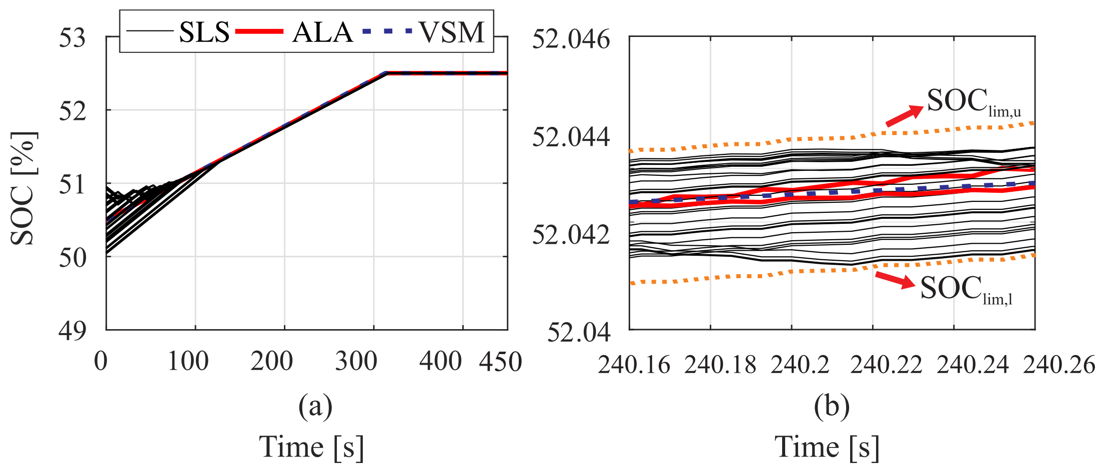

Figure 21 – Dynamic behavior of the SOC during the charging process for the three studied models. (a) SOC dynamic (b) detail in SOC charging.

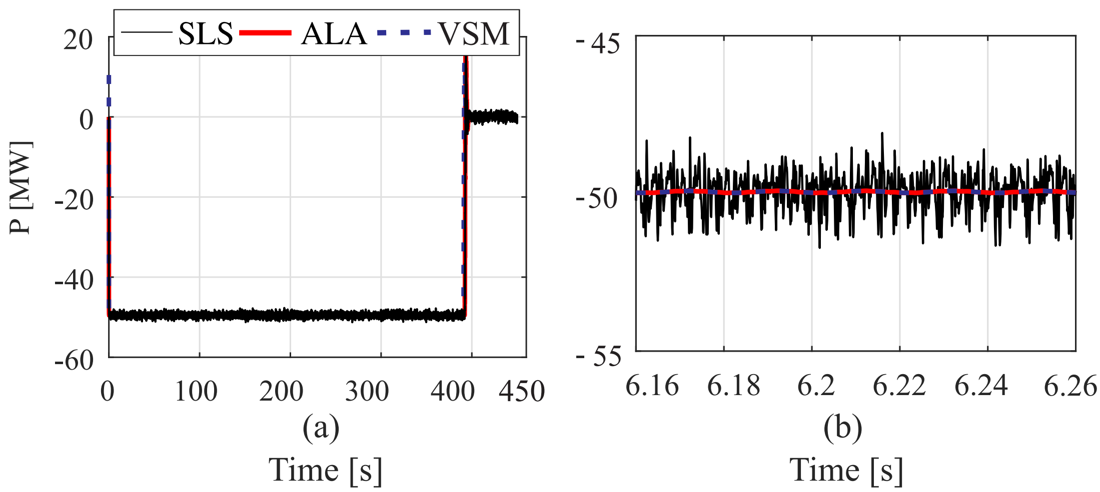

Figure 22 – Dynamic behavior of instantaneous active power during the charging process: Response of the SLS, VSM and ALA models. (a) active power dynamic (b) detail in active power.

The total harmonic distortion (THD) calculated for output current of SLS model reaches an average value of 1.31 % in the three phases. For the ALA and VSM model, the THD calculated reaches an average value of 0 %, once these models not present a switching events in SMs.

In addition, the batteries discharging process is analyzed in terms of SOC, active power and grid current dynamics. Fig. 24 presents the SOC signals for the upper arm in phase a. As observed, the estimated SOC for ALA and VSM are close to SLS SOC distribution, as in the charging process.

Fig. 25 presents the dynamic behavior of the instantaneous active power inject into the grid for both models. As observed, initially, the converter injects approximately 50 MW of active power during the discharging process.

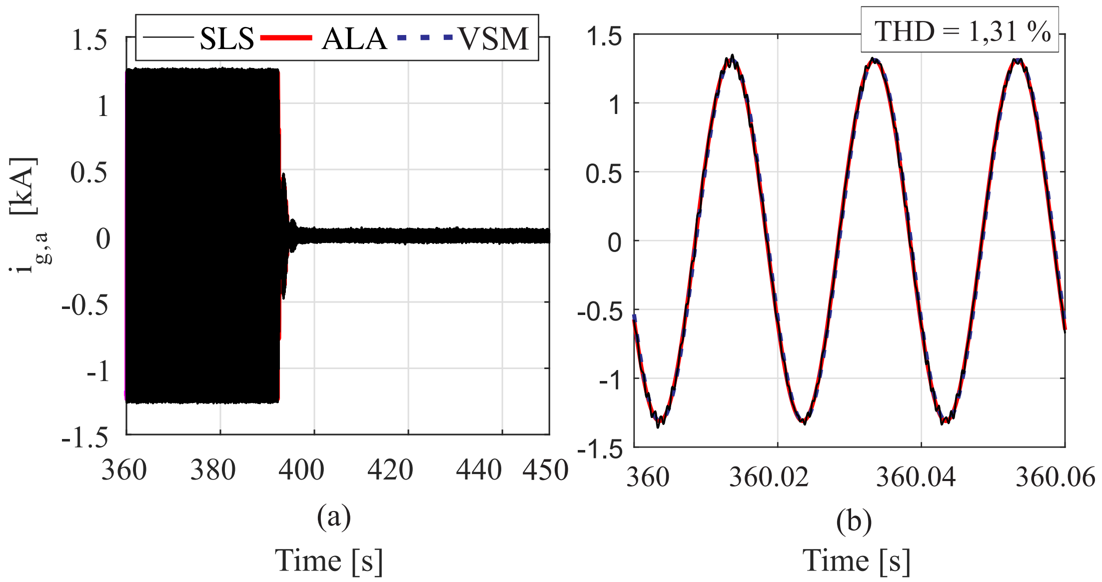

Figure 23 – Dynamic behavior of instantaneous DSHB output current during the charging process: Response of the SLS, VSM and ALA models. (a) DSHB output current dynamic (b) detail in DSHB output current.

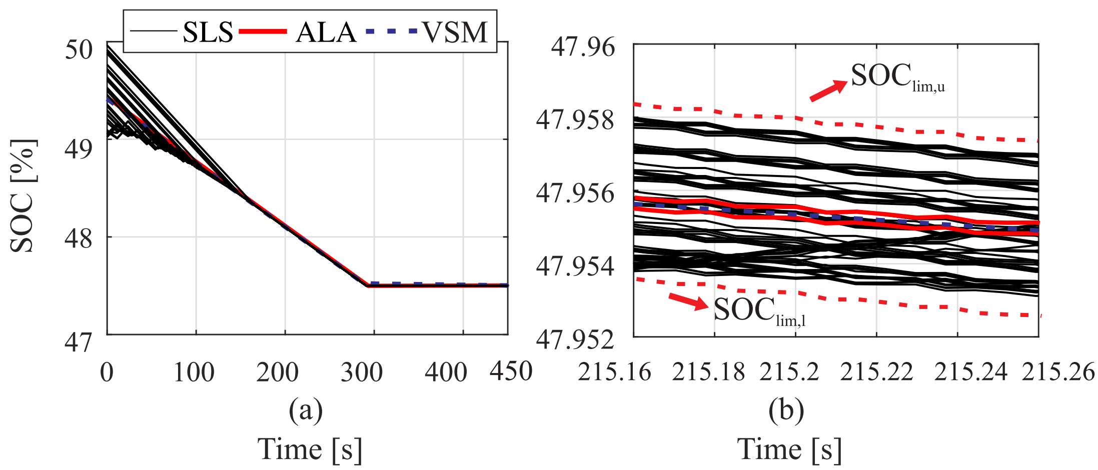

Figure 24 – Dynamic behavior of the SOC during the discharging process for the three studied models. (a) SOC dynamic (b) detail in SOC charging.

Fig. 26 presents the DSHB output current response for both models. As observed, in Fig. 26(a), during the batteries discharging the current peak is 1.3 kA. When the batteries reach the reference value of SOC (47.5 %) the converter stop to exchange energy. Additionally, Fig. 26(b) shows a detail in the DSHB output current for both models, that is similar for all models. The calculated total harmonic distortion output current of SLS model reaches an average value of 1.34 % between the three phases.

The performance in terms of error and time consumption of the three models are compared in Tab. 9. The NIAE is computed considering SLS as reference model, during the process of batteries charging ($t_1 = 0$ s and $t_2 = 450$ s). As observed, the models present a high NIAE (near the unit value), which means that the simplified models are suitable for

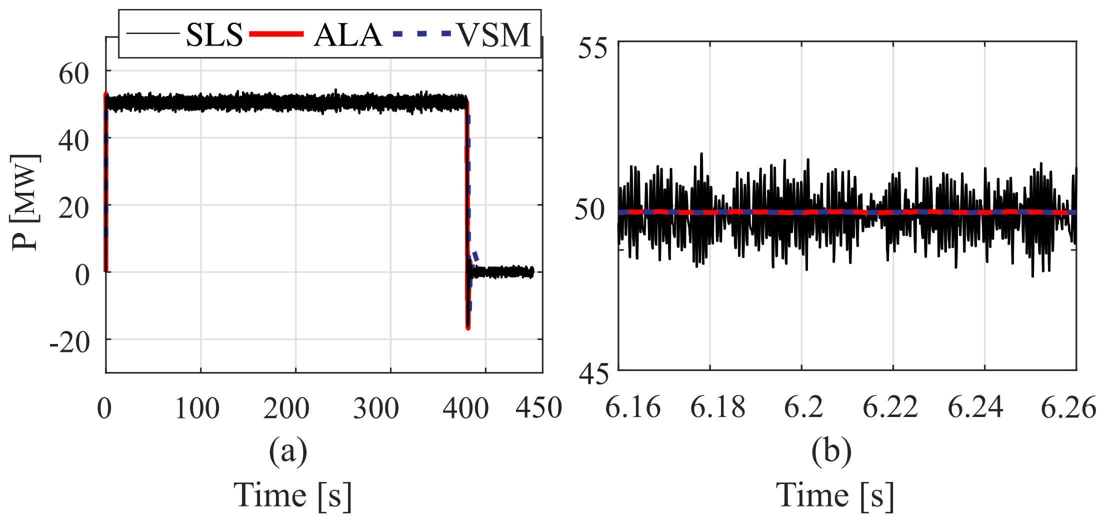

Figure 25 – Dynamic behavior of instantaneous active power during the discharging process: Response of the SLS, VSM and ALA models. (a) active power dynamic (b) detail in active power.

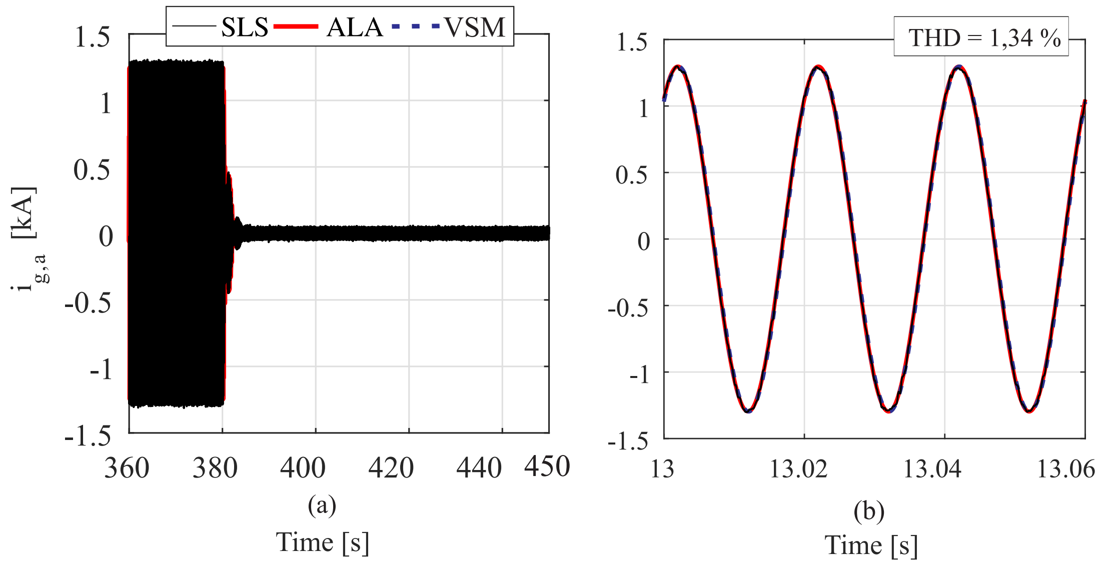

Figure 26 – Dynamic behavior of instantaneous DSHB output current during the discharging process: Response of the SLS, VSM and ALA models. (a) DSHB output current dynamic (b) detail in DSHB output current.

SOC control and discharging process studies. Regarding to the processing time, the ALA model results in a reduction of approximately 58 % in the processing time when compared to the SLS model. The VSM model results in a reduction of approximately 72 % in the processing time.

In addition, the Tab. 9 presents the results for the charging process. As observed, the models present a high NIAE (near the unit value), which means that the simplified models are suitable for SOC control and charging process studies. Regarding to the processing time, the ALA model results in a reduction of approximately 62 % in the processing time when compared to the SLS model. The VSM model results in a reduction of approximately 74 % in the processing time.

Table 9 – Performance comparison of the models during the battery discharging and charging process study.

Figure of merit	SLS	ALA	VSM
NIAE - P (Discharging)	-	0.993	0.992
Processing time (s) (Discharging)	1267.59	527.36	345.95
NIAE - P (Charging)	-	0.992	0.991
Processing time (s) (Charging)	1323.96	506.56	342.11

At this point, two important facts must be mentioned. Firstly, the simulation models proposed in this work can be employed for other control strategies and modulation algorithms. Secondly, unlike the SLS, the complexity of the VSM and ALA models are independent of N. Therefore, the gains observed in the processing time can be even higher if a MMC ES-STATCOM with more than 30 submodules is employed.

In relation to the power ratings of ES-STATCOM, the SOC increase or decrease 2 % during a time of 300s, in the discharging or charging process. The design considered a depth-of-discharge (DOD) of 80 %, which results in a 12,000 seconds (or 200 minutes) to discharge the batteries in the ES-STATCOM. Thus, considering an active power of 0.5 pu exchange by the converter, the calculated total energy of DSHB ($E_{bat,DSHB}$) results in:

$$E_{bat,DSHB} = \frac{80 \times 300}{2 \times 3600} \times 50 \times 10^6 = 166MWh, \tag{4.10}$$

On the other hand, based on the total energy storage value of battery rack E3-R108 employed, the nominal total energy of DSHB ($E_{n-bat,DSHB}$) results in:

$$E_{n-bat,DSHB} = 6 \times 2 \times 5 \times 30 \times 0.108 \times 10^6 \times 0.8 = 155.52MWh. \tag{4.11}$$

In this sense, as the considered total energy storage is $E_n = 150$ MWh, the calculated total energy storage based on simulation results extrapolates in 10 % the total energy storage of project. For the nominal total energy of DSHB, the extrapolation in 3.68 % is due to the approximation caused by the *floor* and *ceil* function in DSHB design.

4.5 Chapter Conclusions

In this chapter, the case study analyze the performance of simulation models were discussed. The case studies are employed on a power system composed of a DSHB ES-STATCOM and a transmission system. The analyzes consist of comparing the performance of models for the charging and discharging batteries process.

Based on the basic characteristics of the adopted DSHB ES-STATCOM, such as rated apparent power, total energy storage, output voltage and frequency, it was designed the numbers of series and parallel battery racks, number of submodules and passive components.

In relation to the case study I, that considered the batteries charging and discharging process, the results was presented in terms of SOC, active power and output current. The response for both models analyzed present a similar response, especially between VSM and ALA models. For the SLS model, the response presented an oscillation in the active power response, due to the switching events representation in this model. In addition, for the SOC analyses, it was obtained 30 signals for the SLS model in the upper arm, because this model computes the SOC for each SM. For the ALA model, it was presented two SOC signals, for the mean value of SOC in the upper and lower arm in phase a. Lastly, for VSM model it was presented one signal of the mean value of SOC in phase a.

The NIAE reveals for ALA and VSM model a high approximation degree with SLS model. In relation to the processing time, VSM model presents the lower value among the reduced-order models analyzed, with a reduction of more than 70 % in relation to the SLS model.

5 Frequency and Voltage Support

In this chapter, the DSHB based on ES-STATCOM simulation models are compared in two grid support cases, that provides frequency and voltage support. In all simulation models, the dynamic response of each model is compared in terms of SOC estimation, active and reactive power, grid current, negative/positive-sequence reactive-current (for voltage support study) and grid frequency response (for frequency support study). In addition, the models are compared in terms of the computational effort, based on the processing time and the difference among the dynamic behavior of the ALA and VSM models in relation to the SLS model, computing the NIAE.

5.1 Case Study

The power system for the grid support studies is presented in Fig. 27. The specifications of power systems components are listed below (the grid model, transmission line model and transformer model are the same described in section 4.1):

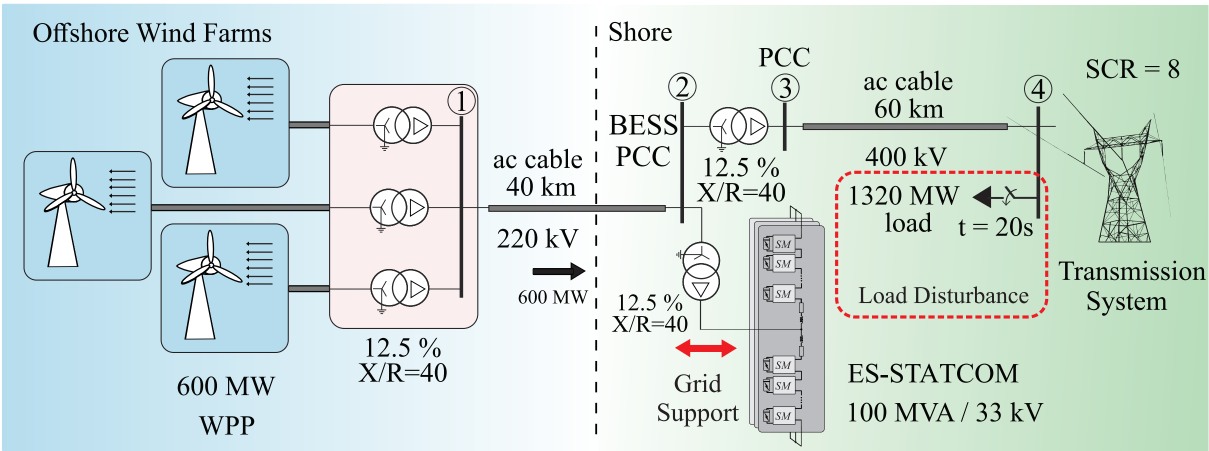

Figure 27 – ES-STATCOM application in an offshore WPP.

- offshore wind farms: The WPP is represented by an average model, where the three phase of converter are replaced by ideal voltage sources. In this structure, the calculated voltage is applied directly to voltage sources, without a PWM structure. This simplification allows to simulated the dc-link voltage dynamic, keeping the dc-link voltage control. The average model used reduces the simulation processing time, due to the elimination of semiconductor devices (Pereira et al., 2014). Fig. 28 present the schematic for the WPP reduced-order model, emphasizing the control strategy, in Fig. 28 (a) and the voltage source model, in Fig. 28 (b). In this work, a 600 MW WPP is employed;

- load disturbance: A three-phase load is used to produce a grid frequency disturbance. Thus, a balanced load of 1320 MW is inserted into the power systems, in bus 4, at the time of 20s.

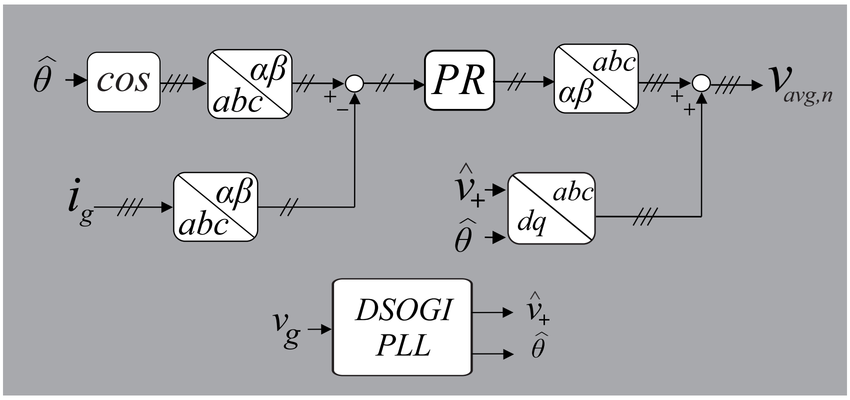

(a)

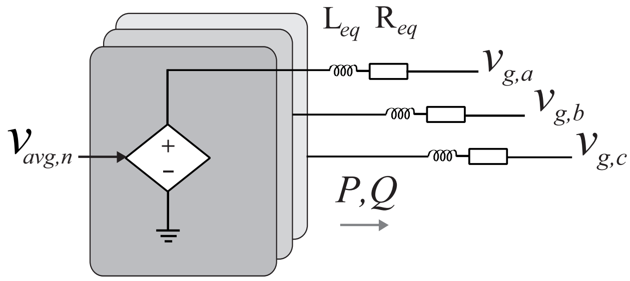

(b)

Figure 28 – Schematic diagram of the reduced-order model of WPP (a) WPP control strategy (b) WPP voltage source model.

To evaluate the dynamic behavior of the DSHB ES-STATCOM simulation models, two case studies are performed, as listed below:

- frequency support: The DSHB ES-STATCOM simulation models are evaluated for a frequency support case. In this case study, to cause a grid frequency disturbance, a load of 1320 MW is entered on bus 4, shown in the Fig. 27, at time t = 20s. At this time, the DSHB ES-STATCOM injects active power to provide frequency support;

- voltage support: The DSHB ES-STATCOM simulation models are evaluated for a voltage support case. The study is conducted considering a symmetrical fault in the bus 4, that is connected to the transmission system. A grid symmetrical fault of 50 % in the three phases of grid voltage is simulated. The fault starts at instant $t = 5$

s and finishes at the time $t = 5.2$ s. The voltage support droop curves follow the standard VDE-AR-N 4120:2015-01 (VDE, 2012).

5.2 Frequency Support Study

The grid frequency response is presented in Fig. 29. As observed, the grid frequency is constant and equal to 50 Hz before $t = 20$ s. At $t = 20$ s, the load is connected at bus 4 and a disturbance in the grid frequency is observed. If the ES-STATCOM is not employed, the grid frequency decreases, reaching values as low as 49.2 Hz. Under such conditions, the power system protection can lead to a blackout.

When the ES-STATCOM performs the primary frequency control, the converter starts to inject active power into the grid and the frequency remains in a safe region (grid frequency above 49.2 Hz). All simulation models exhibited comparable results and the frequency responses are very similar.

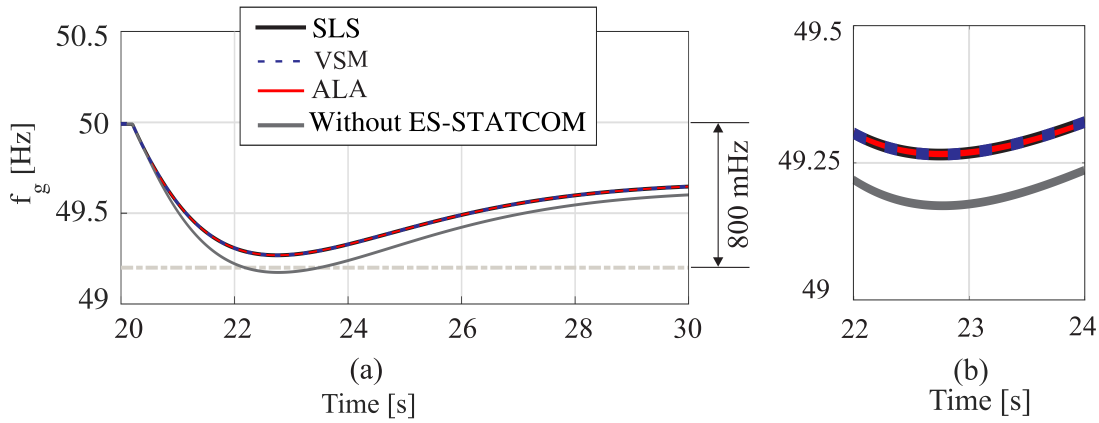

Figure 29 – Dynamic behavior of electrical grid frequency during the load disturbance: Response of the SLS, VSM and ALA models.

Fig. 30 presents the dynamic behavior of the instantaneous active power injected into the grid for all models. As observed, initially, the ES-STACOM is not exchanging active power with the grid. After the load transient, the converter starts injecting active power to perform primary frequency control. VSM and ALA models do not represent the converter switching and, for this reason, no ripples are observed in the instantaneous active power. The high frequency content in the injected power is not observed in the grid frequency, since the system inertia provides some filtering effect.

Fig. 31 shows the instantaneous reactive power injected into the grid. During the load transient, the converter starts to process active power and disturbances are observed in the reactive power. Nevertheless, ALA and VSM models do not present the higher harmonics components caused by the switching events as in the SLS model.

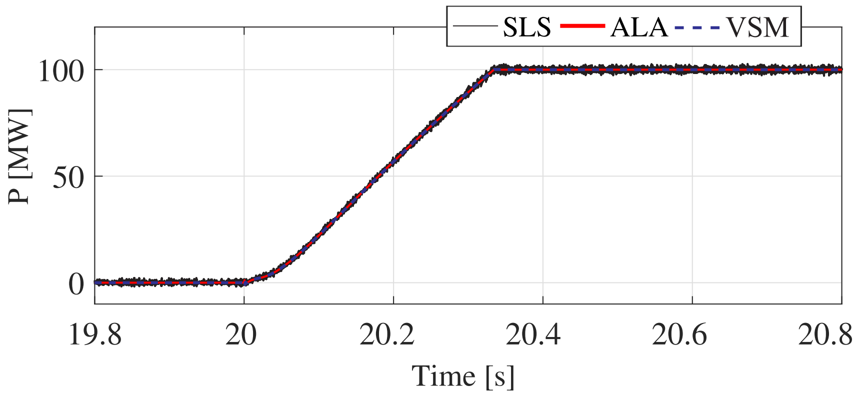

Figure 30 – Dynamic behavior of instantaneous active power during the load disturbance: Response of the SLS, VSM ALA models.

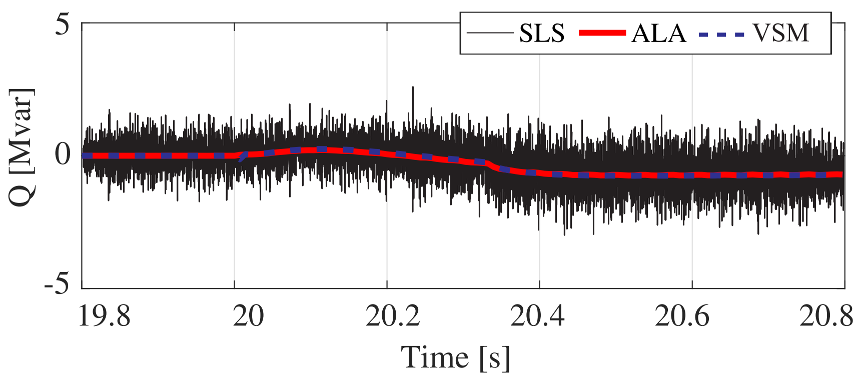

Figure 31 – Dynamic behavior of instantaneous reactive power during the load disturbance: Response of the SLS, VSM and ALA models.

Fig. 32 shows the instantaneous reactive power injected into the grid, considering the average value of reactive power in the SLS model. The average value is computed by a moving average filter, with an averaging time of $\frac{2}{f_n}$, to eliminate the ripple in reactive power response for SLS model. As observed, the variable of average reactive power is similar to the ALA and VSM model response. When the converter injects 1 pu of active power (approximately in t = 20.4 s), it is noticed that reactive power injection occurs (in order of 0.5 MVAr), due to the increase of the grid voltage, which leads the LVRT to insert a reactive component in the current of the reference grid current.

Fig. 33 presents the dynamic behavior of the grid current. Due to symmetry, only phase a is presented. The injected current follows the behavior of active power. At $t = 20.4$ seconds, the current reaches its nominal value, which corresponds to the injection of 100 MW into the electrical grid. The detailed views presented in Fig. 33 (b) and (c) indicate that ALA and VSM do not represent the harmonic content of the MMC ES-STATCOM.

The dynamic behavior of the circulating current is presented in Fig. 34. Since a distributed energy storage system is approached in this work, there is no dc-link current and the theoretical value of circulating current is zero. This value is considered in the ALA

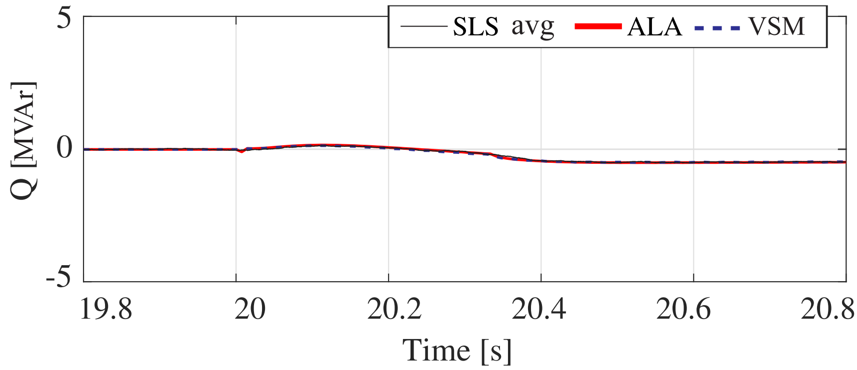

Figure 32 – Dynamic behavior of instantaneous reactive power during the load disturbance: Response of the SLS computed by a moving average filter, VSM and ALA models.

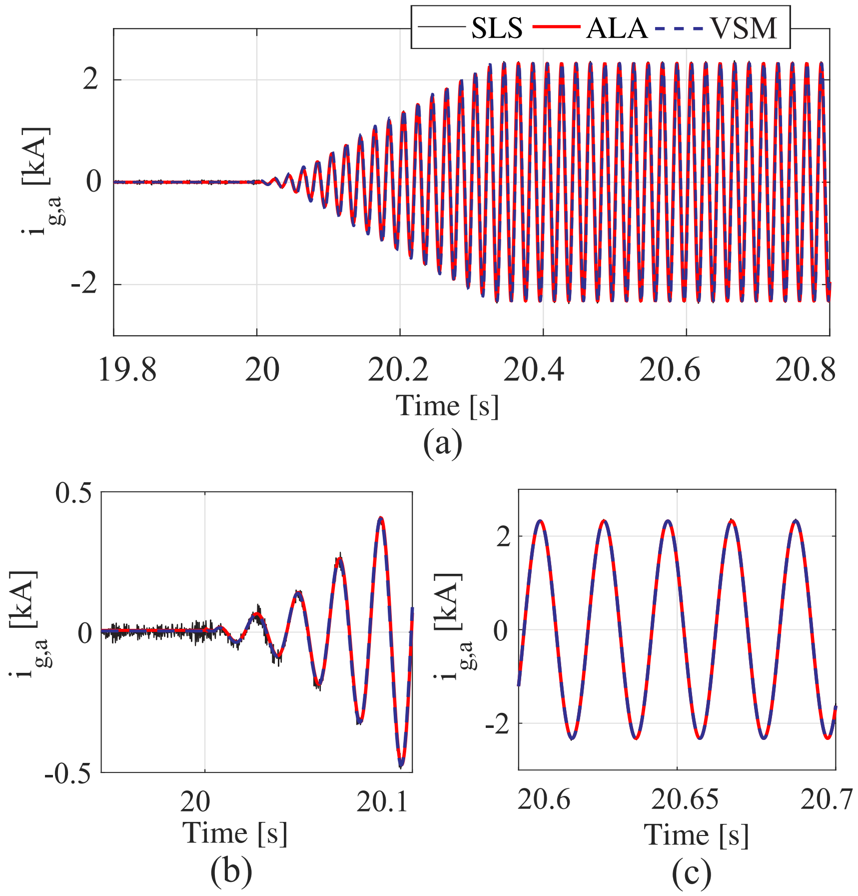

Figure 33 – Dynamic behavior of ES-STATCOM grid current during the load disturbance: Response of the SLS, VSM and ALA models (phase A): (a) Dynamic behavior of the grid current; (b) Detail in the current transient; (c) Detail in the current in steady-state.

and VSM models. Since the SLS model represents the converter switching, it can represent the ripple of circulating current.

Finally, the estimated SOC for the three simulation models are presented in Fig.

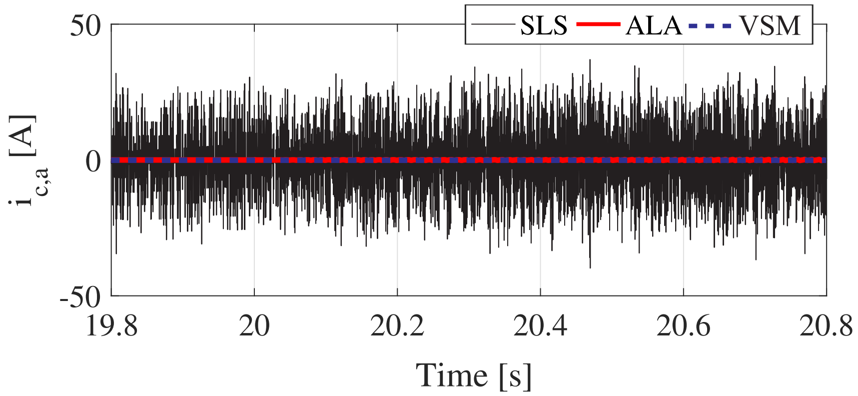

Figure 34 – Dynamic behavior of ES-STATCOM circulating current during the load disturbance: Response of the SLS, VSM and ALA models (phase a).

35, in which 30 signals are plotted for SLS, 2 for ALA and 1 for VSM. As observed, the ALA model can represent the SOC variation when compared with the SLS model. The variation observed in the SOC is related to the SOC balancing algorithm (S&S and NLC).

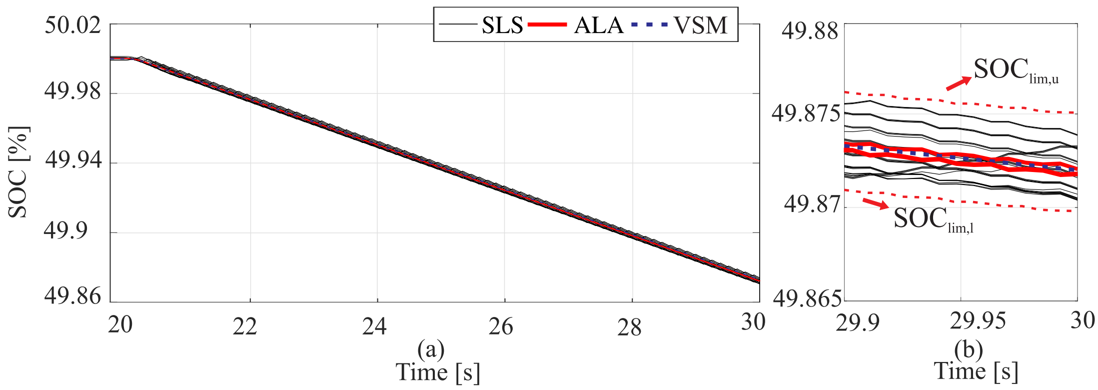

Figure 35 – Dynamic behavior of the SOC during the load disturbance for the three studied models.(a) SOC dynamic (b) detail in SOC discharging.

The performance of the three models are compared in Tab. 10. The NIAE is computed considering SLS as the reference model, during $t_1 = 19.8$ s to $t_2 = 30$ s. As observed, ALA and VSM models can reach a similar NIAE and present values higher than 0.99 for active power and grid frequency. Therefore, both models present a suitable performance for frequency support study.

Regarding the processing time, the ALA model results in a reduction of approximately 60 % in the processing time when compared to the SLS model. The VSM model results in a reduction of approximately 68 % times in the processing time.

Table 10 – Performance comparison of the models during the frequency support study.

Figure of merit	SLS	ALA	VSM
NIAE - P	-	0.993	0.993
NIAE - f_g	-	≈ 1	≈ 1
Processing time (s)	214.89	87.72	69.32

5.3 Voltage Support Study

Finally, the simulation models are analyzed in a symmetrical grid fault. The grid fault is applied to the transmission system model, that is connected to the bus 4. In this situation, the ES-STATCOM needs to inject reactive current, in bus 2, to support the voltage recovery (defined by VDE-AR-N 4120:2015-01 (VDE, 2012)), shown in Fig. 12. The grid fault is applied, based on 50% of voltage drop in the three phases of grid voltage, during the time interval of 5 s $\leq$ t $\leq$ 5.2 s.

The voltage support in a symmetrical fault is analyzed in terms of reactive current injection, grid voltage, grid current, active and reactive power. Fig. 36 (a) and Fig. 36 (b) show the detected positive-sequence of grid voltage ($v_{g,d}^{+}$) and negative-sequence grid voltage ($v_{g,d}^{-}$), respectively. As observed, the symmetrical fault just affect the positive-sequence voltage, resulting in a voltage drop of 0.5 pu in the positive-sequence of grid voltage.

Fig. 37 (a) shown the grid voltage drop, in bus 2, during the period between 5 s and 5.2 s. As observed, all phases are affected, reducing the peak of the grid voltage to 13.47 kV, approximately. In addition, Fig. 37 (b) shown the grid current injects by the ES-STATCOM. In this period, it injects the nominal output current of the DSHB-MMC ES-STATCOM. For all models, the response of grid current and voltage are similar.

Fig. 38 (a) and Fig. 38 (b), present the dynamic behavior of instantaneous active and reactive power, respectively. As observed, in the grid support, just reactive power is injected by the ES-STATCOM into the grid. The reactive power is about 0.5 pu of nominal reactive power, as the converter is operating with 0.5 pu of nominal grid voltage and 1 pu of grid current. The dynamic response of the SLS, VSM and ALA models are similar.

Fig. 36 (a) and Fig. 36 (b) presents the positive-sequence grid voltage (V_g^{+}) and negative-sequence grid voltage (V_g^{-}), respectively. The ES-STATCOM increases the support in 0.026 pu, once the case without ES-STATCOM reaches a positive-sequence grid voltage of 0.472 pu, while the case with ES-STATCOM reaches a positive-sequence grid voltage to 0.498 pu. Fig. 36 (c) and Fig. 36 (d) presents the injection of positive-sequence ($i_{g,q}^{+}$) and negative-sequence reactive-current ($i_{g,q}^{-}$), respectively, during the period of grid voltage drop. As observed, for a drop of 50%, the converter needs to inject 1 pu of positive-sequence reactive-current, as expected by LVRT (VDE, 2012).

The influence of WPP on grid support during the fault is assessed in the Fig. 39.

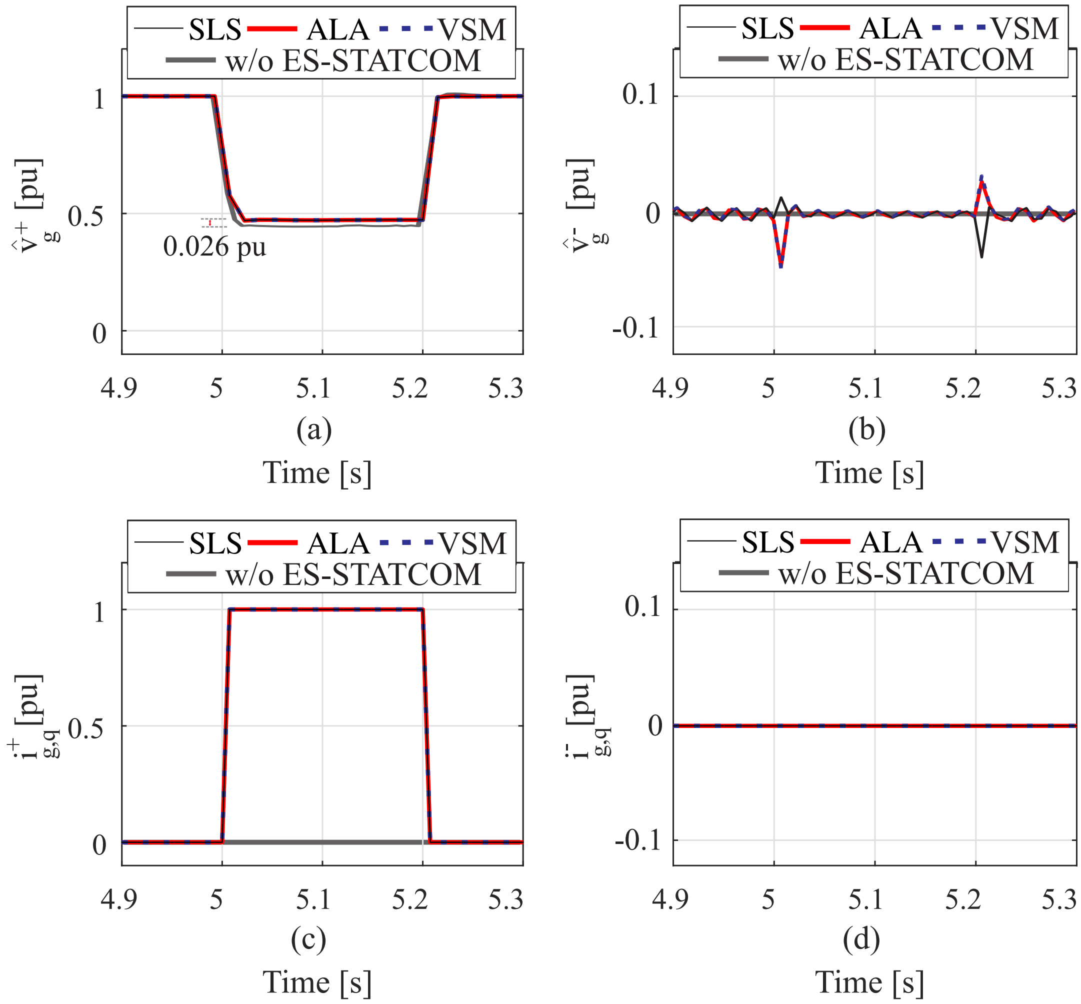

Figure 36 – Dynamic behavior of the negative/positive-sequence grid voltage and negative/positive-sequence reactive-current during the grid symmetrical fault for the SLS, VSM and ALA models. (a) positive-sequence grid voltage (b) negative-sequence grid voltage (c) positive-sequence reactive-current (d) negative-sequence reactive-current.

Without WPP and ES-STATCOM, the positive-sequence grid voltage decreases to 0.4 pu. For the case considered with ES-STATCOM, the grid voltage reduces to 0.498, which results in an addition of 0.098 pu provided by the WPP.

Finally, the performance of the SLS, VSM and ALA models are compared in Tab. 11. The NIAE is computed considering SLS as reference model, during the grid support (t_1 = 5 seconds and t_2 = 5.2 seconds). As observed, the models present a NIAE near 1, which means that the reduced-order models are suitable voltage support studies. Regarding to the processing time, the ALA model results in a reduction of 76 % in the processing time when compared to the SLS model. The VSM model results in a reduction of 81 % in the processing time.

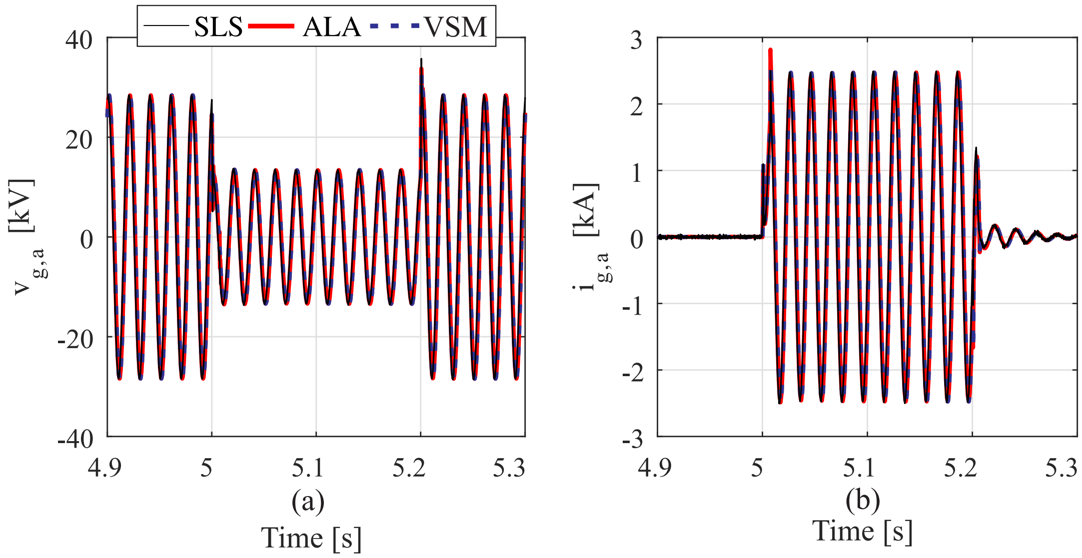

Figure 37 – Dynamic behavior of the grid voltage and grid current during the grid symmetrical fault for the SLS, VSM and ALA models. (a) instantaneous grid voltage (b) instantaneous grid current.

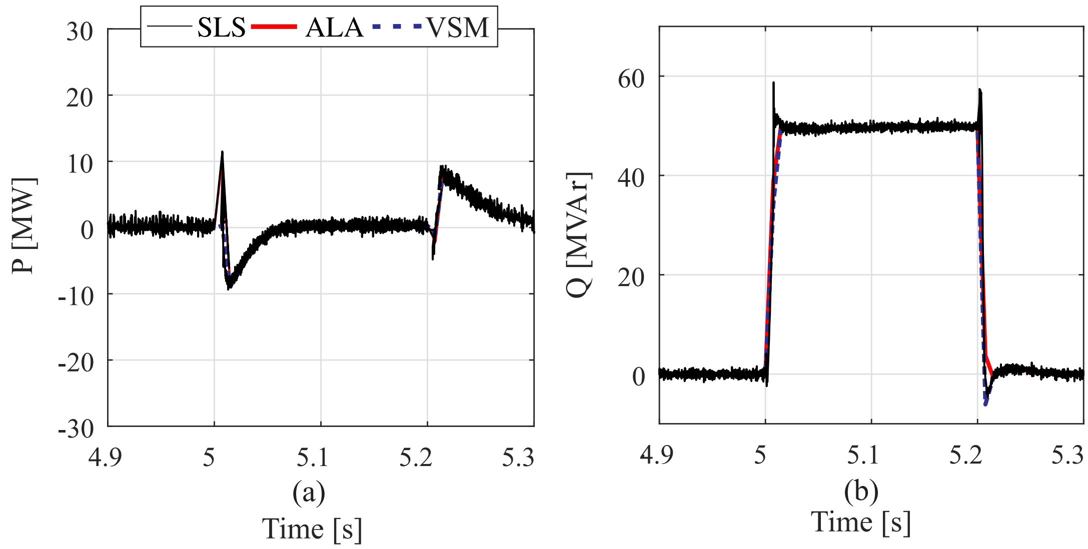

Figure 38 – Dynamic behavior of the instantaneous active and reactive power during the grid symmetrical fault for the SLS, VSM and ALA models. (a) instantaneous active power (b) instantaneous reactive power.

Table 11 – Performance comparison of the models during the grid voltage support study.

Figure of merit	SLS	ALA	VSM
NIAE - Q	-	0.993	0.99
Processing time (s)	167.44	40.28	31.89

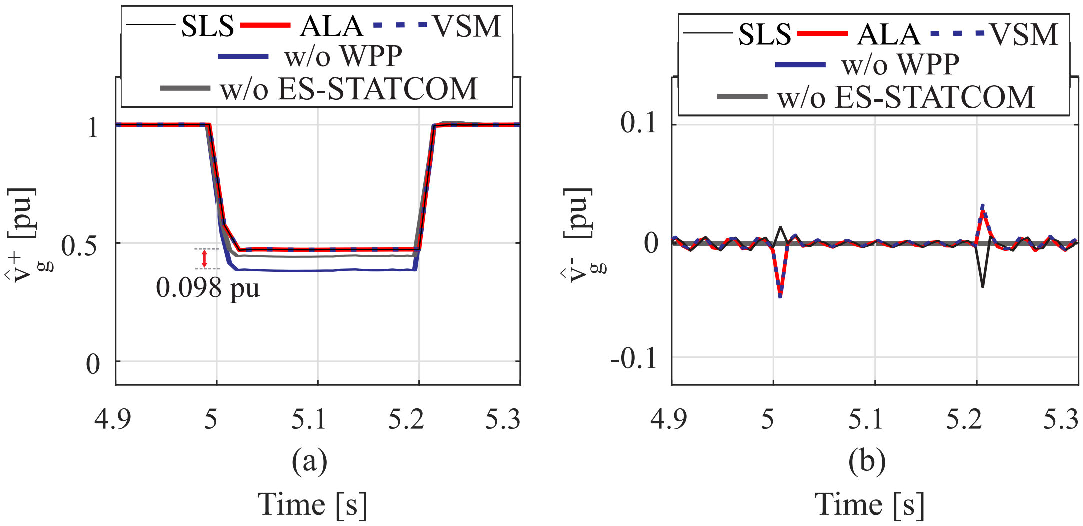

Figure 39 – Dynamic behavior of the negative/positive-sequence grid voltage and negative/positive-sequence reactive-current during the grid symmetrical fault for the SLS, VSM and ALA models. (a) positive-sequence grid voltage (b) negative-sequence grid voltage.

5.4 Chapter Conclusions

In this chapter, two case studies of grid support were implemented to analyze the performance of the simulation models. The analyses consists of comparing the performance of the models for frequency and voltage support.

During the frequency support, the dynamic behavior of the simulation models were similar. They were able to recover the grid frequency to attend the code requirement. In addition, it was verified the presence of oscillations in the SLS model for the variables of active power, reactive power and circulating current, explained by the representation of switching events in SLS model. The VSM and ALA models present a NIAE near 1, which reveals a high approximation of the variables in these models with the SLS model. In addition, the processing time with VSM model was the lowest value, with a reduction of 68 %.

Finally, the voltage support case study evaluates the performance of models, when they inject negative/positive-sequence reactive-current. The response is similar in terms of active power, reactive power, grid current and reactive-current for all models. The NIAE presented a value about to 1. In relation the processing time, the VSM model presents maximum reduction of 81 %.

6 Closure

6.1 Conclusions

This work presented three reduced-order models for DSHB-based ES-STATCOM. These models were discussed and compared through three different case studies: batteries charging and discharging process, grid support considering a grid symmetrical fault and frequency support. The DSHB design was presented to fulfill the power ratings of ES-STATCOM. In addition, three main objectives were defined. The conclusions of these objectives are presented separately.

Objective 1: Evaluate the MMC dynamics during BESS charging and discharging process

The results of Chapter 4 demonstrated that the charging and discharging process requires a long time to reach the reference SOC, depending on the SOC reference. For the case study, the discharging and charging process were analyzed with a variation of ± 2.5 % in the initial SOC value. The results reveal that SLS model requires a processing time in order of 58 % to 74 % higher than ALA and VSM reduced-order models, respectively.

ALA model resulted in a considerably reduced simulation time (2.5 times faster than SLS) and suitable results for frequency support studies. VSM is able to further reduce the processing time (3.6 times faster than the SLS). For this reason, for deeper discharging or charging in the BESS, the SLS model requires a higher computational effort and are not indicated, while the VSM and ALA are able to these simulations.

Furthermore, it has been verified that SLS model can represent the switching effects, expressed in the ripples in instantaneous power and circulating current. Nevertheless, the complexity of this model increases as the number of submodules. The SLS model also presented a suitable estimation of the SOC of the converter. The reduction in the simulation time with ALA and VSM is very significant, more than 58 %, and can be useful when a power system with a high number of buses must be simulated, which reveals VSM and ALA as a suitable models.

Objective 2: Design of the DSHB ES-STATCOM based on power capability

The Chapter 4 presented the design of DSHB for the ES-STATCOM system. The design was conducted by the converter characteristics, as the grid voltage, modulation index, rated apparent power and total energy storage.

The minimum dc-link voltage implemented was able to synthesize the grid voltage required. In addition, the number of battery rack in series produces the expected arm voltages. The number of battery rack string in parallel supported the grid current. The power ratings calculated based on SOC indicates a 10 % extrapolation in the total energy storage considered in the ES-STATCOM design.

Objective 3: Simulation models considering an ES-STATCOM application in an offshore WPP, during voltage and frequency support

The results of Chapter 5 demonstrated that the reduced-order models are applicable in grid support case studies. Besides, the performance of simulation models indicated a high similarity (NIAE $\approx$ 1) between the VSM and ALA models in relation to the SLS model. In addition, the processing time presents a reduction in order of 2.5 and 3 times to ALA and VSM model, in relation to the SLS model.

Finally, the exchange of energy for grid support was achieved in the voltage and frequency support case studies. The active power exchange was able to regulate the frequency above 49.2 Hz, just as the negative/positive-sequence reactive-current injection were able to recover the grid voltage during the applied symmetrical fault.

The conclusions obtained in this work can be summarized in Table 12, that presents a comparison between the reduced-order models studied. These models are evaluated in terms of simulation time for certain power systems services, based in typical time step, where "++" denotes good characteristics, "+" denotes acceptable characteristics and "-" denotes poor characteristics.

Table 12 – Benchmarking of SLS, ALA and VSM reduced-order models applied to power systems.

Power systems studies	SLS	ALA	VSM
Charging and Discharging Process	-	++	++
Voltage Support	+	++	++
Frequency Support	+	++	++
Transient Stability	+	++	++
Power Oscillation Damping	+	++	++
Outer Control	+	++	++
Arm Balancing	++	+	-
SOC Balancing	++	+	-

6.2 Future Works

Some future topics derived from this Master thesis are highlighted as follows:

- evaluation of reduced-order models in other DSHB applications, such as HVDC and active power filters;

- evaluation of the impact of different modulation strategies in DSHB ES-STATCOM considering the SLS model;
- application of the methodology proposed in other ancillary services, as peak shaving, time shifting, among others;
- comparison among others reduced-order or averaged simulation models;
- economical evaluation of a DSHB ES-STATCOM in terms of implementation cost and energy losses.

References

ABB. *DynaPeaQ Energy Storage System – A UK first.* 2016. Available in: <Available:https://new.abb.com/facts/references/reference-dynapeaq---a-uk-first>. 30

ABB. *EssPro - Battery energy storage*. 2017. Available in: <https://new.abb.com/docs/librariesprovider78/eventos/jjtts-2017/presentaciones-peru/(dario-cicio)-bess---battery-energy-storage-system.pdf?sfvrsn=2>. 15, 30, 31

Abdelrazek, S. A.; Kamalasadan, S. Integrated pv capacity firming and energy time shift battery energy storage management using energy-oriented optimization. *IEEE Transactions on Industry Applications*, v. 52, n. 3, p. 2607–2617, May 2016. 33

ADB. *Handbook on battery energy storage system*. 2018. Available in: <https://www.adb.org/sites/default/files/publication/479891/handbook-battery-energy-storage-system.pdf>. 11, 31, 32

AES. *SDGE, AES bring world's largest lithium ion battery storage online in California*. 2017. Available in: <https://www.utilitydive.com/news/sdge-aes-bring-worlds-largest-lithium-ion-battery-storage-online-in-cali/436832/>. 15, 31

Ahmed, N. et al. A computationally efficient continuous model for the modular multilevel converter. *IEEE J. of Emerging and Sel. Topics in Power Electron.*, v. 2, n. 4, p. 1139–1148, Dec 2014. 37

Ajaei, F. B.; Iravani, R. Enhanced equivalent model of the modular multilevel converter. *IEEE Transaction on Power Delivery*, v. 30, n. 2, p. 666–673, April 2015. 37

Akagi, H. Classification, terminology, and application of the modular multilevel cascade converter (mmcc). *IEEE Transaction Power Electronics*, v. 26, n. 11, p. 3119–3130, Nov 2011. 43

Arifujjaman, M. A comprehensive power loss, efficiency, reliability and cost calculation of a 1 mw/500 kwh battery based energy storage system for frequency regulation application. *Renewable Energy*, v. 74, p. 158 – 169, 2015. 36

Arslan, A. O. et al. Effect of arm inductance on efficiency of modular multilevel converter. In: *2018 2nd International Symposium on Multidisciplinary Studies and Innovative Technologies (ISMSIT)*. 2018. p. 1–4. 43

Baker, J. N.; Collinson, A. Electrical energy storage at the turn of the millennium. *Power Engineering Journal*, v. 13, n. 3, p. 107–112, June 1999. 30

Beddard, A.; Barnes, M.; Preece, R. Comparison of detailed modeling techniques for mmc employed on vsc-hvdc schemes. *IEEE Transaction on Power Delivery*, v. 30, n. 2, p. 579–589, April 2015. 37

Bharadwaj, C. A.; Maiti, S. Modular multilevel converter based hybrid energy storage system. In: *2017 IEEE PES Asia-Pacific Power and Energy Engineering Conference (APPEEC)*. 2017. p. 1–6. 29

BNEF. *A Behind the Scenes Take on Lithium-ion Battery Prices*. 2019. Available in: <https://about.bnef.com/blog/behind-scenes-take-lithium-ion-battery-prices/>. 11, 30, 31

Cao, Y.; Kroeze, R. C.; Krein, P. T. Multi-timescale parametric electrical battery model for use in dynamic electric vehicle simulations. *IEEE Transactions on Transportation Electrification*, v. 2, n. 4, p. 432–442, Dec 2016. 66

Ch, A. B.; Maiti, S. Modular multilevel e-statcom considering distributed energy storage at the dc link. In: *2016 IEEE 7th Power India International Conference (PIICON)*. 2016. p. 1–6. 36

Chatzinikolaou, E.; Rogers, D. J. A comparison of grid-connected battery energy storage system designs. *IEEE Transactions on Power Electronics*, v. 32, n. 9, p. 6913–6923, Sep. 2017. 30

CHEN, H. et al. Progress in electrical energy storage system: A critical review. *Progress in Natural Science*, v. 19, n. 3, p. 291 – 312, 2009. 30

Chen, Q.; Li, R.; Cai, X. Analysis and fault control of hybrid modular multilevel converter with integrated battery energy storage system. *IEEE Journal of Emerging and Selected Topics in Power Electronics*, v. 5, n. 1, p. 64–78, March 2017. 36

Cheng, Y. et al. A comparison of diode-clamped and cascaded multilevel converters for a statcom with energy storage. *IEEE Transaction Industrial Electronics*, v. 53, n. 5, p. 1512–1521, Oct 2006. 29

Chivukula, A. B.; Maiti, S. Analysis and control of modular multilevel converter-based e-statcom to integrate large wind farms with the grid. *IET Generation, Transmission Distribution*, v. 13, n. 20, p. 4604–4616, 2019. 36

CIGRE. *Guide for the Development of Models for HVDC Converters in a HVDC Grid*. 2014. 222 p. Available in: <https://e-cigre.org/publication/604-guide-for-the-development-of-models-for-hvdc-converters-in-a-hvdc-grid>. 29, 38, 55

Cupertino, A. F. et al. Dscc-mmc statcom main circuit parameters design considering positive and negative sequence compensation. *J. Control Autom. Electr. Syst.*, v. 62, n. 29, 2018. 54, 71

Cupertino, A. F. et al. Comparison of dscc and sdbc modular multilevel converters for statcom application during negative sequence compensation. *IEEE Transactions on Industrial Electronics*, v. 66, n. 3, p. 2302–2312, March 2019. 37

Dufo-López, R.; Lujano-Rojas, J. M.; Bernal-Agustín, J. L. Comparison of different lead–acid battery lifetime prediction models for use in simulation of stand-alone photovoltaic systems. *Applied Energy*, v. 115, p. 242 – 253, 2014. 71

Egido, I.; Fernandez-Bernal, F.; Rouco, L. Evaluation of automatic generation control (agc) regulators by performance indices using data from real operation. *IET Generation, Transmission Distribution*, v. 1, n. 2, p. 294–302, March 2007. 67

EIRGRID. *EirGrid Grid Code MPID275 GC8*. 2018. Http://www.eirgridgroup.com/site-files/library/EirGrid/Grid-Code.pdf. 55

Fang Zheng Peng. Z-source inverter. *IEEE Transactions on Industry Applications*, v. 39, n. 2, p. 504–510, March 2003. 34

Feng, S. et al. Mitigation of power system forced oscillations: An e-statcom approach. *IEEE Access*, v. 6, p. 31599–31608, 2018. 36

Fotouhi, A. et al. Accuracy versus simplicity in online battery model identification. *IEEE Transactions on Systems, Man, and Cybernetics: Systems*, v. 48, n. 2, p. 195–206, Feb 2018. 66

Garcia-Garcia, L.; Paaso, E. A.; Avendano-Mora, M. Assessment of battery energy storage for distribution capacity upgrade deferral. In: *2017 IEEE Power Energy Society Innovative Smart Grid Technologies Conference (ISGT)*. 2017. p. 1–5. 33

Ghat, M. B.; Shukla, A.; Mathew, E. C. A new hybrid modular multilevel converter with increased output voltage levels. In: *2017 IEEE Energy Conversion Congress and Exposition (ECCE)*. 2017. p. 1634–1641. 50

Gnanarathna, U. N.; Gole, A. M.; Jayasinghe, R. P. Efficient modeling of modular multilevel hvdc converters (mmc) on electromagnetic transient simulation programs. *IEEE Transactions on Power Delivery*, v. 26, n. 1, p. 316–324, Jan 2011. 59

Gu, Y.; Bottrell, N.; Green, T. C. Reduced-order models for representing converters in power system studies. *IEEE Transactions on Power Electronics*, v. 33, n. 4, p. 3644–3654, April 2018. 59

Hao, Q. et al. Reduced-order small-signal models of modular multilevel converter and mmc-based hvdc grid. *IEEE Transactions on Industrial Electronics*, v. 66, n. 3, p. 2257–2268, March 2019. 37, 59

Harnefors, L. et al. Dynamic analysis of modular multilevel converters. *IEEE Transaction on Industrial Electronics*, v. 60, n. 7, p. 2526–2537, July 2013. 43, 55

Hillers, A.; Biela, J. Fault-tolerant operation of the modular multilevel converter in an energy storage system based on split batteries. In: *2014 16th European Conference on Power Electronics and Applications*. 2014. p. 1–8. 37

Hillers, A.; Stojadinovic, M.; Biela, J. Systematic comparison of modular multilevel converter topologies for battery energy storage systems based on split batteries. In: *17th EPE'15 ECCE-Europe)*. 2015. p. 1–9. 37

Horiba, T. Lithium-ion battery systems. *Proceedings of the IEEE*, v. 102, n. 6, p. 939–950, June 2014. 30

IEA. *Energy storage - Tracking Clean Energy Progress*. 2019. Available in: <https://www.iea.org/tcep/energyintegration/energystorage/>. 11, 30, 31

IRENA. *Electricity storage and renewables: costs and markets to 2030*. 2017. Available in: <https://www.irena.org/-/media/Files/IRENA/Agency/Publication/2017/Oct/IRENA_Electricity_Storage_Costs_2017.pdf>. 30

Jianzhong Xu et al. Accelerated model of modular multilevel converters in pscad/emtdc. In: *2013 IEEE Power Energy Society General Meeting*. 2013. p. 1–1. 59

Karaagac, U. et al. Offshore wind farm modeling accuracy and efficiency in mmc-based multiterminal hvdc connection. *IEEE Transaction Power Delivery*, v. 32, n. 2, p. 617–627, April 2017. 37

Knap, V. et al. Sizing of an energy storage system for grid inertial response and primary frequency reserve. *IEEE Transactions on Power Systems*, v. 31, n. 5, p. 3447–3456, Sep. 2016. 29, 33

Krata, J.; Saha, T. K. Real-time coordinated voltage support with battery energy storage in a distribution grid equipped with medium-scale pv generation. *IEEE Transactions on Smart Grid*, v. 10, n. 3, p. 3486–3497, May 2019. 34

Krishnamoorthy, H. S. et al. Wind turbine generator–battery energy storage utility interface converter topology with medium-frequency transformer link. *IEEE Transactions on Power Electronics*, v. 29, n. 8, p. 4146–4155, Aug 2014. 34

Kundur, P. Power system stability and control. *McGraw-Hill*, USA, p. 209, 1994. 70

Lawder, M. T. et al. Battery energy storage system (bess) and battery management system (bms) for grid-scale applications. *Proceedings of the IEEE*, v. 102, n. 6, p. 1014–1030, June 2014. 30

Li, N. et al. Soh balancing control method for the mmc battery energy storage system. *IEEE Transaction Industrial Electronics*, v. 65, n. 8, p. 6581–6591, Aug 2018. 29, 47, 65, 66

Li, X.; Hui, D.; Lai, X. Battery energy storage station (bess)-based smoothing control of photovoltaic (pv) and wind power generation fluctuations. *IEEE Transactions on Sustainable Energy*, v. 4, n. 2, p. 464–473, April 2013. 33

Liu, Y. et al. Control system design of battery-assisted quasi-z-source inverter for grid-tie photovoltaic power generation. *IEEE Transactions on Sustainable Energy*, v. 4, n. 4, p. 994–1001, Oct 2013. 34

Lopez, A. M. et al. Limitations and accuracy of a continuous reduced-order model for modular multilevel converters. *IEEE Transactions on Power Electronics*, v. 33, n. 7, p. 6292–6303, July 2018. 59

Álvarez Antón, J. C. et al. Support vector machines used to estimate the battery state of charge. *IEEE Transactions on Power Electronics*, v. 28, n. 12, p. 5919–5926, Dec 2013. 66

Ma, Y. et al. Capacitor voltage balancing control of modular multilevel converters with energy storage system by using carrier phase-shifted modulation. In: *2017 IEEE Applied Power Electronics Conference and Exposition (APEC)*. 2017. p. 1821–1828. 44

Marquadt, R. Stromrichterschaltungen mit verteilten energiespeichern. *German Patent*, DE 20,011,030,31, 2001. 36

Meng, J. et al. An overview and comparison of online implementable soc estimation methods for lithium-ion battery. *IEEE Transactions on Industry Applications*, v. 54, n. 2, p. 1583–1591, March 2018. ISSN 1939-9367. 11, 53

NATIONAL GRID ELECTRICITY TRANSMISSION. *THE GRID CODE, ISSUE 5, REVISION 21*. 2017. 55

NEOEN. *Hornsdale Power Reserve*. 2018. Available in: <https://static.poder360.com.br/2018/12/Aurecon-Hornsdale-Power-Reserve-Impact-Study-2018.pdf>. 15, 31

NOBEL PRIZE. *The Nobel Prize in Chemistry 2019*. 2019. Available in: <https://www.nobelprize.org/uploads/2019/10/press-chemistry-2019-2.pdf>. 30

Pereira, H. A. et al. High performance reduced order models for wind turbines with full-scale converters applied on grid interconnection studies. *Energies*, v. 7, n. 11, p. 7694–7716, November 2014. 61, 68, 81

Pereira, H. A.; Kontos, E.; Teodorescu, R. High level performance models of double-star mmc converters. In: *2017 IEEE 8th International Symposium on Power Electronics for Distributed Generation Systems (PEDG)*. 2017. p. 1–6. 37

Pou, J. et al. Evaluation of the low-frequency neutral-point voltage oscillations in the three-level inverter. *IEEE Transactions on Industrial Electronics*, v. 52, n. 6, p. 1582–1588, Dec 2005. 36

Prasatsap, U.; Kiravittaya, S.; Polprasert, J. Determination of optimal energy storage system for peak shaving to reduce electricity cost in a university. *Energy Procedia*, v. 138, p. 967 – 972, 2017. 2017 International Conference on Alternative Energy in Developing Countries and Emerging Economies. 33

Qian, H. et al. A high-efficiency grid-tie battery energy storage system. *IEEE Transactions on Power Electronics*, v. 26, n. 3, p. 886–896, March 2011. 30

Rekasius, Z. A general performance index for analytical design of control systems. *IRE Transactions on Automatic Control*, v. 6, n. 2, p. 217–222, May 1961. 67

REN21. *RENEWABLES 2019 GLOBAL STATUS REPORT*. 2019. Available in: <https://www.ren21.net/wp-content/uploads/2019/05/gsr_2019_full_report_en.pdf>. 30

Rodrigues, S. et al. Steady-state loss model of half-bridge modular multilevel converters. *IEEE Transaction Industrial Application*, v. 52, n. 3, p. 2415–2425, May 2016. 38

Rodriguez, P. et al. Decoupled double synchronous reference frame pll for power converters control. *IEEE Transactions on Power Electronics*, v. 22, n. 2, p. 584–592, March 2007. 56

Rohner, S.; Weber, J.; Bernet, S. Continuous model of modular multilevel converter with experimental verification. In: *2011 IEEE Energy Conversion Congress and Exposition*. 2011. p. 4021–4028. 59

Saad, H.; Dennetière, S.; Mahseredjian, J. On modelling of mmc in emt-type program. In: *2016 IEEE 17th COMPEL*. 2016. p. 1–7. 61

Saad, H. et al. Modular multilevel converter models for electromagnetic transients. *IEEE Transaction Power Delivery*, v. 29, n. 3, p. 1481–1489, June 2014. 61

Saad, H. et al. Dynamic averaged and simplified models for mmc-based hvdc transmission systems. *IEEE Transaction Power Delivery*, v. 28, n. 3, p. 1723–1730, July 2013. 29, 37

SAMSUNG. *ESS Batteries by Samsung SDI*. 2018. Top Safety and Reliability Solutions. 15, 31, 71

Sangwongwanich, A. et al. Enhancing pv inverter reliability with battery system control strategy. *CPSS Transactions on Power Electronics and Applications*, v. 3, n. 2, p. 93–101, June 2018. 71

Saqib, M. A.; Saleem, A. Z. Power-quality issues and the need for reactive-power compensation in the grid integration of wind power. *Renewable and Sustainable Energy Reviews*, v. 43, p. 51 – 64, 2015. 29

Sato, Y.; Igarashi, H. Generation of equivalent circuit from finite-element model using model order reduction. *IEEE Transactions on Magnetics*, v. 52, n. 3, p. 1–4, March 2016. 59

Serban, I.; Marinescu, C. Control strategy of three-phase battery energy storage systems for frequency support in microgrids and with uninterrupted supply of local loads. *IEEE Transactions on Power Electronics*, v. 29, n. 9, p. 5010–5020, Sep. 2014. 33, 36

Sharifabadi, K. et al. Design, control and application of modular multilevel converters for hvdc transmission systems. John Wiley & Sons, 2016. 15, 37, 50, 51, 59, 61, 64, 67

SIEMENS. *Frequency and voltage support for dynamic grid stability*. 2018. Available in: <https://new.siemens.com/global/en/products/energy/high-voltage/facts/portfolio/svcplus-frequency-stabilizer.html>. 30

Smith, J. R.; Stringfellow, D. C. Numerical determination of a performance index for improved system response. *Proceedings of the Institution of Electrical Engineers*, v. 125, n. 7, p. 698–700, July 1978. 67

Sochor, P.; Akagi, H. Theoretical comparison in energy-balancing capability between star- and delta-configured modular multilevel cascade inverters for utility-scale photovoltaic systems. *IEEE Transactions on Power Electronics*, v. 31, n. 3, p. 1980–1992, March 2016. 36

Soong, T.; Lehn, P. W. Evaluation of emerging modular multilevel converters for bess applications. *IEEE Transactions on Power Delivery*, v. 29, n. 5, p. 2086–2094, Oct 2014. 36

Soong, T.; Lehn, P. W. Internal power flow of a modular multilevel converter with distributed energy resources. *IEEE Journal of Emerging and Selected Topics in Power Electronics*, v. 2, n. 4, p. 1127–1138, Dec 2014. 36

Soong, T.; Lehn, P. W. Assessment of fault tolerance in modular multilevel converters with integrated energy storage. *IEEE Transaction Power Electronics*, v. 31, n. 6, p. 4085–4095, June 2016. 37

Stroe, D. et al. A comprehensive study on the degradation of lithium-ion batteries during calendar ageing: The internal resistance increase. In: *2016 IEEE Energy Conversion Congress and Exposition (ECCE)*. 2016. p. 1–7. 71

Stroe, D.-I. Lifetime models for lithium ion batteries used in virtual power plants. AALBORG UNIVERSITY, 2014. 65

Tariq, M. et al. Modeling and integration of a lithium-ion battery energy storage system with the more electric aircraft 270 v dc power distribution architecture. *IEEE Access*, v. 6, p. 41785–41802, 2018. 66

Uno, M.; Tanaka, K. Influence of high-frequency charge–discharge cycling induced by cell voltage equalizers on the life performance of lithium-ion cells. *IEEE Transactions on Vehicular Technology*, v. 60, n. 4, p. 1505–1515, May 2011. 36

Vasiladiotis, M.; Cherix, N.; Rufer, A. Impact of grid asymmetries on the operation and capacitive energy storage design of modular multilevel converters. *IEEE Transactions on Industrial Electronics*, v. 62, n. 11, p. 6697–6707, Nov 2015. 36

Vasiladiotis, M.; Rufer, A. Analysis and control of modular multilevel converters with integrated battery energy storage. *IEEE Transaction Power Electronics*, v. 30, n. 1, p. 163–175, Jan 2015. 29, 37, 65, 66

Vazquez, S. et al. Energy storage systems for transport and grid applications. *IEEE Transactions on Industrial Electronics*, v. 57, n. 12, p. 3881–3895, Dec 2010. 34

VDE. *E VDE-AR-N 4120:2012-11 Technische Bedingungen für den Anschluss und Betrieb von Kundenanlagen an das Hochspannungsnetz*. 2012. 11, 55, 56, 83, 87

Velasco de la Fuente, D. et al. Photovoltaic power system with battery backup with grid-connection and islanded operation capabilities. *IEEE Transactions on Industrial Electronics*, v. 60, n. 4, p. 1571–1581, April 2013. 33

Walawalkar, R.; Apt, J.; Mancini, R. Economics of electric energy storage for energy arbitrage and regulation in new york. *Energy Policy*, v. 35, n. 4, p. 2558 – 2568, 2007. 33

Xavier, L. S.; Cupertino, A. F.; Pereira, H. A. Ancillary services provided by photovoltaic inverters: Single and three phase control strategies. *Computers Electrical Engineering*, v. 70, p. 102 – 121, 2018. 29, 34

Xu, J.; Gole, A. M.; Zhao, C. The use of averaged-value model of modular multilevel converter in dc grid. In: *2015 IEEE Power Energy Soc. General Meeting*. 2015. p. 1–1. 37

Xu, Z. et al. Study on black start strategy of microgrid with pv and multiple energy storage systems. In: *2015 18th International Conference on Electrical Machines and Systems (ICEMS)*. 2015. p. 402–408. 34

Zeng, R. et al. Design and operation of a hybrid modular multilevel converter. *IEEE Transaction on Power Electronics*, v. 30, n. 3, p. 1137–1146, March 2015. 50

Zhang, K.; Shan, Z.; Jatskevich, J. Large- and small-signal average-value modeling of dual-active-bridge dc–dc converter considering power losses. *IEEE Transactions on Power Electronics*, v. 32, n. 3, p. 1964–1974, March 2017. 59

Zhang, Y. et al. Simplified thermal modeling for igbt modules with periodic power loss profiles in modular multilevel converters. *IEEE Transaction Industrial Electronics*, v. 66, n. 3, p. 2323–2332, March 2019. 38

Zhao, C. et al. Energy storage requirements optimization of full-bridge mmc with third-order harmonic voltage injection. *IEEE Transactions on Power Electronics*, v. 34, n. 12, p. 11661–11678, Dec 2019. 49

Biography

William Caires Silva Amorim was born in Caetité - BA, Brazil in 1996. He received the B.S. degree in Electrical Engineering from the Universidade Federal de Viçosa (UFV), Viçosa - MG, Brazil in 2018. In this institution, he carried out research in the area of Information Theory, with emphasis on Coding Theory by the PICME Program (Programa de Iniciação Científica e Mestrado) and was a tutor of Signals and Systems. Currently, he is substitute professor at the Department of Electrical Engineering - UFV and a researcher assistant at Gerência de Especialistas em Eletrônica de Potência (GESEP), where he develops researches in the area of Power Electronics and Electrical Power Systems, with focus on Modular Multilevel Cascade Converters-based HVDC and ES-STATCOM systems.

E-mail: williamcaires490@gmail.com